

---

# Applied Research Laboratory

## Technical Report

### SUB-BAND MODULATION IN ACTIVE SONAR

PENNSTATE

---



The Pennsylvania State University  
The Graduate School  
Department of Acoustics

SUB-BAND MODULATION  
IN  
ACTIVE SONAR

A Thesis in  
Acoustics  
by  
Eric R. Boeker

© 2001 Eric R. Boeker

Submitted in Partial Fulfillment  
of the Requirements  
for the Degree of

Master of Science

December 2001

20011214 085

# REPORT DOCUMENTATION PAGE

Form Approved  
OMB No. 0704-0188

Public reporting burden for this collection of information is estimated to average 1 hour per response, including the time for reviewing instructions, searching existing data sources, gathering and maintaining the data needed, and completing and reviewing the collection of information. Send comments regarding this burden estimate or any other aspect of this collection of information, including suggestions for reducing this burden, to Washington Headquarters Services, Directorate for Information Operations and Reports, 1215 Jefferson Davis Highway, Suite 1204, Arlington, VA 22202-4302, and to the Office of Management and Budget, Paperwork Reduction Project (0704-0188), Washington, DC 20503.

1. AGENCY USE ONLY (Leave blank)		2. REPORT DATE December 2001	3. REPORT TYPE AND DATES COVERED Thesis in Acoustics; Master of Science	
4. TITLE AND SUBTITLE  SUB-BAND MODULATION IN ACTIVE SONAR			5. FUNDING NUMBERS	
6. AUTHOR(S)  Eric R. Boeker			8. PERFORMING ORGANIZATION REPORT NUMBER  TR 01-006	
7. PERFORMING ORGANIZATION NAME(S) AND ADDRESS(ES) Applied Research Laboratory The Pennsylvania State University P.O. Box 30 State College, PA 16804-0030				
9. SPONSORING / MONITORING AGENCY NAME(S) AND ADDRESS(ES) Office of Naval Research Ballston Tower One 800 North Quincy Street Arlington, VA 22217  Mr. Les Jacobi, Code 333			10. SPONSORING / MONITORING AGENCY REPORT NUMBER	
11. SUPPLEMENTARY NOTES				
12a. DISTRIBUTION / AVAILABILITY STATEMENT  Approved for public release; distribution is unlimited			12b. DISTRIBUTION CODE	
13. ABSTRACT (Maximum 200 words)  A method for the simultaneous transmission of multiple sonar signals is described and investigated. The sonar signals are linearly combined as the modulating phase component of a carrier signal, which avoids the transmit energy losses in peak power limited systems caused by a modulating amplitude. These modulating signals are designed to be spectrally separable upon reception, so each sonar signal can be simultaneously processed. Demodulation and echo processing techniques are then presented, and several experiments (both simulated and in-water) were conducted to investigate the detection performance of the modulated signals, as compared to the equivalent unmodulated signals. Results from these experiments indicate that the modulation technique is a viable method of transmitting multiple sonar signals simultaneously, while avoiding amplitude modulation.				
14. SUBJECT TERMS			15. NUMBER OF PAGES 85	
			16. PRICE CODE	
17. SECURITY CLASSIFICATION OF REPORT  Unclassified	18. SECURITY CLASSIFICATION OF THIS PAGE  Unclassified	19. SECURITY CLASSIFICATION OF ABSTRACT  Unclassified	20. LIMITATION OF ABSTRACT	

## GENERAL INSTRUCTIONS FOR COMPLETING SF 298

The Report Documentation Page (RDP) is used in announcing and cataloging reports. It is important that this information be consistent with the rest of the report, particularly the cover and title page. Instructions for filling in each block of the form follow. It is important to *stay within the lines* to meet optical scanning requirements.

**Block 1. Agency Use Only (Leave blank).**

**Block 2. Report Date.** Full publication date including day, month, and year, if available (e.g. 1 Jan 88). Must cite at least the year.

**Block 3. Type of Report and Dates Covered.** State whether report is interim, final, etc. If applicable, enter inclusive report dates (e.g. 10 Jun 87 - 30 Jun 88).

**Block 4. Title and Subtitle.** A title is taken from the part of the report that provides the most meaningful and complete information. When a report is prepared in more than one volume, repeat the primary title, add volume number, and include subtitle for the specific volume. On classified documents enter the title classification in parentheses.

**Block 5. Funding Numbers.** To include contract and grant numbers; may include program element number(s), project number(s), task number(s), and work unit number(s). Use the following labels:

C - Contract	PR - Project
G - Grant	TA - Task
PE - Program Element	WU - Work Unit Accession No.

**Block 6. Author(s).** Name(s) of person(s) responsible for writing the report, performing the research, or credited with the content of the report. If editor or compiler, this should follow the name(s).

**Block 7. Performing Organization Name(s) and Address(es).** Self-explanatory.

**Block 8. Performing Organization Report Number.** Enter the unique alphanumeric report number(s) assigned by the organization performing the report.

**Block 9. Sponsoring/Monitoring Agency Name(s) and Address(es).** Self-explanatory.

**Block 10. Sponsoring/Monitoring Agency Report Number.** (If known)

**Block 11. Supplementary Notes.** Enter information not included elsewhere such as: Prepared in cooperation with...; Trans. of...; To be published in.... When a report is revised, include a statement whether the new report supersedes or supplements the older report.

**Block 12a. Distribution/Availability Statement.** Denotes public availability or limitations. Cite any availability to the public. Enter additional limitations or special markings in all capitals (e.g. NOFORN, REL, ITAR).

DOD - See DoDD 5230.24, "Distribution Statements on Technical Documents."

DOE - See authorities.

NASA - See Handbook NHB 2200.2.

NTIS - Leave blank.

**Block 12b. Distribution Code.**

DOD - Leave blank.

DOE - Enter DOE distribution categories from the Standard Distribution for Unclassified Scientific and Technical Reports.

NASA - Leave blank.

NTIS - Leave blank.

**Block 13. Abstract.** Include a brief (*Maximum 200 words*) factual summary of the most significant information contained in the report.

**Block 14. Subject Terms.** Keywords or phrases identifying major subjects in the report.

**Block 15. Number of Pages.** Enter the total number of pages.

**Block 16. Price Code.** Enter appropriate price code (*NTIS only*).

**Blocks 17. - 19. Security Classifications.** Self-explanatory. Enter U.S. Security Classification in accordance with U.S. Security Regulations (i.e., UNCLASSIFIED). If form contains classified information, stamp classification on the top and bottom of the page.

**Block 20. Limitation of Abstract.** This block must be completed to assign a limitation to the abstract. Enter either UL (unlimited) or SAR (same as report). An entry in this block is necessary if the abstract is to be limited. If blank, the abstract is assumed to be unlimited.



## Abstract

A method for the simultaneous transmission of multiple sonar signals is described and investigated. The sonar signals are linearly combined as the modulating phase component of a carrier signal, which avoids the transmit energy losses in peak power limited systems caused by a modulating amplitude. These modulating signals are designed to be spectrally separable upon reception, so each sonar signal can be simultaneously processed. Demodulation and echo processing techniques are then presented, and several experiments (both simulated and in-water) were conducted to investigate the detection performance of the modulated signals, as compared to the equivalent unmodulated signals. Results from these experiments indicate that the modulation technique is a viable method of transmitting multiple sonar signals simultaneously, while avoiding amplitude modulation.

## Table of Contents

List of Figures . . . . .	vii
Glossary of Symbols . . . . .	ix
Acknowledgments . . . . .	xiv
Chapter 1. Introduction . . . . .	1
1.1 Motivation . . . . .	1
1.2 Literature Review . . . . .	2
1.3 Thesis Outline . . . . .	3
Chapter 2. Sonar Theory and Motivation . . . . .	5
2.1 Active Sonar Background . . . . .	5
2.2 Echo Processing . . . . .	9
2.3 General Waveform and Ambiguity Function Characteristics . . . . .	14
2.4 Motivation behind Sub-band Modulation . . . . .	22
Chapter 3. Modulation Theory . . . . .	25
3.1 Overview of Amplitude Modulation . . . . .	25
3.2 Overview of Angle Modulation and Sub-band Modulation . . . . .	30
3.2.1 Characteristics of Sub-band Modulation . . . . .	33
3.3 Demodulation . . . . .	38
3.3.1 Demodulation without Interference . . . . .	38
3.3.2 Demodulation in the Presence of Interference . . . . .	45
Chapter 4. Experiment . . . . .	50
4.1 Waveform Design Considerations . . . . .	50
4.2 Waveform Specifications . . . . .	52
4.3 Matlab Implementation . . . . .	58
4.4 Simulations . . . . .	59
4.5 In-Water Data . . . . .	61

Chapter 5. Results and Analysis . . . . .	63
5.1 Simulation Analysis . . . . .	63
5.2 In-Water Data Analysis . . . . .	76
Chapter 6. Summary and Conclusions . . . . .	79
References . . . . .	82

## List of Figures

2.1	Region of Signal Ambiguity of an Ambiguity Function and Cross-Section of Ambiguity Function Peak . . . . .	14
2.2	Example Sinewave Time Series and Frequency Spectrum . . . . .	15
2.3	Ambiguity Function of a Long Time Duration Sinewave . . . . .	16
2.4	Ambiguity Function of a Short Time Duration Sinewave . . . . .	16
2.5	Ambiguity Function Cross-Sections of a Long and Short Time Duration Sinewaves . . . . .	16
2.6	Example Linear Frequency Modulated Waveform Time Series and Frequency Spectrum . . . . .	17
2.7	Ambiguity Function of a LFM . . . . .	17
2.8	Ambiguity Function Cross-Section of a LFM . . . . .	17
2.9	Example Biphase Shift Keyed Waveform Waveform Time Series and Frequency Spectrum . . . . .	19
2.10	Ambiguity Function of a BPSK . . . . .	19
2.11	Ambiguity Function Cross-Section of a BPSK . . . . .	19
2.12	Matched Filter Responses of Different Signals in Reverberation . . . . .	21
3.1	Example Amplitude Modulation Suppressed Carrier of Two Sinewaves . . . . .	27
3.2	Example Amplitude Modulation with Carrier of Two Sinewaves . . . . .	29
3.3	Example Phase Modulation of Two Sinewaves . . . . .	31
3.4	Example Frequency Modulation of Two Sinewaves . . . . .	32
3.5	Sub-band Modulation of Two Sinewaves (Frequency Spectrum) . . . . .	34
3.6	Sub-band Modulation of Two Sinewaves with Increasing Deviation Constant . . . . .	37
3.7	Vector Addition of Echo Signal and Noise (High Signal-to-Interference Ratio at the Receiver) . . . . .	47
3.8	Vector Addition of Echo Signal and Noise (Low Signal-to-Interference Ratio at the Receiver) . . . . .	48
3.9	Maximum Amplitude Difference between the Received Signal (Signal plus Noise) and the Echo Signal with Respect to the Received Signal-to-Interference Ratio . . . . .	49

3.10	Maximum Phase Difference between the Received Signal (Signal plus Noise) and the Echo Signal with Respect to the Received Signal-to-Interference Ratio . . . . .	49
4.1	Spectral Constraints of Waveform Design . . . . .	53
4.2	Frequency Spectra of the Waveform Combinations Used in the Experiment . . . . .	55
4.3	Frequency Spectrum of the Sub-band Modulated BPSK and CW Waveform Combination before Transmission . . . . .	57
5.1	Comparison between Matched Filter Responses of Sub-band Modulated and Unmodulated BPSK and CW Signal Combination (stationary scatterer and matched carrier) . . . . .	64
5.2	Comparison between Matched Filter Responses of Sub-band Modulated and Unmodulated BPSK and CW Signal Combination (closing scatterer at 3 (m/sec.) and mismatched carrier) . . . . .	66
5.3	Comparison between Matched Filter Responses of Sub-band Modulated and Unmodulated BPSK and CW Signal Combination (opening scatterer at -3 (m/sec.) and mismatched carrier) . . . . .	67
5.4	Carrier Mismatch Results for BPSK and CW Signals . . . . .	69
5.5	Comparison between Matched Filter Responses of BPSK and CW Signal Combinations: Sub-band Modulated with Matched Carrier, Sub-band Modulated with Mismatched Carrier and Unmodulated (closing scatterer at 3(m/sec.) ) . . . . .	70
5.6	Comparison between Matched Filter Responses of Sub-band Modulated and Unmodulated LFM and CW Signal Combination (stationary scatterer and matched carrier) . . . . .	71
5.7	Matched Filter Responses of Sub-band Modulated BPSK and CW signal Combination, when Demodulation is Coupled with Hypothesis Testing . . . . .	73
5.8	Average of the Peak Matched Filter Responses with Respect to Received Signal-to-Interference Ratio . . . . .	75
5.9	Matched Filter Responses of Sub-band Modulated BPSK and CW Signal Combination (In-Water) . . . . .	78

## Glossary of Symbols

- $\beta$  • velocity induced time dilation factor
- $\hat{\beta}$  • bank of dilation factor hypotheses
- $\gamma$  • detection threshold of a matched filter
- $\Delta\tau_r$  • delay resolution
- $\Delta\phi_r$  • Doppler resolution
- $\Delta\omega$  • Difference between received carrier frequency and the carrier frequency used in the demodulator
- $\Delta r$  • range resolution
- $\Delta v_l$  • line-of-sight velocity resolution
- $\eta, \eta_m$  • center frequency of waveform(s) in Hz, where  $\omega_m = 2\pi\eta_m$
- $\theta$  • uniform phase of the scatterer  $S_s$
- $\kappa$  • number of sub-bands on either side of the carrier in sub-band modulation
- $\tau$  • time delay
- $\hat{\tau}$  • bank of time delay hypotheses
- $\phi$  • Doppler frequency
- $\phi_{dm}$  • Doppler frequency of demodulated sonar signal  $m$
- $\phi_{um}$  • Doppler frequency of signal  $m$  transmitted without sub-band modulation
- $\hat{\phi}$  • bank of Doppler hypotheses
- $\Phi_{ff}(\tilde{\beta}, \tilde{\tau})$  • wideband ambiguity function
- $\Phi_{ff}(\hat{\phi}, \hat{\tau})$  • narrowband ambiguity function
- $\psi(t), \psi_m(t)$  • phase modulation of a waveform(s)

- $\psi_a(t)$  • sub-band modulation combination of BPSK and CW waveforms, and identifier for the simulation set containing these waveforms
- $\psi_b(t)$  • sub-band modulation combination of LFM and CW waveforms, and identifier for the simulation set containing these waveforms
- $\psi_c(t)$  • sub-band modulation combination of four CW waveforms, and identifier for simulation set containing these waveforms
- $\psi_d(t)$  • sub-band modulation combination of four CW waveforms (two of duration  $T$  and two of duration  $\frac{T}{2}$ ), and identifier for simulation set containing these waveforms
- $\psi_n(t)$  • uniformly distributed phase of noise
- $\psi_R(t)$  • phase of received signal
- $\omega, \omega_m$  • center frequency of sonar waveform(s) ( $\omega = 2\pi$  [frequency in Hz])
- $\omega_0$  • carrier frequency (radians/sec.)
- $\omega_{max}$  • highest frequency of sub-band modulating signals (radians/sec.)
- $\omega_s$  • sampling frequency (radians/sec.)
- $\omega_{v_{lmax}}$  • maximum shifted frequency due to line-of-sight velocity (radians/sec.)
- $a(t), a_m(t)$  • amplitude modulation of waveform(s)
- $a_n(t)$  • Rayleigh distributed noise envelope
- $A_c$  • normalization factor of amplitude modulating signal
- $B$  • bandwidth of sub-band modulation
- $B_d$  • bandwidth of demodulation filter's stopband
- $B_{filter\ m}$  • passband of separation filter for signal  $m$
- $B_r$  • dilation bandwidth of Reverberation
- $B_t$  • bandwidth of transducer
- $c$  • speed of sound
- $e_o$  • transmitted signal energy

- $E\{\cdot\}$  • expected value
- $E_{eff}$  • energy efficiency
- $E_{max}$  • maximum transmit energy
- $E_s$  • expected value of received signal energy
- $E_t$  • transmit energy
- $f(\mathbf{p}, t), f(\beta(t - \tau))$  • wideband Doppler model of sonar waveform
- $f(t), f_m(t)$  • sonar waveform(s)
- $f_{max}$  • peak amplitude of transmit waveform
- $f_{uh\ m}(t)$  • unmodulated sonar waveform  $m$  frequency translated to the carrier frequency of sub-band modulating waveform(s) for comparison and evaluation purposes
- $\tilde{f}(t), \tilde{f}_m(t)$  • complex envelope of waveform(s)
- $H_0$  • hypothesis that only noise is present in the input data
- $H_1$  • hypothesis that the sonar signal is present in the input data
- $j$  • imaginary number ( $\sqrt{-1}$ )
- $J_m(k_p)$  • Bessel function of order  $m$  and argument  $k_p$
- $k_p$  • deviation constant or modulation index of phase modulation and sub-band modulation
- $k_f$  • deviation constant or modulation index of frequency modulation
- $K_d$  • discriminator constant
- $|\ell_{nb}|^2$  • narrowband matched filter
- $|\ell_{wb}|^2$  • wideband matched filter
- $n(t)$  • white Gaussian noise
- $N$  • number of sonar waveforms



- $N_o$  • power spectral density of noise
- $\mathbf{p}$  • vector of dilation and delay
- $\hat{\mathbf{p}}$  • vector of dilation and delay replicas
- $P(\cdot)$  • probability
- $P_d$  • probability of detection
- $P_f$  • probability of false alarm
- $P_{peak}$  • peak transmitted power
- $P(t)$  • instantaneous transmitted power
- $r_b$  • blind range
- $r(t)$  • received signal
- $R$  • distance to scatterer
- $R(t)$  • amplitude of received signal
- $s(t)$  • echo signal
- $s_1(t)$  • analytic echo signal
- $s_2(t)$  • basebanded  $s_1(t)$
- $s_3(t)$  • imaginary part of the natural logarithm of  $s_2(t)$
- $s_{3f}(t)$  • high-pass filtered version of  $s_3(t)$
- $s_d(t)$  • demodulated sonar signals
- $s_{dm}(t)$  • demodulated and separated sonar signal  $m$
- $s_{dhm}(t)$  • frequency translated version of  $s_{dm}(t)$
- $s_H(t)$  • Hilbert transform of echo signal
- $s_t(t)$  • transmitted signal
- $s_{um}(t)$  • sonar signal  $m$  transmitted without sub-band modulation as  $f_m(t)$  for comparison and evaluation purposes

$s_{uh\ m}(t)$  • sonar signal  $m$  transmitted without sub-band modulation as  $f_{uh\ m}(t)$  for comparison and evaluation purposes

$SIR_i$  • signal-to-interference ratio at the receiver

$SIR_o$  • signal-to-interference ratio at the matched filter output

$S_s$  • attenuation due to a slowly fluctuating point scatterer

$|S_s|$  • random Rayleigh magnitude of  $S_s$

$S_s(\beta, \tau)$  • echo spreading function for slowly fluctuating point scatterer

$S_s(\beta', \tau')$  • echo spreading function

$t$  • time

$T$  • time duration of waveform

$T_{lp}$  • time duration of long pulse sinewave

$v_l$  • line-of-sight velocity of scatterer

$v_p$  • sonar platform velocity

$v_s$  • scatterer velocity

$W, W_m$  • bandwidth of waveform(s)

$W_{sp}$  • bandwidth of short pulse sinewave

## Acknowledgements

I would like to thank the members of my committee Dr. Lora Weiss and Dr. Russell Burkhardt for their support and suggestions during this research and the writing of my dissertation. In particular, I would like to thank Dr. D.W. Ricker for his role as my thesis advisor.

I would also like to Dr. L.H. Sibul, Dr. J.J. Kisenwether, Steve N. Harp and Anthony J. Cutezo for their constructive comments and invaluable advice.

I would like to thank my mother and father for their encouragement. Finally, I would like to thank Adrienne S. Howard for being so supportive and understanding throughout this endeavor.

This material is based upon work supported by the Office of Naval Research, under contract No. N00014-00-G-0058, Delivery Order No. DN BOA-12.

## Chapter 1

### Introduction

#### 1.1 Motivation

The detection of a scatterer and the estimation of its parameters are some of the main goals of active sonar. Sonar waveforms are transmitted into the ocean, and their echo signals are processed for information pertaining to range and velocity characteristics of any scatterers, that the signals encounter [36]. The ability to successfully estimate these scatterer parameters in different situations depends on the sonar waveforms used to gather this information. Some waveforms have good delay (or range) resolution but poor Doppler (or velocity) resolution, while others exhibit excellent Doppler resolution but inferior delay resolution. Some waveforms perform well in the presence of reverberation, while others are good at distinguishing between multiple scatterers closely spaced in delay and Doppler. Since different sonar waveforms are better suited for different situations and estimating certain scatterer parameters, it is beneficial to use multiple sonar waveforms to interrogate a given scatterer.

The parameters of a scatterer can change over time. Although, the interrogation of a scatterer with multiple sonar signals over different time intervals may have some benefit, it is more useful to simultaneously transmit several waveforms, because they estimate the scatterer parameters for a specific event. Since transmission time is limited in monostatic sonar, the simultaneous transmission of multiple sonar waveforms also maximizes transmission time, which in turn maximizes the Doppler resolution of the sonar waveforms [15].

Although, several methods do exist to simultaneously transmit multiple waveforms, some of the most widely known ones come from the field of radio. They are amplitude modulation, which is the modulation of a carrier waveform's amplitude with multiple waveforms, and angle modulation, which is the modulation of a carrier waveform's phase with multiple waveforms. While both modulation techniques provide viable methods of simultaneously transmitting multiple sonar waveforms, amplitude modulation experiences total transmit energy losses in peak power limited systems [30]. These

energy losses present problems for amplitude modulation, since scatterer detection depends on the transmit level [36].

Phase modulation (a subset of angle modulation) provides a method for transmitting multiple sonar waveforms simultaneously, while maximizing transmit time and avoiding amplitude modulation. Phase modulation is the linear combination of multiple waveforms as the modulating phase component of a carrier waveform [41]. When the modulating waveforms are designed to be spectrally separable by filtering techniques, the modulating signals can be individually processed upon reception and demodulation. The application of this technique in active sonar is referred to as sub-band modulation, which was first proposed by L. H. Sibul [30].

This thesis presents a discussion of modulation theory, as it applies to sub-band modulation. Different modulation techniques are compared, and a detailed analysis of the sub-band modulation and demodulation processes is made. Furthermore, the waveform design considerations for both the sub-band waveforms and the overall modulation are presented, and sub-band modulation theory is implemented as a process in Matlab. Both simulated and in-water experiments are conducted to investigate the effects of scatterer velocity, sub-band modulating signal type, signal-to-interference ratio and demodulation conditions on the performance of sub-band modulating signals, and to demonstrate the application of sub-band modulation in active sonar.

## 1.2 Literature Review

The coupling of sonar, signal processing and modulation theory provided the basis of sub-band modulation theory. This is because the concepts behind sub-band modulation are not new, only the application is. Therefore, a wide variety of sources were utilized to construct the theoretical background for this thesis.

Numerous sonar and sonar signal processing sources were employed in this thesis to provide a solid background in sonar theory and the motivation behind sub-band modulation. Some sources provided a detailed background in underwater propagation and sonar theory [3, 23, 36], while others provided insight into the benefits of different sonar waveforms [4, 15, 32]. Still other sources provided an excellent insight into sonar signal processing [1, 5, 11, 35, 37, 38].

Extensive resources exist on the topic of modulation theory. Since modulation theory was exhaustively researched through out the twentieth century because of its applications in radio, a vast array of literature can be found, that present comprehensive

overviews on both amplitude and angle modulation [2, 13, 27, 29, 41]. Other more specific sources focus on the effects of noise on modulation [9, 19, 28, 40].

### 1.3 Thesis Outline

Chapter 2 presents an in-depth background into active sonar and the motivation behind sub-band modulation. The active sonar background provides insight into the effects of scatterer parameters and underwater sound propagation on the echo signal. A discussion of echo processing is then presented to illustrate the process of estimating these parameters from received echo signals. This is followed by a comparison between several sonar waveforms and a discussion of their advantages and disadvantages in various situations. Finally, the motivation behind sub-band modulation is presented, as a culmination of the ideas presented in the previous sections.

A comprehensive discussion of modulation theory and its application to sub-band modulation is given in chapter 3. First, an overview of amplitude modulation is presented to illustrate its limitations. An overview of angle modulation was then discussed, and its subsets (frequency and phase modulation) were compared to amplitude modulation. This provides a clear definition of sub-band modulation, along with an explanation of its advantages in active sonar over other types of modulation. Next, specific characteristics of sub-band modulation were examined and discussed. Chapter 3 ends with an analysis of the demodulation of sub-band modulating signals for processing. The overall demodulation process is first presented, then the effects of delay and Doppler on demodulation are analyzed, and finally, demodulation in the presence of interference is discussed.

In chapter 4, the experimental portion of this thesis is presented. First, a detailed description of the factors influencing sub-band waveform design are discussed, along with the waveform design process that takes them into account. This is followed by the presentation and analysis of the sub-band waveforms used in this experiment, and the motivation behind each waveform combination is examined. Next, the implementation of sub-band modulation theory as a series of Matlab processes is explained. A step by step description of the simulations in this thesis is presented in the following section, which focuses on the setup of the different experiments and their goals. A similar description of the in-water experiment portion of this thesis concludes this chapter.

Chapter 5 consists of a discussion of the results of the experiments described in chapter 4. First, the results from each of the simulations were incrementally presented and analyzed. This analysis is then used to characterize the detection performance of the

sub-band modulated signals, as compared to the performance of equivalent unmodulated signals. The results from the in-water experiment are then discussed and analyzed. These results were then compared with the simulation results to confirm the detection performance of the sub-band modulated signals observed in the simulations.

## Chapter 2

### Sonar Theory and Motivation

A thorough background in active sonar, sonar signal processing and the motivation behind sub-band modulation is warranted to better understand sub-band modulation and its role in active sonar. First, active sonar theory is presented in order to illustrate the resulting effects of scatterer parameters on the received echo signal. Second, the echo processing techniques used to estimate these scatterer parameters from the echo signal are discussed. Third, several sonar waveforms are compared in order to bring to light the advantages and disadvantages of different sonar waveforms. Finally, active sonar theory, echo processing and the characteristics of different sonar waveforms are combined together to motivate and begin to define sub-band modulation.

#### 2.1 Active Sonar Background

Active sonar is the interrogation of the ocean environment with acoustic signals to detect the presence of possible scatterers from backscattered echos and to estimate scatterer parameters, such as velocity and range [3, 15, 36]. A sonar waveform has the form

$$\begin{aligned} f(t) &= [a(t) \exp(j\psi(t))] \exp(j\omega_0 t) \\ &= \tilde{f}(t) \exp(j\omega_0 t) \end{aligned} \quad t \in (0, T), \quad (2.1)$$

where  $\tilde{f}(t)$  denotes the complex envelope of the waveform and contains all of the phase and amplitude information. The analytic representation of the real waveform is given by

$$\Re\{f(t)\} = a(t) \cos(\psi(t) + \omega_0 t), \quad (2.2)$$

where  $\omega_0$  is the frequency of the carrier term,  $a(t)$  represents the amplitude of the signal and  $\psi(t)$  represents the phase [5, 11, 35, 39]. Sonar waveforms by convention are



normalized to unit energy,

$$\int_{-\infty}^{\infty} |\tilde{f}(t)|^2 dt = \int_0^T a^2(t) dt = 1 \quad (2.3)$$

[30, 35, 38], so that the transmitted signal with energy  $e_o$  is

$$\begin{aligned} s_t(t) &= \sqrt{e_o} \Re\{f(t)\} \\ &= \sqrt{e_o} a(t) \cos[\omega_0 t + \psi(t)]. \end{aligned} \quad (2.4)$$

The received signal is the combination of the echo signal and additive interference, consisting of white Gaussian noise and reverberation measured at the receiver [1, 11, 35]. This signal is modeled as

$$r(t) = s(t) + n(t), \quad (2.5)$$

where  $s(t)$  is the echo signal and  $n(t)$  is the interference. The simplest backscatter model for the returning echo signal is the point reflector in a homogeneous environment, where the echo signal is an attenuated, time delayed and possibly Doppler shifted replica of the transmitted waveform [15, 23, 35]. The echo signal is

$$s(t) = \sqrt{e_o} \int_{\beta} \int_{\tau} \sqrt{\beta'} S_s(\beta', \tau') f[\beta'(t - \tau')] d\tau' d\beta', \quad (2.6)$$

where  $S_s(\beta', \tau')$  is the echo spreading function [15, 22]. The echo spreading function is the random weighting of the echo signal, that accounts for the scatterer-influenced attenuation, delay and Doppler changes in the echo.  $S_s(\beta', \tau')$  for a point scatterer with dilation  $\beta$  and delay  $\tau$  (commonly known as a slowly fluctuating point scatterer) is

$$S_s(\beta, \tau) = S_s \delta(\beta' - \beta) \delta(\tau' - \tau) \quad (2.7)$$

[23, 38], where  $S_s$  has a random Rayleigh magnitude with uniform phase that remains constant over each interrogation interval ( $S_s = |S_s| \exp(j\theta)$ ) [15, 35]. (2.5) can be rewritten to incorporate the spreading function of the slowly fluctuating point scatterer

using (2.7) as

$$\begin{aligned}
 r(t) &= \sqrt{e_o} \int_{\beta} \int_{\tau} \sqrt{\beta'} S_s \delta(\beta' - \beta) \delta(\tau' - \tau) f[\beta'(t - \tau')] d\tau' d\beta' + n(t) \\
 &= \sqrt{e_o} \beta S_s f(\beta(t - \tau)) + n(t) \\
 &= \sqrt{e_o} S_s f(\mathbf{p}, t) + n(t),
 \end{aligned} \tag{2.8}$$

where  $f(\mathbf{p}, t)$  is the wideband Doppler model of the echo waveform, and  $\mathbf{p}$  represents the delay and Doppler parameters,  $[\beta, \tau]$ .  $n(t)$  is white Gaussian noise with a power spectral density of  $N_o$ , when noise is the dominant form of interference [23]. Reverberation can dominate the interference, and this possibility will be further discussed later in this section. The magnitude of the echo signal is also affected by equipment and transmission medium influenced parameters. These attenuation parameters can be incorporated into the variable  $S_s$ , along with target strength.

The wideband Doppler model of the received echo signal can be rewritten in the form of (2.1), where

$$\begin{aligned}
 s(t) &= \sqrt{e_o} S_s f(\mathbf{p}, t) \\
 &= \sqrt{e_o} \beta S_s f(\beta(t - \tau)) \\
 &= \sqrt{e_o} \beta S_s \tilde{f}_t(\beta(t - \tau)) \exp(j\omega_0 [\beta t - \tau]),
 \end{aligned} \tag{2.9}$$

$\tau$  is the time delay, and  $\beta$  is the dilation factor, represented by

$$\begin{aligned}
 \beta &= \left( \frac{c + v_s}{c - v_s} \right) \left( \frac{c + v_p}{c - v_p} \right) \\
 &\approx \left( 1 + \frac{2v_s}{c} \right) \left( 1 + \frac{2v_p}{c} \right) \\
 &\approx \left( 1 + \frac{2[v_s + v_p]}{c} \right) \\
 &\approx 1 + \frac{2v_l}{c}.
 \end{aligned} \tag{2.10}$$

[1, 22, 38].  $v_p$  is the platform velocity,  $v_s$  is the scatterer velocity, and  $v_l$  is the relative line-of-sight velocity between the platform and scatterer, which is positive when the range between the platform and the scatterer is closing and negative when it is opening.

The receiving and transmitting transducers are colocated for a monostatic sonar [36], so that the round trip delay is

$$\tau = \frac{2R}{c}, \quad (2.11)$$

where  $R$  is the distance to the scatterer and  $c$  is the speed of sound [15, 35, 39]. The range and scatterer velocity are estimated by measuring the dilation factor and time delay of the echo signal.

Equation (2.9) illustrates the compression or dilation of the time scale of the complex envelope and the frequency shift of the carrier frequency. It can be rewritten as

$$s(t) = \sqrt{e_o} \beta S_s \tilde{f}(\beta(t - \tau)) \exp(j\omega_0(t - \tau)) \exp(j2\pi\phi t) \quad (2.12)$$

by separating the delay and dilation components of the carrier. The shift in the carrier frequency caused by the motion of the scatterer relative to the sonar platform is

$$\phi = \frac{2v_l \frac{\omega_0}{2\pi}}{c}, \quad (2.13)$$

and is known as the Doppler frequency [35, 38].

The signal (2.12) may be simplified, provided the scatterer does not travel a greater distance than the range resolution during the time of its illumination by the sonar signal. This requires that

$$\frac{2v_l}{c} \ll \frac{1}{TW} \quad (2.14)$$

or  $|v_l| \ll c$  to unambiguously resolve a scatterer [25, 32, 35, 38]. Here,  $T$  is the signal duration, and  $W$  is its bandwidth. When (2.14) is met, the signal is considered narrowband, and the time scale compression or dilation of the received signal envelope can be approximated by a frequency shift. The narrowband Doppler model assumes, the scatterer velocity is small enough, so that the entire bandwidth experiences essentially the same Doppler shift. The narrowband Doppler model of the received echo signal is then

$$s(t) \approx \sqrt{e_o} S_s f(t - \tau) \exp(j2\pi\phi t) \quad (2.15)$$

[1, 15, 22, 35, 38]. This method is less computationally intensive than the wideband model, but if the narrowband criteria are not met, it can yield incorrect velocity information and decreased detection performance [25].

## 2.2 Echo Processing

The effects of the scatterer's range from the sonar platform and line-of-sight velocity on an echo signal were discussed in section 2.1. Now, methods of extracting this information from the echo signal are presented.

A matched filter is the optimum maximum likelihood detector for a slowly fluctuating point scatterer in white Gaussian noise. Although it is optimum only under these conditions, it is a robust process because it can yield useful results for less optimum conditions [3, 26, 36, 35, 39]. The matched filter or the replica correlator for the narrowband and wideband Doppler models are

$$|\ell_{nb}|^2 = \left| \int_{-\infty}^{\infty} r(t) f^*(t - \hat{\tau}) \exp(-j2\pi\hat{\phi}t) dt \right|^2 \quad (\text{Narrowband}) \quad (2.16)$$

$$|\ell_{wb}|^2 = \hat{\beta} \left| \int_{-\infty}^{\infty} r(t) f^*[\hat{\beta}(t - \hat{\tau})] dt \right|^2 \quad (\text{Wideband}) \quad (2.17)$$

[25, 35, 39]. The matched filter is implemented as the correlation of the received signal with a bank of time delayed and Doppler shifted replicas of the transmitted signal, where  $\hat{\tau}$ ,  $\hat{\phi}$  and  $\hat{\beta}$  are the delay, Doppler and dilation factor hypotheses [12]. The points of high correlation yield peaks in the phase plane (delay-Doppler plane). This indicates, that the received signal closely matches the hypothesized delay and Doppler of the replica [15, 35]. Furthermore, the shape of this peak is determined by the transmitted waveform, which is discussed in more detail later in this section.

The detection criteria of the matched filter are

$$|\ell|^2 > \gamma \Rightarrow H_1 \quad (2.18)$$

$$|\ell|^2 < \gamma \Rightarrow H_0, \quad (2.19)$$

where  $|\ell|^2$  can be either  $|\ell_{nb}|^2$  or  $|\ell_{wb}|^2$ .  $H_0$  and  $H_1$  are detection hypotheses and  $\gamma$  is the detection threshold [11, 20, 33].  $H_1$  is the hypothesis, that the sonar signal is present

in the received data, and  $H_0$  is the hypothesis, that only noise is present. If  $|\ell|^2 > \gamma$ , then hypothesis  $H_1$  is declared, and if  $|\ell|^2 < \gamma$ , then hypothesis  $H_0$  is declared.

According to the detection hypotheses, the two possible received signals are

$$\begin{aligned} r(t) &= s(t) + n(t) && \text{for } H_1 \\ r(t) &= n(t) && \text{for } H_0 \end{aligned}$$

[15, 11, 24, 35]. The expected matched filter output for hypothesis  $H_1$  for the wideband Doppler model (2.17) is

$$E \left\{ |\ell_{wb}|^2 | H_1 \right\} = E \left\{ \left| \int_{-\infty}^{\infty} (s(t) + n(t)) f^*(\hat{\mathbf{p}}, t) dt \right|^2 \right\}, \quad (2.20)$$

where  $\hat{\mathbf{p}} = [\hat{\beta}, \hat{\tau}]$ . Since  $E \{|x|^2\} = E \{xx^*\}$  [20], (2.20) becomes

$$E \left\{ |\ell_{wb}|^2 | H_1 \right\} = E \left\{ \left[ \int_{-\infty}^{\infty} (s(t) + n(t)) f^*(\hat{\mathbf{p}}, t) dt \right] \left[ \int_{-\infty}^{\infty} (s(u) + n(u)) f^*(\hat{\mathbf{p}}, u) du \right]^* \right\}.$$

$s(t)$  and  $n(t)$  are uncorrelated, so the cross terms cancel, yielding

$$\begin{aligned} E \left\{ |\ell_{wb}|^2 | H_1 \right\} &= E \left\{ \int_{-\infty}^{\infty} \int_{-\infty}^{\infty} s(t) s^*(u) f^*(\hat{\mathbf{p}}, t) f(\hat{\mathbf{p}}, u) dudt \right\} \\ &\quad + E \left\{ \int_{-\infty}^{\infty} \int_{-\infty}^{\infty} n(t) n^*(u) f^*(\hat{\mathbf{p}}, t) f(\hat{\mathbf{p}}, u) dudt \right\}. \end{aligned} \quad (2.21)$$

The correlation of white Gaussian noise with a power spectral density of  $N_o$  is

$$E \left\{ n(t) n^*(u) \right\} = N_o \delta(t - u) \quad (2.22)$$

[11, 35]. Therefore, the expected matched filter output for an echo signal backscattered from a point scatterer is

$$\begin{aligned}
 E \left\{ |\ell_{wb}|^2 | H_1 \right\} &= E \left\{ \left| \int_{-\infty}^{\infty} s(t) f^*(\hat{\mathbf{p}}, t) dt \right|^2 \right\} + E \left\{ N_o \left| \int_{-\infty}^{\infty} f^*(\hat{\mathbf{p}}, t) dt \right|^2 \right\} \\
 &= E \left\{ \left| \int_{-\infty}^{\infty} \sqrt{e_o} S_s f(\mathbf{p}, t) f^*(\hat{\mathbf{p}}, t) dt \right|^2 \right\} \\
 &\quad + E \left\{ N_o \left| \int_{-\infty}^{\infty} f^*(\hat{\mathbf{p}}, t) dt \right|^2 \right\}. \quad (2.23)
 \end{aligned}$$

The noise term reduces to  $N_o$ , because the waveform is normalized to unity [40], and (2.23) becomes

$$E \left\{ |\ell_{wb}|^2 | H_1 \right\} = E_s \left| \int_{-\infty}^{\infty} \sqrt{\beta \hat{\beta}} f(\beta(t - \tau)) f^*(\hat{\beta}(t - \hat{\tau})) dt \right|^2 + N_o \quad (2.24)$$

[22, 35], where  $E_s$  is the expected value of the received signal energy,

$$E_s = e_o E \left\{ |S_s|^2 \right\}. \quad (2.25)$$

When a spread scatterer is assumed instead of a point scatterer, (2.24) takes on the more general form

$$E \left\{ |\ell_{wb}|^2 | H_1 \right\} = e_o \int_{-\infty}^{\infty} \int_{-\infty}^{\infty} R_s(\beta, \tau) \left[ \left| \int_{-\infty}^{\infty} \sqrt{\beta \hat{\beta}} f(\beta(t - \tau)) f^*(\hat{\beta}(t - \hat{\tau})) dt \right|^2 \right] d\tau d\beta + N_o, \quad (2.26)$$

where  $R_s(\beta, \tau) = E \left\{ |S_s(\beta, \tau)|^2 \right\}$  is the scattering function for a spread scatterer [26].

Knight et al. [15] recommend considering the matched filter process in the absence of noise, because the properties of the matched filter depend upon the transmitted signal. The output of the wideband matched filter normalized to unit energy in the absence of

noise is known as the wideband ambiguity function [5, 15], and its standard form is

$$\Phi_{ff}(\tilde{\beta}, \tilde{\tau}) = \tilde{\beta} \left| \int_{-\infty}^{\infty} f(u) f^* [\tilde{\beta}(u - \tilde{\tau})] du \right|^2. \quad (2.27)$$

(2.27) is the correlation of the time dilated and delayed waveform and the bank of replicas [1, 25, 31, 40, 38]. Equation (2.24) can be rewritten as a function of the standard form of the wideband ambiguity function by changing the variables to  $u = \beta(t - \tau)$ ,  $\tilde{\beta} = \frac{\hat{\beta}}{\beta}$  and  $\tilde{\tau} = \beta(\tau - \hat{\tau})$ . Then, (2.24) becomes

$$E \left\{ |\ell_{wb}|^2 |H_1 \right\} = E_s \Phi_{ff}(\tilde{\beta}, \tilde{\tau}) + N_0 \quad (2.28)$$

for a point scatterer. The narrowband case  $\left( E \left\{ |\ell_{nb}|^2 |H_1 \right\} \right)$  has the same form as the wideband output  $\left( E \left\{ |\ell_{wb}|^2 |H_1 \right\} \right)$ , except that the narrowband ambiguity function

$$\Phi_{ff}(\hat{\phi}, \hat{\tau}) = \left| \int_{-\infty}^{\infty} f(t) f^*(t - \hat{\tau}) \exp(-j2\pi\hat{\phi}t) dt \right|^2 \quad (2.29)$$

is implemented [1, 5, 15, 26, 37, 38]. When only the noise is present (2.19), the expected output of the matched filter is

$$E \left\{ |\ell_{wb}|^2 |H_0 \right\} = E \left\{ \hat{\beta} \left| \int_{-\infty}^{\infty} n(t) f^* [\hat{\beta}(t - \hat{\tau})] dt \right|^2 \right\} = N_0, \quad (2.30)$$

as seen in (2.24). The signal-to-interference ratio at the matched filter output  $(SIR_o)$  can then be calculated using (2.28) and (2.30),

$$SIR_o = \frac{E \left\{ |\ell_{wb}|^2 |H_1 \right\}}{E \left\{ |\ell_{wb}|^2 |H_0 \right\}} - 1 = \frac{E_s \Phi_{ff}(\hat{\beta}, \hat{\tau})}{N_o}, \quad (2.31)$$

which is also known as the detection index [5, 15, 26, 35]. The probability of detection  $P_d$  for a fixed probability of false alarm  $P_f$  is

$$P_d = P_f^{\frac{1}{1+SIR_o}} \quad (2.32)$$

[26, 35]. Therefore, a high detection index typically results in a strong detection and a high level of confidence in the estimated scatterer parameters.

(2.28) is a convolutional relationship between the scattering function and ambiguity function in the delay-Doppler plane, which can be seen when the expected matched filter response from a spread scatterer (2.26) is written in terms of the ambiguity function (2.27):

$$\begin{aligned} E \left\{ \left| \ell_{wb} \right|^2 | H_1 \right\} &= e_o \int_{-\infty}^{\infty} \int_{-\infty}^{\infty} R_s(\beta, \tau) \Phi_{ff}(\tilde{\beta}, \tilde{\tau}) d\tau d\beta + N_o \\ &= e_o \left( R_s(\beta, \tau) ** \Phi_{ff}(\tilde{\beta}, \tilde{\tau}) \right) + N_o \end{aligned} \quad (2.33)$$

[10, 23]. Therefore, the peak in the matched filter response indicates the delay-Doppler location of the overlap between the scattering function and the ambiguity function of the transmitted signal. The expected matched filter output is at a maximum, when the delay and dilation of the echo signal matches the replica  $(\hat{\beta}, \hat{\tau} = \beta, \tau)$ , and  $(E \left\{ \left| \ell_{wb} \right|^2 | H_1 \right\})$  becomes

$$E \left\{ \left| \ell_{wb} \right|^2 | H_1 \right\} = E_s + N_o, \quad (2.34)$$

which yields a peak in the phase plane at  $(\beta, \tau)$ . This also illustrates the importance of the ambiguity function in the matched filter response, from which the scatterer's parameters are estimated.

The matched filter response depends heavily upon the ambiguity function, as seen in (2.28). The estimated scatterer parameters are defined by the delay-Doppler location of the matched filter peak. The peak covers a range of delay and Doppler values, within which the ambiguity function still yields a significant magnitude relative to the maximum response, as seen in figure 2.1 [32]. This area in the phase plane is known as the mainlobe, and it represents the uncertainty of the delay and Doppler estimates for the scatterer. The mainlobe region is defined as the area within the half power points of  $\Phi_{ff}(\phi, \tau)$ , which is the delay-Doppler cross-section of the ambiguity function 3dB down from the peak, and this is the resolution area of the ambiguity function for a given waveform [4, 32]. Therefore, the resolution of the delay and Doppler estimates depends upon the shape of the matched filter peak, and the shape of the peak is determined by the ambiguity function, which is unique to each sonar signal [5, 32, 37].



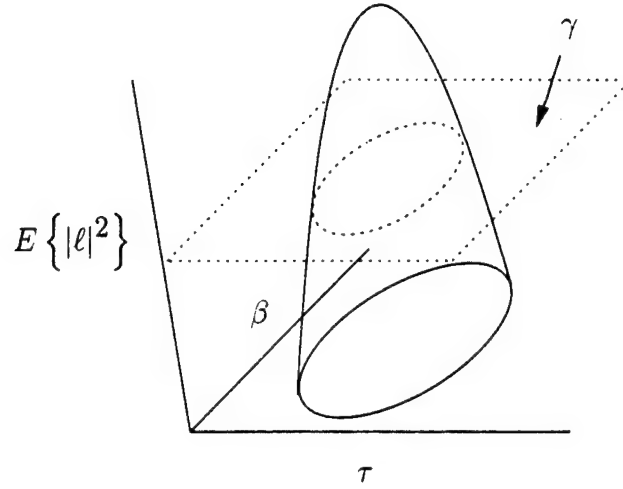


Fig. 2.1. Example of the Region of Signal Ambiguity of an Ambiguity Function (dotted line indicates the ambiguity function at threshold)

Ideally, a thumbtack ambiguity function that approaches a delta function yields more accurate parameter estimations [1, 10, 22, 35], because narrower ambiguity function peaks provide more localized delay and Doppler estimates. However, ambiguity functions exhibit a conservation of volume property, which states that narrowband signals with unity normalized energy have ambiguity functions with unity volume [5, 15, 26, 32, 37]. Therefore, narrowing the mainlobe results in higher sidelobe levels, which can result in several sidelobes above the detection threshold, for some waveforms. The advantages and disadvantages of different ambiguity functions are discussed in section 2.3.

### 2.3 General Waveform and Ambiguity Function Characteristics

A wide variety of waveforms are implemented in active sonar. For the purpose of this thesis, three types of sonar waveforms are considered: the continuous waveform (CW), the linear frequency modulated waveform (LFM) and the biphasic shift keyed waveform (BPSK). Each individual waveform has specific attributes, that make them advantageous for producing particular echo information. These attributes are demonstrated by examining the ambiguity functions of the different sonar waveforms.

The discrimination of scatterers that are separated in delay and Doppler depends upon the resolution of the sonar waveforms [5, 15]. The narrowband Doppler resolution

is

$$\Delta\phi_r = \left( \frac{2\Delta v_l}{c} \right) \frac{\omega_0}{2\pi} \approx \frac{1}{T}, \quad (2.35)$$

and the delay resolution is

$$\Delta\tau_r = \left( \frac{2\Delta r}{c} \right) \approx \frac{1}{W} \quad (2.36)$$

[10, 15, 32, 35, 37]. The accuracy of delay and Doppler estimates gathered with a matched filter is bounded by the resolution of a given sonar signal. Different signals are better at discriminating between delay and Doppler due to their length in time and their bandwidth [1], but the shape of the peak in the ambiguity function is more crucial for making unambiguous measurements, as discussed in section 2.2.

The continuous waveform (CW) or sinewave (2.1) has the form

$$f(t) = a(t) \exp(j\omega_0 t), \quad (2.37)$$

when  $\psi(t) = 0$  [15, 30]. Its time series and frequency spectrum are illustrated in figures 2.2a and b. Sinewaves have a time bandwidth product of unity ( $TW = 1$ ), which

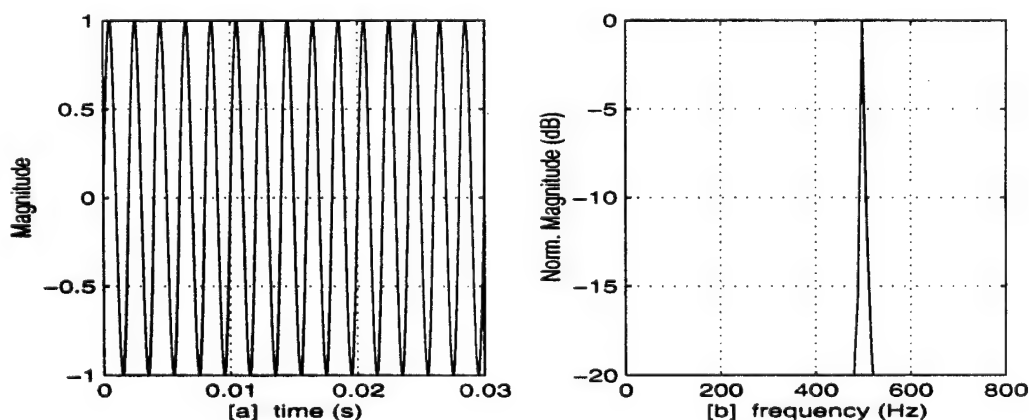


Fig. 2.2. Example CW with Center Frequency of 500Hz: [a] Time Series and [b] Frequency Spectrum

influences their ambiguity functions (figures 2.3 and 2.4) [10, 32]. The ambiguity function

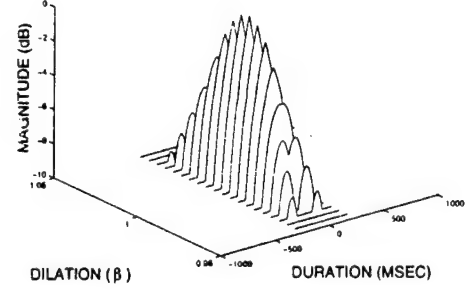
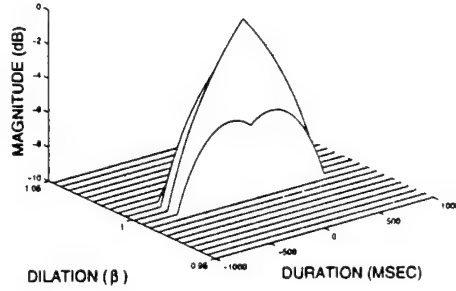


Fig. 2.3. Long CW Ambiguity Function Fig. 2.4. Short CW Ambiguity Function

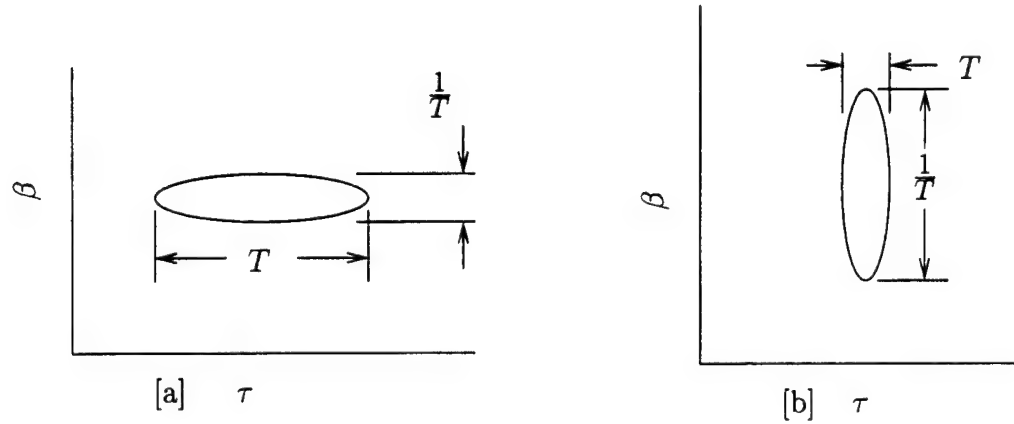


Fig. 2.5. Ambiguity Function Cross-Sections: [a] Long CW, [b] Short CW

peak for a sinewave is spread in delay for the time duration of the signal ( $T$ ) and spread in Doppler according to the bandwidth of the signal ( $W = \frac{1}{T}$ ). This results in a CW with a large  $T$  correlating over a large range of delays but only a small range of frequencies, as seen in figure 2.5a [4, 32]. If the CW has a relatively short  $T$ , then it correlates over only a small range of delays but over a large range of frequencies, as seen in figure 2.5b. The CW can have good Doppler resolution with a longer CW or good range resolution with a shorter CW, but not both simultaneously [15].

The LFM is a sinewave with a linearly increasing frequency component  $\dot{\psi}(t) = \frac{2\pi Wt}{T}$ , and the waveform is

$$f(t) = a(t) \exp\left(j\frac{\pi Wt^2}{T}\right) \exp(j\omega_0 t) \quad t \in (0, T), \quad (2.38)$$

shown in figures 2.6a and b [5, 10, 15, 30]. The LFM time bandwidth product is not unity,

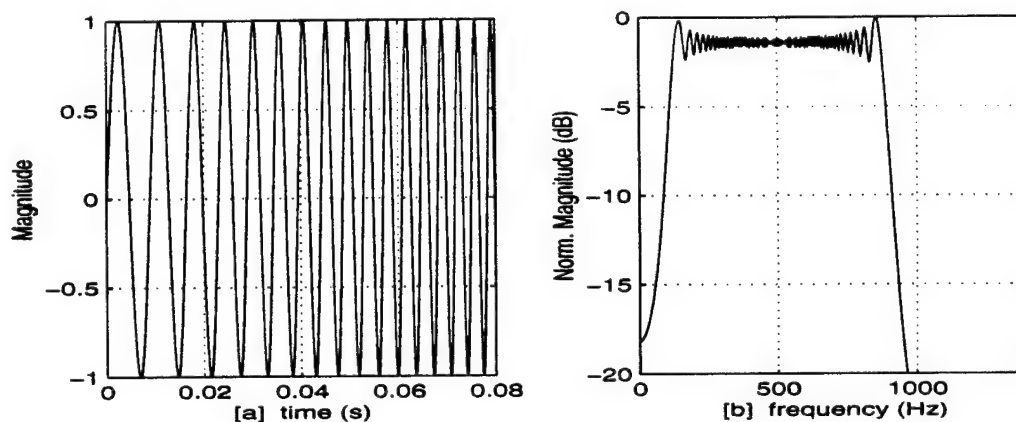


Fig. 2.6. Example LFM with Center Frequency of 450Hz and a Bandwidth of 800Hz: [a] Time Series and [b] Frequency Spectrum

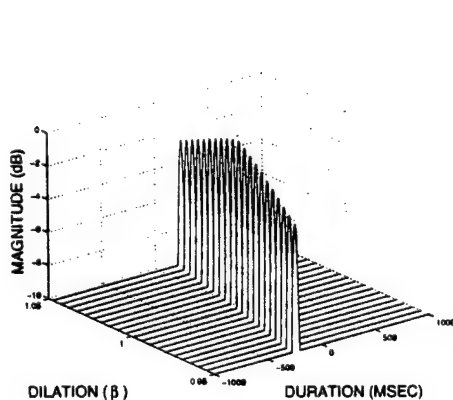


Fig. 2.7. LFM Ambiguity Function

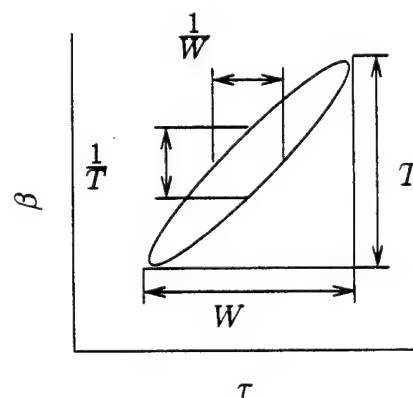


Fig. 2.8. LFM Ambiguity Function Cross-Section

and typically  $TW \gg 1$  [15, 32]. Since the frequency of the LFM increases linearly with time, the LFM correlates over short time intervals at different frequency intervals, which result in a diagonal ambiguity function peak across the phase plane with an overall mainlobe frequency range of  $W$  and a delay range of  $T$ , as seen in figures 2.7 and 2.8 [4, 5, 23, 32]. The LFM is not a good joint estimator of both delay and Doppler parameters, because it is highly skewed in the delay-Doppler plane. The minimum variance of the ambiguity function estimation in delay and Doppler depends upon

$$\Phi_{ff}(\beta, -\tau) = \Phi_{ff}(\beta, \tau), \quad (2.39)$$

which is satisfied by even symmetric waveform functions [21]. When (2.39) is satisfied, the waveform is said to be uncoupled, and the variance of the delay and Doppler estimations are minimal. Otherwise, the waveform is coupled, and this coupling is represented by the slope in the ambiguity function [7]. Therefore, the LFM is a highly coupled waveform, so the joint delay and Doppler estimates for a LFM can not be localized better than  $T$  and  $W$ , if both of the parameters are unknown [5, 35]. However, if one of the parameters is already known ( $\phi$  or  $\tau$ ), the other can be estimated with a much higher resolution ( $\frac{1}{W}$  or  $\frac{1}{T}$ ) [32].

The BPSK is a combination of CW chips at the same frequency, that are phase shifted by  $\pm 180^\circ$  according to a pseudo-random code in order to create a broadband waveform that appears noise-like, as seen in figures 2.9a and b [22]. The 3dB bandwidth of the BPSK is  $W \approx \frac{N}{T}$ , where  $N$  is the length of the pseudo-random code sequence (or number of chips). An  $M$  stage shift register generates the code sequence of length  $N = 2^M - 1$ , that shifts between  $\pm 180^\circ$  and repeats for each chip [16, 22]. The frequency spectrum of a BPSK waveform appears similar to a sinc function ( $\text{sinc}(x) = \sin(x)/x$ ), where the mainlobe has the bandwidth of  $W$ , and the first set of sidelobes are approximately 13dB down, as seen in figure 2.9b. The BPSK has very good joint frequency and delay resolution ( $\frac{1}{T}, \frac{1}{W}$ ), because it's ambiguity function has an exceptionally localized mainlobe (figures 2.10 and 2.11). Furthermore, it is uncoupled in delay and Doppler, when the complex spectrum of the BPSK is even and satisfies (2.39). The phase plane area of the mainlobe of the ambiguity function for the BPSK is  $\frac{1}{TW}$ , which can be very high resolution [4, 32]. This higher resolution can make it more computationally intensive to search the phase plane for detection peaks, and it results in a very large sidelobe region for the BPSK.

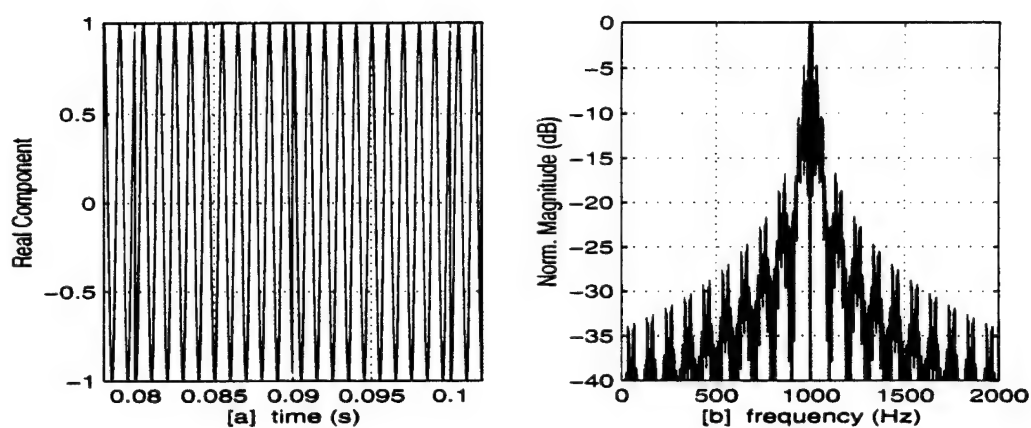


Fig. 2.9. Example BPSK consisting of 30 Chips with Center Frequency of 1kHz and a Bandwidth of 100Hz : [a] Time Series and [b] Frequency Spectrum

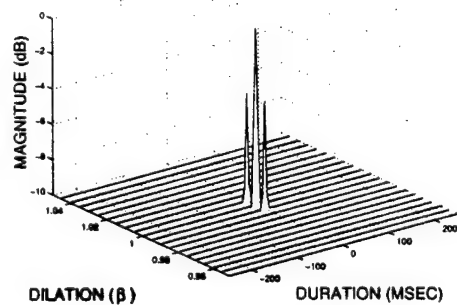


Fig. 2.10. BPSK Ambiguity Function

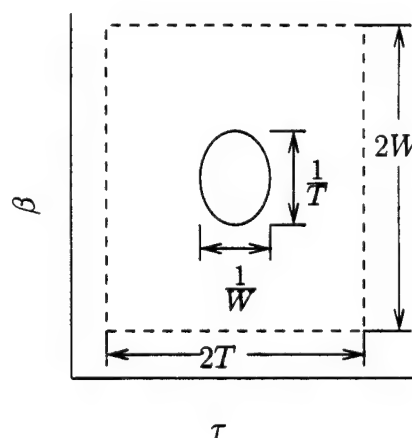


Fig. 2.11. BPSK Ambiguity Function Cross-Section (solid line is the mainlobe region, dashed line is the sidelobe region)

The detection of a scatterer in reverberation and the detection of multiple scatterers closely spaced in delay and Doppler (or a spread scatterer) are two particular circumstances, that illustrate some of the advantages and disadvantages of different sonar signals. Reverberation is backscattered energy from discontinuities, boundaries and the volume in the ocean [3, 35]. These discontinuities range from water-born particulates to biological sources and from surface interactions to bottom backscattering. Reverberation is represented by the scattering function

$$R_r(\tau, \phi) = E \left\{ \left| S_r(\tau, \phi) \right|^2 \right\} \quad (2.40)$$

[23].  $S_r(\tau, \phi)$  is the reverberation spreading function, which is similar to (2.25), except that it accounts for the spread scattering from all of the ocean inhomogeneities encountered instead of just a point scatterer. The expected matched filter response for reverberation is

$$\begin{aligned} E \left\{ |\ell|^2 \right\} &= e_o \left( R_r(\tau, \phi) ** \Phi_{ff}(\hat{\phi}, \hat{\tau}) \right) \\ &= e_o \int_{-\infty}^{\infty} \int_{-\infty}^{\infty} R_r(\tau, \phi) \Phi_{ff}(\hat{\phi}, \hat{\tau}) d\phi d\tau \\ &= e_o \int_{-\infty}^{\infty} \int_{-\infty}^{\infty} E \left\{ \left| S_r(\tau, \phi) \right|^2 \right\} \Phi_{ff}(\hat{\phi}, \hat{\tau}) d\phi d\tau, \end{aligned} \quad (2.41)$$

which is the same form as the scattering from a spread scatterer (2.33) [23, 35]. Reverberation is the dominant form of interference at short ranges from the sonar platform, but its magnitude decays with range, like all backscattered signals [36]. Once a range has been reached, where reverberation has decayed below the ambient noise level, noise becomes the dominant form of interference [23]. Reverberation occurs at low Doppler, because the discontinuities in the ocean are stationary or moving at very low velocities. Therefore, reverberation backscatter is confined to a band of width  $B_r$  around the transmit frequency over the entire receive interval in the phase plane, as seen in figures 2.12a and b [4, 23]. This Doppler bandwidth  $B_r$  is determined by the motion of the medium, and it can be modeled for the purpose of performance prediction as uniform over the entire bandwidth [23]. Since reverberation is often the main source of interference in active sonar [36], its effects need to be considered, when evaluating the utility of different sonar signals.

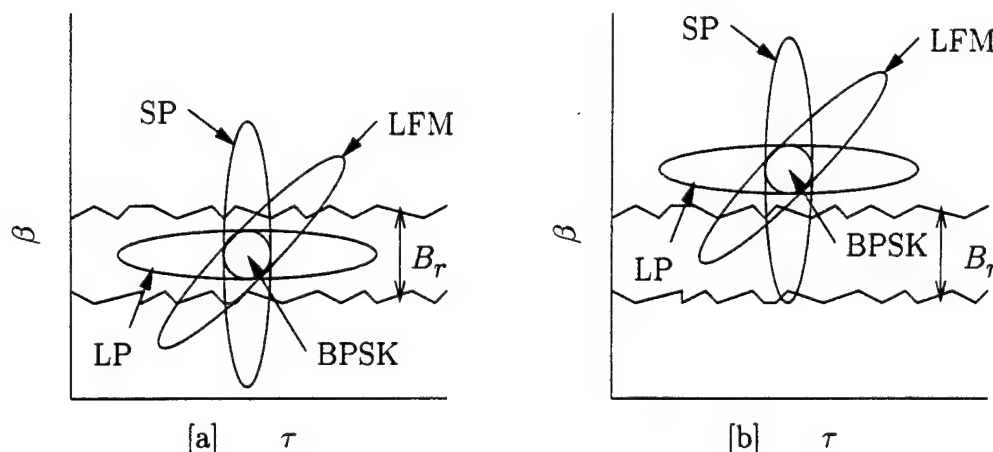


Fig. 2.12. Matched Filter Responses of Different Signals in Reverberation: [a] low Doppler scatterer, [b] high Doppler scatterer

High levels of reverberation can become prominent in matched filter responses, as seen in figures 2.12a and b. The degradation of the matched filter response due to reverberation is determined by the amount of overlap between the ambiguity function of the signal and the reverberation scattering function [4, 18, 35]. Therefore, a sonar with minimal overlap between  $\Phi_{ff}(\hat{\phi}, \hat{\tau})$  and  $R_r(\tau, \phi)$  in a given scenario is chosen to maximize detection [15]. The ambiguity function mainlobe is embedded in reverberation when the scatterer has a low velocity. The ambiguity function mainlobes of short CW or LFM signals are spread in Doppler to a length of  $W$ , which may not be completely embedded in reverberation, if  $B_r < W$  (figure 2.12a). The ambiguity functions of the short duration CW and LFM have less overlap with the reverberation scattering function than the long CW and BPSK, due to their Doppler spread mainlobes. Therefore, the effects of reverberation are minimized, and there is a greater chance that the scatterer parameters can be estimated from them [4, 15, 18, 35]. However, long CWs and BPSKs may provide better detection in high Doppler scenarios, because their mainlobes are less spread in Doppler (figure 2.12b). The long CW may have a sufficiently narrow bandwidth, such that its ambiguity function has negligible overlap with the reverberation scattering function at high Doppler [4, 18]. The mainlobe of the BPSK may also have minimal overlap with the reverberation scattering function, but its large sidelobe region will most likely overlap [15, 18, 35]. This makes the BPSK a less effective waveform for the detection of a high velocity scatterer than a long duration CW. However, it may still



be more effective than the LFM or the short CW, because its mainlobe can have less overlap with the reverberation scattering function.

The discrimination of multiple scatterers that are closely spaced in delay and Doppler is often of interest in active sonar. Signals with fine time resolution are needed to discriminate between multiple scatterers closely spaced in delay, and signals with high frequency resolution discriminate between multiple scatterers closely spaced in Doppler, as seen in (2.35) and (2.36). Clearly, a signal with good resolution in time and frequency is required to successfully discriminate individual scatterers closely spaced in delay and Doppler. For this reason, BPSKs are more appropriate than CW or LFM signals for the discrimination of multiple, closely spaced scatterers.

## 2.4 Motivation behind Sub-band Modulation

Careful waveform selection is required in order to accurately estimate the scatterer parameters under particular conditions. Therefore, different waveforms are needed to perform detection and estimation. It can be beneficial to transmit numerous active sonar signals at once, in order to gather more information about a scatterer. Numerous variations of signal combinations could be used to gather different types of echo information. An obvious choice is to transmit signals with good frequency resolution and signals with good time resolution together, in order to gather high resolution delay and Doppler information. Another alternative is to transmit a high resolution and low resolution signal together, in order to decrease detection complexity. A low resolution signal will result in a spread peak in the matched filter response, that does not localize well. The rough localization of delay and Doppler parameters of the scatterer can be made from the low resolution response, and applied to the match filtering of the high resolution signal. The computational requirements to search a large delay-Doppler region with a bank of high resolution matched filter replicas are considerably reduced by first isolating the scatterer with a low resolution matched filter. Knight [15] noted that, a combination of different sonar signals are usually transmitted to detect targets of various velocities. Therefore, a signal with good reverberation performance but low Doppler resolution and a signal with good Doppler resolution but poor reverberation performance is another possible signal combination. This signal combination allows for a detection to still be made in a high reverberation/low Doppler scenario, as well as achieve good Doppler information with a higher scatterer velocity. The desire to transmit multiple sonar signals together is one of the motivating factors behind sub-band modulation.

Transmission time is limited in monostatic sonar. There must be separate transmit and receive intervals, because the transmit and receive transducers are colocated (and are most likely the same transducers). Scatterers within the blind range

$$r_b = \frac{Tc}{2} \quad (2.42)$$

will not be detected, since signals can not be received while transmitting. The transmit interval is limited to minimize the blind range [30, 15]. However, it is beneficial to utilize the longest transmit time possible, because frequency resolution is proportional to the inverse of time (2.35). This presents a problem, when transmitting consecutive sonar signals during the same transmit interval, because the transmit time of each signal is limited even further. Maximizing the transmission time of each sonar signal is another motivation behind sub-band modulation.

One of the purposes of transmitting multiple sonar signals is to receive more echo information describing a specific event; for example, a scatterer's location and velocity at a given moment in time. The gathering of echo information with time separated sonar signals can differ between each interrogation due to the nonstationarity of echo parameters. The time separation of the sonar signals and the potential for a moving scatterer can result in echo information describing multiple events, as opposed to a specific event. Clearly, the most beneficial method of achieving this goal is through simultaneous signal transmission, which also provides the maximum transmission time for each sonar signal.

Transmit energy is another concern in active sonar. The transmit energy of the waveform is defined as

$$E_t = \int_0^T P(t) dt = \int_0^T [f_t(t)]^2 dt = \frac{1}{2} \int_0^T |\sqrt{e_o} \tilde{f}(t)|^2 dt, \quad (2.43)$$

where  $P(t)$  is the instantaneous transmitted power [11, 30]. However,  $E_t$  is energy only when the waveform is normalized (2.3). The  $\frac{1}{2}$  relates to the peak of the real transmitted waveform, and is dropped when the real waveform is normalized instead of the analytic waveform. A maximum operational level is set for each peak power limited, sonar projector. If this maximum level is surpassed, cavitation may occur. Cavitation is the formation and collapse of bubbles on the face of the sonar projector, which results in the deterioration of projector performance and an impedance mismatch

between the projector and the medium around it [3, 36]. Detection is directly related to the received signal-to-interference ratio  $SIR_i$ , which in turn is related to the attenuated transmit level [4, 36]. The transmit energy needs to be maximized to produce a higher probability that the sonar signal will be detected in noise limited conditions. The overall transmit energy can be related to this maximum transmit level through energy efficiency ( $E_{eff}$ ). Energy efficiency is the transmit energy of a real waveform ( $E_t$ ) compared to the maximum transmit energy

$$E_{max} = \int_0^T [f_{max}]^2 dt, \quad (2.44)$$

where  $f_{max}$  is the peak amplitude of the real transmit waveform. Therefore, energy efficient is

$$E_{eff} = \frac{E_t}{P_{peak}T} = \frac{E_t}{E_{max}}, \quad (2.45)$$

where  $P_{peak}$  is the peak transmitted power [30]. Energy efficiency is maximized in the case of a single real sinusoidal signal normalized to  $\sqrt{e_o}$ , where

$$E_{eff} = \frac{E_t}{E_{max}} = \frac{e_o}{e_o} = 1. \quad (2.46)$$

When transmit energy is maximized, the probability of detection for a fixed probability of false alarm is also maximized under noise limited conditions, as seen in (2.32). However, the total transmit energy is not always maximized, when multiple sonar waveforms are simultaneously in a peak power limited system. This can be caused by amplitude modulation, and is discussed in section 3.1. Therefore, another motivational goal behind sub-band modulation is to avoid amplitude modulation. In summary, this motivation conveys the need to investigate a process, that permits the time simultaneous transmission of multiple sonar signals, while avoiding amplitude modulation.

## Chapter 3

### Modulation Theory

Modulating a carrier waveform with several active sonar waveforms is one way to transmit multiple waveforms simultaneously. This has been done in radio broadcasting for many years. Both amplitude and angle modulation theory are discussed and the sub-band modulation concept is defined and analyzed. This is followed by an in-depth analysis of sub-band modulation. Finally, the demodulation of sub-band modulated signals is thoroughly examined.

#### 3.1 Overview of Amplitude Modulation

Linear combination is one way to simultaneously transmit multiple sonar waveforms without sacrificing the transmit time of each individual waveforms. This is done by selecting waveforms, that are sufficiently spectrally separated to permit their recovery by filtering. The linear combination of multiple, analytic sonar waveforms is

$$\begin{aligned} f(t) &= \sqrt{e_o} A_c \sum_{m=1}^N \tilde{f}_m(t) \exp(j\omega'_m t) \quad t \in (0, T) \\ &= \sqrt{e_o} A_c \sum_{m=1}^N \left[ a_m(t) \exp(j\psi_m(t)) \right] \exp(j\omega'_m t) \quad t \in (0, T), \end{aligned} \quad (3.1)$$

where  $\tilde{f}_m(t)$  are the complex envelopes of the sonar waveforms, and  $N$  is the total number of sonar waveforms. The transmit waveform energy is normalized by

$$A_c = \frac{1}{\sqrt{\frac{1}{2} \int_0^T \left( \sum_{m=1}^N a_m(t) \right)^2 dt}}, \quad (3.2)$$

since the real waveform will be transmitted, and the transmit energy is limited to  $e_o$  [30].  $A_c$  depends on the modulating signals and modulation type, so it will be redefined for each form of amplitude modulation discussed in this section. (3.1) can be rewritten

as

$$f(t) = \sqrt{e_o} A_c \exp(j\omega_0 t) \left[ \sum_{m=1}^N \tilde{f}_m(t) \exp\left(j \left[ \omega'_m - \omega_0 \right] t\right) \right] \quad (3.3)$$

by separating the carrier waveform. (3.3) reveals, that the linear combination of sonar waveforms results in a carrier waveform with a modulating amplitude. Although one of the motivations behind sub-band modulation is to avoid amplitude modulation, it is presented here to illustrate why it is undesirable.

If the modulation is a real function instead of analytic, then (3.3) becomes amplitude modulation (AM). Amplitude modulation is the linear combination of multiple waveforms as the amplitude component of a carrier, and has the form

$$f(t) = \sqrt{e_o} A_c \exp(j\omega_0 t) \left[ \sum_{m=1}^{N/2} a_m(t) \cos(\omega_m t + \psi_m(t)) \right], \quad (3.4)$$

where  $\omega_m = \omega'_m - \omega_0$ ,  $\omega'_m > \omega_0$  and  $N$  is the total number of sonar waveforms in the modulating spectrum, which is an even number for AM suppressed carrier [19, 30, 41]. Since the maximum transmit energy is limited to  $e_o$  (section 2.3),  $A_c$  from (3.2) becomes

$$A_c = \frac{1}{\sqrt{\frac{1}{2} \int_0^T \left[ \sum_{m=1}^{N/2} a_m(t) \right]^2 dt}}. \quad (3.5)$$

An AM waveform is typically designed using (3.4) and not (3.1), so the  $\omega_m$  are the center frequencies of the sonar waveforms and  $\omega_m < \omega_0$ . The carrier waveform is suppressed in this case (commonly known as AM suppressed carrier), and the time series and frequency spectrum of the amplitude modulation of a suppressed carrier by two sinewaves is shown in figures 3.1a and b<sup>1</sup>.

---

<sup>1</sup>The non-symmetries in any of the frequency spectrum plots in this thesis are due to finite sampling.

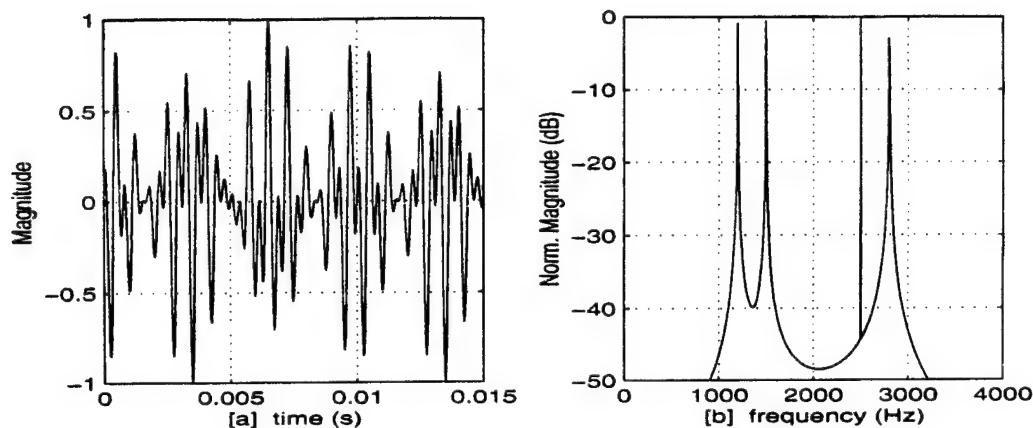


Fig. 3.1. Example AM Suppressed Carrier of Two Sinewaves (Center Frequencies of 500Hz, 800Hz) with a Carrier Frequency of 2kHz: [a] Time Series and [b] Frequency Spectrum

Assuming that  $f_m(t)$  are real and sinusoidal, the total transmit energy (2.43) of a real AM waveform with a suppressed carrier (3.4) is

$$E_t = \frac{e_o A^2}{2} \int_0^T \left[ \sum_{m=1}^{N/2} a_m(t) \cos(\omega_m t + \psi_m(t)) \right]^2 dt. \quad (3.6)$$

The peak amplitude of the real transmit waveform is

$$f_{max} = \text{maximum } f(t) = \sqrt{e_o} A_c \left[ \sum_{m=1}^{N/2} a_m(t) \right] \geq f(t), \quad (3.7)$$

producing a maximum transmit energy (2.44) of

$$E_{max} = \frac{e_o A^2}{2} \int_0^T \left[ \sum_{m=1}^{N/2} a_m(t) \right]^2 dt = e_o. \quad (3.8)$$

(3.6), (3.5) and (3.8) are combined to yield the energy efficiency of an AM suppressed carrier waveform,

$$\begin{aligned}
 E_{eff} &= \frac{E_t}{E_{max}} \\
 &= \frac{\frac{e_o}{2} \int_0^T \left[ \sum_{m=1}^{N/2} a_m(t) \cos(\omega_m t + \psi_m(t)) \right]^2 dt}{\frac{1}{2} \int_0^T \left[ \sum_{m=1}^{N/2} a_m(t) \right]^2 dt} \bigg/ e_o \\
 &= \frac{\int_0^T \left[ \sum_{m=1}^{N/2} a_m(t) \cos(\omega_m t + \psi_m(t)) \right]^2 dt}{\int_0^T \left[ \sum_{m=1}^{N/2} a_m(t) \right]^2 dt}. \tag{3.9}
 \end{aligned}$$

Since cosine functions are limited to a range of (-1,1), the numerator of (3.9) is always less than or equal to the denominator. Therefore,  $E_{eff} \leq 1$  for AM suppressed carrier waveforms. This illustrates that the transmit energy of AM suppressed carrier waveforms depend on the modulating waveforms, and their overall transmit energy is not maximized.

Another form of amplitude modulation occurs, when the carrier is not suppressed. The AM waveform with a carrier is

$$f(t) = \sqrt{e_o} A_c \exp(j\omega_o t) \left[ 1 + \sum_{m=1}^{(N-1)/2} a_m(t) \cos(\omega_m t + \psi_m(t)) \right], \tag{3.10}$$

where the carrier appears in the spectrum (see figure 3.2b), and  $N$  is odd [2, 9, 13, 19, 41].  $A_c$  is redefined for an AM waveform with carrier as

$$A_c = \frac{1}{\sqrt{\frac{1}{2} \int_0^T \left[ 1 + \sum_{m=1}^{(N-1)/2} a_m(t) \right]^2 dt}}. \tag{3.11}$$

The total transmit energy of a real AM waveform with a carrier (3.10) is

$$E_t = \frac{e_o A_c^2}{2} \int_0^T \left[ 1 + \sum_{m=1}^{(N-1)/2} a_m(t) \cos(\omega_m t + \psi_m(t)) \right]^2 dt. \tag{3.12}$$

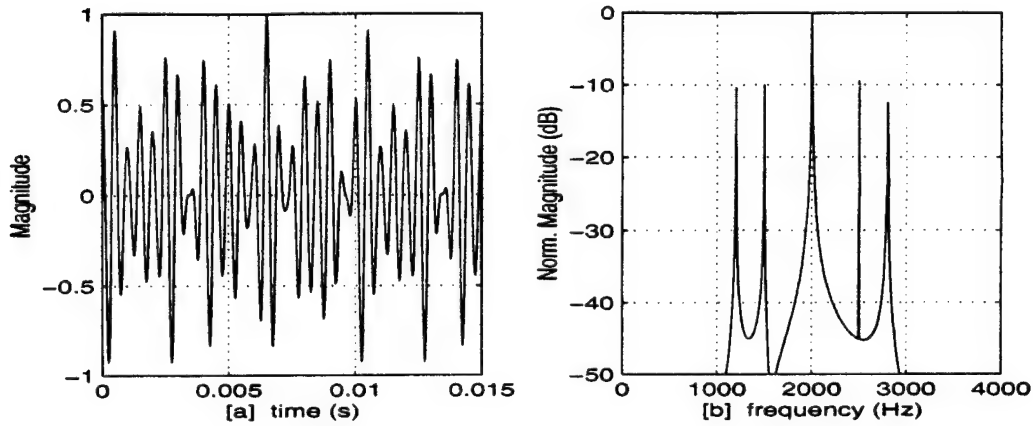


Fig. 3.2. Example AM with Carrier of Two Sinewaves (Center Frequencies of 500Hz, 800Hz) with a Carrier Frequency of 2kHz: [a] Time Series and [b] Frequency Spectrum

By taking into account the peak amplitude of the real transmit waveform of the AM waveform with carrier

$$f_{max} = \sqrt{e_o} A_c \left[ 1 + \sum_{m=1}^{(N-1)/2} a_m(t) \right] \geq f(t), \quad (3.13)$$

which yields a maximum transmit energy of

$$E_{max} = \frac{e_o A_c^2}{2} \int_0^T \left[ 1 + \sum_{m=1}^{(N-1)/2} a_m(t) \right]^2 dt = e_o, \quad (3.14)$$

the energy efficiency of an AM waveform with a carrier can be calculated.

$$\begin{aligned} E_{eff} &= \frac{\frac{e_o}{2} \int_0^T \left[ 1 + \sum_{m=1}^{(N-1)/2} a_m(t) \cos(\omega_m t + \psi_m(t)) \right]^2 dt}{\frac{1}{2} \int_0^T \left[ 1 + \sum_{m=1}^{(N-1)/2} a_m(t) \right]^2 dt} \bigg/ e_o \\ &= \frac{\int_0^T \left[ 1 + \sum_{m=1}^{(N-1)/2} a_m(t) \cos(\omega_m t + \psi_m(t)) \right]^2 dt}{\int_0^T \left[ 1 + \sum_{m=1}^{(N-1)/2} a_m(t) \right]^2 dt}, \end{aligned} \quad (3.15)$$



where  $E_{eff} \leq 1$  under the same conditions that applied to the AM suppressed carrier case. The influence of the modulating waveforms is still present, and the overall transmit energy is not maximized. Therefore, the varying amplitude of an AM waveform is disadvantageous in a peak power limited system.

### 3.2 Overview of Angle Modulation and Sub-band Modulation

Multiple sonar waveforms can also be transmitted simultaneously using angle modulation. Wherein, the amplitude of the carrier waveform is held constant, and multiple waveforms are combined as the phase component of the carrier [2, 9, 41]. The use of angle modulation in active sonar was first suggested by L. H. Sibul [30]. Angle modulation may be either phase modulation (PM) or frequency modulation (FM). The phase of the carrier waveform is varied linearly with the message waveforms with PM, where

$$\Re\{f(t)\} = \sqrt{e_o} A_c \cos \left( \omega_0 t + k_p \sum_{m=1}^N f_m(t) \right). \quad (3.16)$$

$k_p$  is the deviation constant of the phase modulation and will be further explained later on in this section [2, 27, 9, 17, 28, 34, 41].  $A_c$  is defined as  $A_c = 1/\sqrt{T}$ , because the amplitude of an angle modulated waveform remains constant [9], and the the maximum transmit energy is limited to  $e_o$ . Middleton [17] states, that the conditions  $\omega_m k_p \ll \omega_0$  and  $\omega_m \ll \omega_0$  must be imposed, if (3.16) is to be characterized as modulation and not waveform mixing. An example of the phase modulation of a carrier with two sinewaves is shown in figures 3.3a and b.

FM is the linear variation of the time derivative of the phase of the carrier, as shown by

$$\Re\{f(t)\} = \sqrt{e_o} A_c \cos \left( \omega_0 t + k_f \int_{t_0}^t \left[ \sum_{m=1}^N f_m(u) \right] du \right), \quad (3.17)$$

where  $A_c$  remains defined as  $A_c = 1/\sqrt{T}$ ,  $k_f$  is the deviation constant of the frequency modulation [9, 28, 17, 19, 30, 41], and the modulation conditions for FM are  $k_f \ll \omega_0$  and  $\omega_m \ll \omega_0$  [17]. An example of two sinewaves frequency modulating a carrier is shown in figures 3.4a and b.

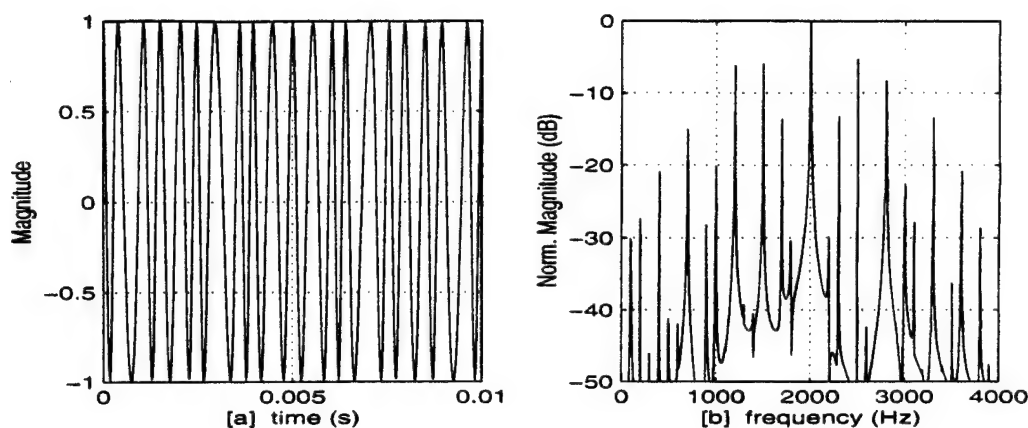


Fig. 3.3. Example PM of Two Sinewaves (Center Frequencies of 500Hz, 800Hz) with a Carrier Frequency of 2kHz and a Modulation Index of 1.5: [a] Time Series and [b] Frequency Spectrum

The transmit energy (2.43) for real waveforms with both real phase and frequency modulation is

$$E_t = \int_0^T \left( \sqrt{e_o} A_c \cos(\omega_0 t + \psi(t)) \right)^2 dt. \quad (3.18)$$

Since the amplitude of the carrier waveform is not changed by the frequency and phase modulating waveforms, the transmit energy becomes  $E_t = e_o$  [9, 41]. Certain extenuating circumstances do exist, which keep  $E_t$  from being maximized. These circumstances become more obvious, when (3.18) is expressed as a series of Bessel functions. This will be discussed thoroughly in section 3.2.1. However, they can be typically avoided by limiting the size of  $k_p$ , so the power of an angle modulated waveform is independent of the message waveforms [41]. Angle modulation transfers the signal energy from the carrier to the sidebands, so the average energy of the modulating waveform is the same as the unmodulated carrier waveform [9, 17]. Therefore, it is no surprise, that energy efficiency for angle modulation is  $E_{eff} = e_o/e_o = 1$ , and the transmit energy is maximized.

The difference between the transmit energy in an amplitude modulated waveform and the transmit energy in an angle modulated waveform can be quantified by evaluating the contribution of each individual waveform to the signal energy. AM splits the amplitude of the carrier waveform amongst the waveforms modulating it. When equal

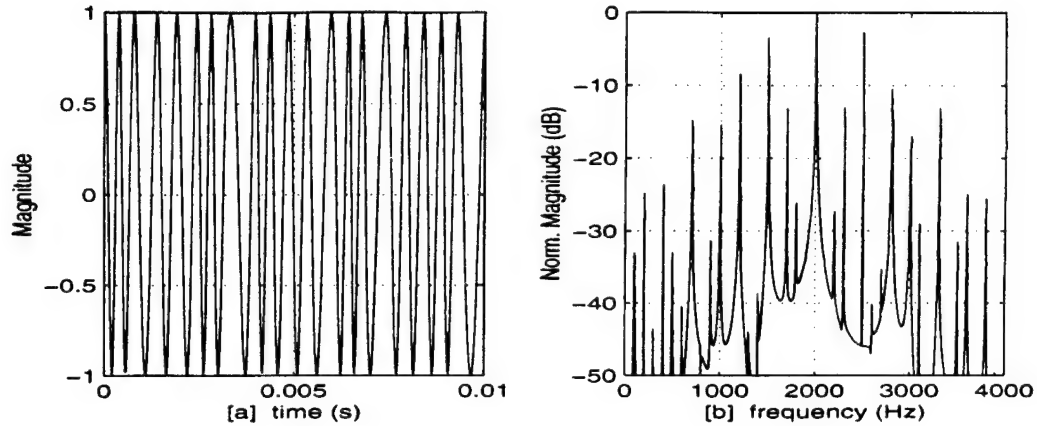


Fig. 3.4. Example FM of Two Sinewaves (Center Frequencies of 500Hz, 800Hz) with a Carrier Frequency of 2kHz and a Modulation Index of 0.15: [a] Time Series and [b] Frequency Spectrum

amplitude signals are used, the amplitude for each waveform is  $\frac{1}{N}$ . Therefore, the signal energy for each of the individual waveforms is reduced by a factor of  $\frac{1}{N^2}$ . This differs from angle modulation, where the signal energy instead of the amplitude is split between the waveforms modulating the carrier. Assuming that all of the signal energy is split between the waveforms modulating the carrier and none is lost, then energy in each waveform becomes  $\frac{1}{N}E_t$ , instead of  $\frac{1}{N^2}E_t$ . Therefore, the energy splitting of angle modulation provides an increase in individual waveform energy over the amplitude splitting of amplitude modulation.

Angle modulation allows for the simultaneous transmission of multiple sonar waveforms over a maximized time interval while avoiding amplitude modulation. However, this research focuses on phase modulation, rather than frequency modulation, for several reasons. Most sonar waveforms are combinations of sinewaves, in one form or another. Whether they are simple CWs or a combination of CW pulses used to represent a LFM, sinusoidal waveforms make up the majority of the waveforms used in this study. The integration of a sinewave is another sinewave phase shifted, so in the context of this research, frequency modulation and phase modulation are essentially the same process. However, frequency modulation requires more computational processing. The processing is simplified through the use of PM, because it requires a less elaborate implementation in Matlab. Therefore, the definition of sub-band modulation for the purpose of this

thesis is the phase modulation of a carrier by multiple waveforms, as applied to active sonar.

### 3.2.1 Characteristics of Sub-band Modulation

The two major parameters of phase modulation as described in (3.16) are the carrier frequency  $\omega_0$  and the deviation constant  $k_p$ . The carrier frequency is the center frequency of the sub-band modulated waveform, and the modulating waveforms appear in the frequency spectrum as the lower and upper sidebands around the carrier frequency, as seen in figure 3.5 where  $\eta_0 = \frac{\omega_0}{2\pi} = 2\text{kHz}$ .

The deviation constant is the maximum value of the phase deviation of the modulated carrier waveform. When the message waveforms are sinusoidal, it is known as the modulation index [41], and in this thesis the terms will be used interchangeably. The deviation constant controls the bandwidth of the modulation and the magnitude of the sidebands, and therefore controls the prominence of the sub-band waveforms in the modulating spectrum. The effects of  $k_p$  are apparent when (3.16) is expressed as the sum of Bessel functions. First, (3.16) is rewritten as

$$\Re\{f(t)\} = \sqrt{e_o} A_c \Re\left\{\exp(j\omega_0 t) \prod_{m=1}^N \exp(jk_p f_m(t))\right\}$$

Assuming that the sonar waveforms  $f_n(t)$  are sinusoidal, the Bessel function expansion is

$$\exp[jk_p \sin(\omega t)] = \sum_{\hat{m}=-\infty}^{\infty} J_{\hat{m}}(k_p) \exp(j\hat{m}\omega t), \quad (3.19)$$

and (3.16) becomes

$$\begin{aligned} \Re\{f(t)\} &= \sqrt{e_o} A_c \Re\left\{\exp(j\omega_0 t) \prod_{m=1}^N \left[\sum_{\hat{m}=-\infty}^{\infty} J_{\hat{m}}(k_p) \exp(j\hat{m}\omega_m t)\right]\right\} \\ &= \sqrt{e_o} A_c \sum_{\hat{m}_1=-\infty}^{\infty} \cdots \sum_{\hat{m}_N=-\infty}^{\infty} J_{\hat{m}_1}(k_p) \cdots J_{\hat{m}_N}(k_p) \cos\left([\omega_0 + \hat{m}_1\omega_1 + \cdots + \hat{m}_N\omega_N]t\right) \end{aligned} \quad (3.20)$$

[2, 9, 17, 19, 28, 41]. The sub-band modulating waveforms lie at the carrier frequency plus and minus integer multiples of their center frequencies with magnitudes determined by the value of the Bessel function at the deviation constant. The form of the sub-band

modulation is shown by the following example, where two sinusoidal message waveforms are sub-band modulating a carrier. (3.20) is rewritten as

$$\Re\{f(t)\} = \sqrt{e_o} A_c \sum_{\hat{m}_1=-\infty}^{\infty} \sum_{\hat{m}_2=-\infty}^{\infty} J_{\hat{m}_1}(k_p) J_{\hat{m}_2}(k_p) \cos \left( [\omega_0 + \hat{m}_1 \omega_1 + \hat{m}_2 \omega_2] t \right), \quad (3.21)$$

and is displayed in figure 3.5.

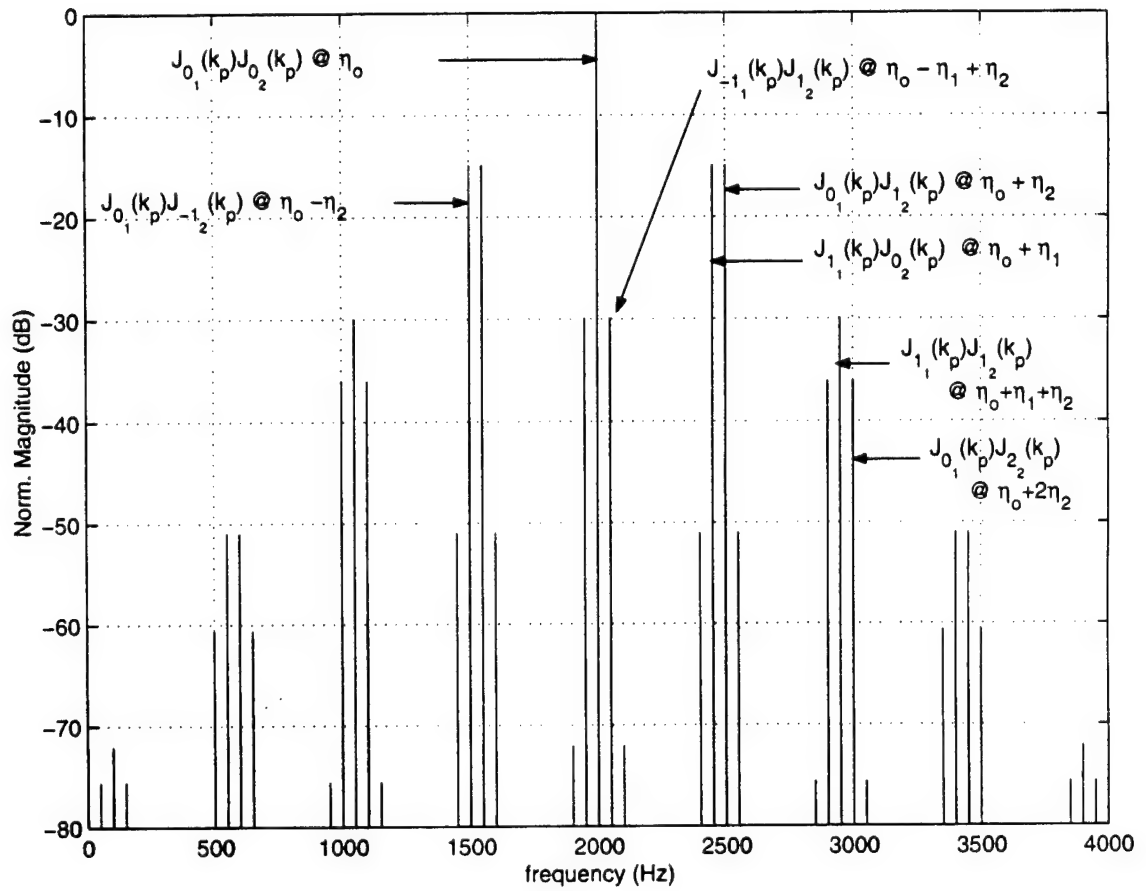


Fig. 3.5. Sub-band Modulation of Two Sinewaves ( $\eta_1 = 450\text{Hz}$ ,  $\eta_2 = 500\text{Hz}$ ) with  $\eta_0 = 2\text{kHz}$  and  $k_p = 0.7$  (Frequency Spectrum)

Ziemer and Tranter [41] point out, that angle modulation results in an infinite number of sidebands, which yields an essentially infinite bandwidth. However, a fixed  $k_p$  yields  $\lim_{\hat{m} \rightarrow \infty} J_{\hat{m}}(k_p) = 0$ , so only the sidebands containing significant power are applicable.  $\kappa$  represents the significant number of sidebands on each side of the carrier, where  $J_{\hat{m}}(k_p) \neq 0$  for  $\hat{m} \in (-\kappa, \kappa)$ . Initial investigations into phase modulation with Matlab revealed, that even  $\kappa$  sidebands  $\sim 40\text{dB}$  down from the carrier are significant and aid in the proper demodulation of the sonar signals.  $\kappa$  can be related to the bandwidth of the sub-band modulation by

$$B \cong 2\kappa\omega_{max}, \quad (3.22)$$

where  $\omega_{max}$  is the highest frequency of the modulating waveforms, and  $B$  is the bandwidth of the modulation [41]. Carson's Rule,

$$B \cong 2(k_p + 1)\omega_{max} \quad (3.23)$$

which describes the bandwidth of angle modulation as a function of the deviation constant [4, 41], relates  $\kappa$  and  $k_p$  by

$$\kappa \cong k_p + 1, \quad (3.24)$$

illustrating that the bandwidth of the sub-band modulation broadens with increasing values of  $k_p$ .

This can be problematic in sub-band modulation, because the transmit energy can be effected by large increases in modulation index and bandwidth. The overall transmit energy of a sub-band modulating waveform (3.18) can be restated using (3.20) to better

illustrate this effect;

$$\begin{aligned}
 E_t &= \int_0^T \left| \sqrt{e_o} A_c \prod_{m=1}^N \left[ \sum_{\hat{m}=-\kappa}^{\kappa} J_{\hat{m}_m}(k_p) \cos(\omega_0 t + \hat{m} \omega_m t) \right] \right|^2 dt \\
 &\vdots \\
 &= e_o \prod_{m=1}^N \left[ \sum_{\hat{m}=-\kappa}^{\kappa} J_{\hat{m}_m}^2(k_p) \right] \\
 &= e_o \prod_{m=1}^N \left[ \underbrace{J_{0_m}^2(k_p) + 2 \sum_{\hat{m}=1}^{k_p+1} J_{\hat{m}_m}^2(k_p)}_{\dagger} \right]. \tag{3.25}
 \end{aligned}$$

The second term of  $\dagger$  (3.25) is negligible for small values of  $k_p$  ( $k_p < \frac{\pi}{2}$  [29]), and  $J_{0_m}^2(k_p) \approx 1$  [9, 41]. The second term becomes significant as  $k_p$  becomes larger, which also results in a decrease in the magnitude of the first term [17, 29]. Schwartz [29] defines a large modulation index as  $k_p > \frac{\pi}{2}$ .  $\dagger$  can still approximate unity in this case. However, when the modulation index becomes too large, the modulating bandwidth becomes so wide, that some of the significant terms of (3.25) are located at frequencies much higher than the carrier  $\omega_0$ . This can result in  $\dagger \not\approx 1$ , which equates to amplitude modulation. Computational complexity and sampling frequency limitations may require some of these higher frequency terms to be neglected, which can also result in amplitude modulation [13].

Therefore, the modulating waveforms begin to affect the overall transmit energy as  $k_p$  increases, as shown by the following example. The sub-band modulation of a carrier with two sinewaves (3.21) is illustrated, and the time series and spectra of the sub-band waveform with increasing  $k_p$  are shown in figures 3.6a-f. Small values of  $k_p$  ( $k_p = 1.2$ ) result in a narrow bandwidth of essentially only the first sideband ( $B \approx 2.2\text{kHz}$ ), as seen in figures 3.6a, b. Here, the spectrum of the sub-band modulation appears somewhat similar to an AM spectrum, because most of the waveform information is contained within the major sidebands. However, the sidebands quickly broaden and begin to resemble overlapping Bessel functions as  $k_p$  increases (figures 3.6c, d). The waveform information is no longer contained within the first sidebands, when larger values of  $k_p$  are used ( $k_p = 2$ ,  $B \approx 3\text{kHz}$ ). Therefore, sub-band modulation can be used to create a waveform with a spread spectrum. Eventually, the bandwidth of the

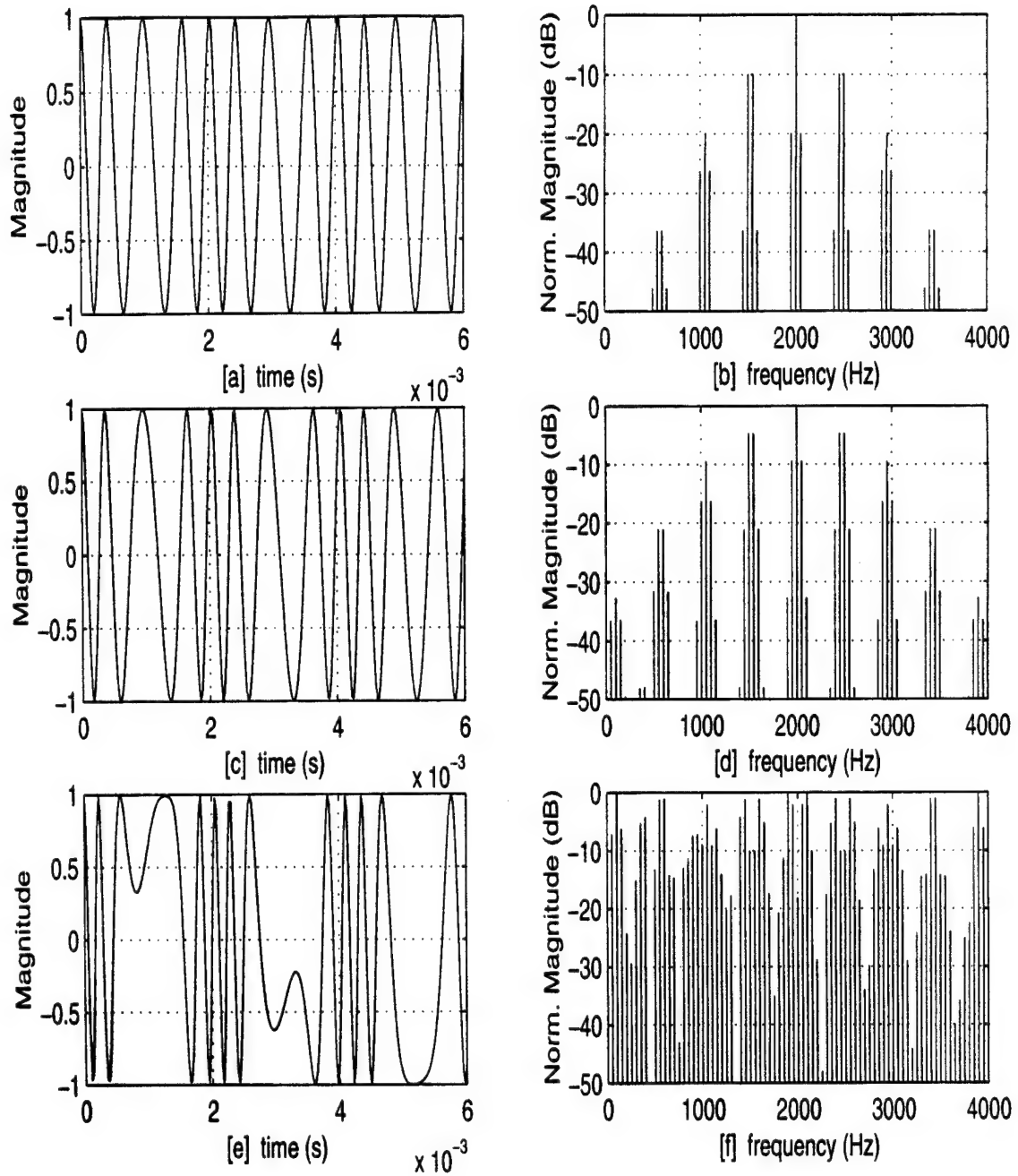


Fig. 3.6. Sub-band Modulation of Two CWs ( $\eta_1 = 450\text{Hz}$ ,  $\eta_2 = 500\text{Hz}$ ) with a Carrier Frequency of 2kHz and Increasing Values for  $k_p$ , Where the Left Column are the Time Series and the Right Column are the Frequency Spectra : [a]  $k_p = 1.2$  (small), [b]  $k_p = 1.2$  (small), [c]  $k_p = 2$  (medium), [d]  $k_p = 2$  (medium), [e]  $k_p = 5.5$  (large), and [f]  $k_p = 5.5$  (large)



sub-band modulation will fill the spectrum as  $k_p$  increases further ( $k_p = 5.5$ ,  $B \approx 6.5\text{kHz}$ ), as seen in figures 3.6e and f. This can even result in a modulating amplitude in some extreme cases, as seen in figure 3.6e. When  $k_p$  is large, an angle modulating waveform can be passed through a limiter, which removes any amplitude modulation in the signal [17]. However, a limiter is not needed, when  $k_p$  is kept relatively small. For the purposes of sub-band modulation, the modulation index is also kept relatively small, so the modulation bandwidth can be limited to the desired frequency range. A further discussion of spectrum considerations for sub-band modulation is presented in section 4.1.

### 3.3 Demodulation

The received echo is demodulated to recover the sub-band modulating signals, before the individual waveform components are processed. The demodulation process is first analyzed without the inclusion of noise, and then followed by an investigation of the sub-band demodulation process in the presence of noise. In the same vein, the demodulation process will first be introduced without the inclusion of time delay and Doppler, and then further analyzed with the effects of time compression and delay taken into account. This incremental breakdown and examination allows for all of the aspects of the received signal affecting the demodulation process to be individually analyzed.

#### 3.3.1 Demodulation without Interference

The point scatterer echo signal component of the received data (2.9) is

$$s(t) = \sqrt{e_o} S_s \cos \left( \omega_0 t + k_p \sum_{m=1}^N f_m(t) \right) \quad (3.26)$$

assuming  $\beta = 1$  ( or  $\phi = 0$  ) and  $\tau = 0$ . A demodulation process is implemented to extract the modulating sonar signals  $\left( \psi(t) = k_p \sum_{m=1}^N f_m(t) \right)$  from the carrier signal, and an ideal discriminator was implemented for this thesis. According to Van Trees [34], "An ideal discriminator is simply a device whose voltage output is proportional to the instantaneous frequency of its input." FM and PM demodulation using a discriminator (or discrimination) is the separation of the modulating signals from the carrier. Therefore,

the output of a sub-band modulation discriminator is

$$s_d(t) = K_d \psi(t) = K_d k_p \sum_{m=1}^N f_m(t), \quad (3.27)$$

where  $K_d$  is a discriminator constant [2, 41].

The ideal discriminator used in this study is based upon the demodulator implemented in the Matlab Signal Processing Toolbox [14]. The use of this demodulator is discussed in section 4.3, but the theory behind it is presented here. First, the received echo signal is made analytic with a Hilbert transform, and yields:

$$\begin{aligned} s_1(t) &= s(t) + js_H(t) \\ &= \sqrt{e_o} S_s a(t) \cos \left( \omega_0 t + k_p \sum_{m=1}^N f_m(t) \right) + j \sqrt{e_o} S_s a(t) \sin \left( \omega_0 t + k_p \sum_{m=1}^N f_m(t) \right) \\ &= \sqrt{e_o} S_s a(t) \cos (\omega_0 t + \psi(t)) + j \sqrt{e_o} S_s a(t) \sin (\omega_0 t + \psi(t)) \\ &= \sqrt{e_o} S_s a(t) \exp (j \omega_0 t + j \psi(t)) \\ &= \sqrt{e_o} S_s \tilde{f}(t) \exp (j \omega_0 t) \end{aligned} \quad (3.28)$$

The carrier is then extracted by multiplying  $s_1(t)$  by the complex conjugate of the carrier signal,

$$\begin{aligned} s_2(t) &= s_1(t) \exp (-j \omega_0 t) \\ &= \sqrt{e_o} S_s \tilde{f}(t) \exp (j \omega_0 t) \exp (-j \omega_0 t) \\ &= \sqrt{e_o} S_s \tilde{f}(t) \end{aligned} \quad (3.29)$$

and it becomes a baseband signal.

Next, the sonar signals are retrieved from  $s_2(t)$  by taking the imaginary part of it's natural log:

$$\begin{aligned}
 s_3(t) &= \Im \left\{ \ln [s_2(t)] \right\} \\
 &= \Im \left\{ \ln \left( \sqrt{e_o} [S_s] [\tilde{f}_t(t)] \right) \right\} \\
 &= \Im \left\{ \ln \left( \sqrt{e_o} [S_s] \exp(j\theta) [a(t) \exp(j\psi(t))] \right) \right\} \\
 &= \Im \left\{ \ln \left( \sqrt{e_o} |S_s| a(t) \right) + \ln (\exp [j(\psi(t) + \theta)]) \right\} \\
 &= \psi(t) + \theta \\
 &= k_p \sum_{m=1}^N f_m(t) + \theta.
 \end{aligned} \tag{3.30}$$

The derivation of (3.30) shows that the effects of the amplitude modulation  $a(t)$  are discarded by the discriminator. The benefits of this are discussed in section 3.3.2. (3.30) retains the uniform phase component of the point scatterer, but it is turned into a constant by the discrimination process, and can be easily removed by filtering. The highpass filtered version of (3.30) is represented by  $s_{3f}(t)$ . Finally, the signal is multiplied by a discriminator constant  $\left( K_d = \frac{1}{k_p} \right)$ , and the discriminator yields the demodulated sonar signals:

$$\begin{aligned}
 s_d(t) &= \frac{1}{k_p} s_{3f}(t) \\
 &= \sum_{m=1}^N f_m(t),
 \end{aligned}$$

which is the same form as (3.27). The waveforms were intentionally designed to be spectrally separable using bandpass filtering at the output of the ideal discriminator. A further discussion of the waveform design criteria is presented in section 4.2.

When  $\beta \neq 1$  and  $\tau \neq 0$ , the analytic form of the wideband Doppler model of the echo signal component of the data is

$$s_1(t) = \sqrt{\beta e_o} S_s \tilde{f}(\beta[t - \tau]) \exp(j\omega_0[t - \tau]) \exp(j2\pi\phi t). \tag{3.31}$$

First, the carrier is extracted from (3.31) by multiplying by the complex conjugate of the carrier signal, as was done in (3.29).

$$\begin{aligned}
 s_2(t) &= [s_1(t)] \exp(-j\omega_0 t) \\
 &= [\sqrt{\beta e_o} S_s \tilde{f}(\beta[t - \tau]) \exp(j\omega_0[t - \tau]) \exp(j2\pi\phi t)] \exp(-j\omega_0 t) \\
 &= \sqrt{\beta e_o} [S_s] [\tilde{f}(\beta[t - \tau])] \exp(-j\omega_0 \tau) \underbrace{\exp(j2\pi\phi t)}_{\star} \quad (3.32)
 \end{aligned}$$

(3.32) illustrates that this process does not entirely baseband the modulating signals when  $\beta \neq 1$ , because the Doppler component of the carrier ( $\star$ ) is not removed. This mismatch between the transmit carrier frequency used for demodulation and the received carrier frequency effected by  $\star$  degrades the discriminator's performance.  $\star$  can be removed from the received signal by demodulating with the complex conjugate of the Doppler shifted carrier. However, this assumes that the Doppler shifted carrier frequency is known. This is not a practical assumption for a demodulator in a sonar signal processing system, since the Doppler shift should be estimated from the received signal and is not known prior to signal reception. Demodulation with a mismatched and a matched carrier are investigated in the experiment and analysis section of this thesis (section 4.4 and 5.1). The practical advantages and disadvantages of carrier frequency matching in demodulation or not will be further discussed in these sections. However, it will be shown, that although a carrier mismatch in the demodulation process with an ideal discriminator does result in decreased demodulator performance, it does not severely degrade the performance. Furthermore, the resulting performance remains constant even as the difference between the demodulation frequency and the received carrier frequency increases. Therefore, the ideal discriminator is still a reasonably effective sub-band demodulator, even when the carrier frequency is mismatched. Since the ideal discrimination process is identical except for the carrier frequencies in the cases of matched and mismatched carriers, the demodulation process will be described here taking both processes into consideration. Following this discussion, a method of coupling the demodulation process with hypothesis testing in order to implement frequency matching is presented. The further comparison between the different demodulation processes is left to the analysis of this thesis (section 5.1).

Equation 3.32 with the mismatched carrier is expanded before the demodulation process continues, so  $s_2(t)$  becomes

$$\begin{aligned}
 s_2(t) &= \sqrt{\beta e_o} [S_s] [\tilde{f}(\beta[t - \tau])] \exp(-j\omega_o \tau) \exp(j2\pi\phi t) \\
 &= \sqrt{\beta e_o} [|S_s| \exp(j\theta)] [a(\beta[t - \tau]) \exp(j[\psi(\beta[t - \tau])])] \exp(-j\omega_o \tau) \exp(j2\pi\phi t) \\
 &= \sqrt{\beta e_o} |S_s| a(\beta[t - \tau]) \exp(j[\psi(\beta[t - \tau]) + \theta - \omega_o \tau + 2\pi\phi t]). \quad (3.33)
 \end{aligned}$$

The imaginary part of the natural logarithm of  $s_2(t)$  is then separated from the rest of the signal, which yields the modulating signals, as shown by (3.30).

$$\begin{aligned}
 s_3(t) &= \Im \{ \ln [s_2(t)] \} \\
 &= \Im \{ \ln [\sqrt{\beta e_o} |S_s| a(\beta[t - \tau])] + \ln [\exp(j[\psi(\beta[t - \tau]) + \theta - \omega_o \tau + 2\pi\phi t])] \} \\
 &= \psi(\beta[t - \tau]) + \theta - \omega_o \tau + 2\pi\phi t \\
 &= k_p \sum_{m=1}^N f_m(\beta[t - \tau]) + \underbrace{\theta - \omega_o \tau + 2\pi\phi t}_* \quad (3.34)
 \end{aligned}$$

(3.34) contains the modulating signals, along with a linear term and two constants (\*) due to the time dilated and delayed carrier and the phase of the point scatterer.  $\theta$  and  $\omega_o \tau$  do not have a significant effect on the demodulated signal, and some of the effects of  $2\pi\phi t$  can be removed with a highpass filter. When the filter is applied to (3.34), it yields essentially the modulating signals<sup>2</sup>,

$$s_{3f}(t) \approx k_p \sum_{m=1}^N f_m(\beta[t - \tau]).$$

The modulation index is then removed from the signals to yield the output of the discriminator,

$$s_d(t) \approx \sum_{m=1}^N f_m(\beta[t - \tau]) \quad (3.35)$$

<sup>2</sup>If the carrier frequency happened to be precisely matched by the demodulator, the highpass filter would yield only the time delayed and dilated modulating signals without any degradation.

These signals can then be separated from each other using band-pass filters and made analytic for further processing. Since a broad bandwidth is one of the characteristics of sub-band modulation, the wideband Doppler model is assumed for the echo signal before demodulation. However, the narrowband assumption may be implemented in the further processing of some of the demodulated sonar signals, if they meet the criteria set in (2.14).

Before the sonar signals are processed according to the methods discussed in section 2.3, they need to be frequency translated. Although the signals have been demodulated to their premodulation frequencies, they have experienced time dilation at a frequency near the carrier frequency. This results in a Doppler shift that is much larger than if the signal had not been sub-band modulated at all. This frequency shift becomes evident by comparing only one of the sub-band modulated/demodulated sonar signals ( $s_{d1}(t) = s_d(t)|_{m=1}$ ) and the same signal transmitted without the use of sub-band modulation ( $s_{u1}(t)$ ).  $s_{u1}(t)$  has a center frequency of  $\omega_1$  and experiences a Doppler shift of

$$\phi_{u1} = \frac{2v_l \eta_1}{c}. \quad (3.36)$$

Although  $s_{d1}(t)$  has the same center frequency, it was phase modulating a carrier at  $\eta_o$ , where  $\eta_1 \ll \eta_o$ . Therefore, the Doppler frequency of  $s_{d1}(t)$  after demodulation is

$$\phi_{d1} \approx \frac{2v_l \eta_o}{c} = \frac{2 \left( v_l \frac{\eta_o}{\eta_1} \right) \eta_1}{c}, \quad (3.37)$$

even though the center frequency of the signal is  $\eta_1$ . This presents a problem, when processing  $s_{d1}(t)$  with a matched filter, because the Doppler frequency of the demodulated signal is no longer representative of the Doppler velocity. The estimated scatterer velocity is  $v_l \frac{\eta_o}{\eta_1}$  instead of  $v_l$ . Therefore, the demodulated and separated signals are shifted in frequency up to the carrier frequency to account for this processing anomaly. This is achieved by multiplying the signal by the carrier signal. This shift in frequency

is known as a heterodyne shift, and the demodulated signal becomes

$$\begin{aligned}
 s_{dh1}(t) &= [s_{d1}(t)] \exp(j\omega_0 t) \\
 &= \left[ \tilde{f}_1(\beta t) \exp(j\omega_1 t) \exp\left(j\frac{2\omega_0 v_l}{c} t\right) \right] \exp(j\omega_0 t) \\
 &= \tilde{f}_1(\beta t) \exp\left(j[\omega_1 + \omega_0] t\right) \exp\left(j\frac{2\omega_0 v_l}{c} t\right), \tag{3.38}
 \end{aligned}$$

where  $\omega_1 + \omega_0 \approx \omega_0$  because  $\omega_1 \ll \omega_0$ . Now, the Doppler shift in the demodulated signal is representative of the velocity of the scatterer. When processed with a matched filter bank of time dilated and delayed replicas centered around  $\omega_0 + \omega_1$ , the correct Doppler values are estimated<sup>3</sup>. It will be shown in section 4.2, that this frequency shift in the demodulation process is taken into consideration in the waveform design process.

Ironically, the ideal discriminator is not always the best choice for a demodulator. Prior knowledge of the carrier frequency and deviation constant are required for effective demodulation. Other demodulators can be more advantageous in certain situations, such as the phase-lock loop [30]. The phase-lock loop is a feedback demodulator, that implements a voltage-controlled oscillator to track the frequency deviations of the received signal. A voltage proportional to the frequency deviation between the received signal and a receiver generated sinewave are applied to the voltage-controlled oscillator. This shifts its frequency deviations to approximate the received signal [27, 12, 28, 34, 41]. The frequency deviation of the received signal is measured by implementing this feedback demodulator, and the phase-lock loop demodulates a received FM or PM signal without prior knowledge of the carrier frequency. The phase-lock loop also exhibits good noise performance, because the frequency deviations are constantly tracked [28]. However, phase-lock loop (and other demodulators) require a much more complex and rigorous implementation. Since the object of this research is to investigate the application of phase modulation in sonar, the investigation of more complex demodulation schemes will be left for future research.

One method of coupling the ideal discriminator with frequency matching as part of the hypothesis testing process is explored in this thesis. Instead of demodulating the received signal with only one carrier frequency and then matched filtering, the received

---

<sup>3</sup>Only  $f_1(\beta t)$  is used in (3.38) instead of  $f_1(\beta[t - \tau])$ , because the effects of time delay were removed to simplify processing. This was done using methods, that will be presented in section 4.3.

signal is demodulated with a time dilated carrier, whose time dilation correspond with the time dilation of the replica, against which it would be correlated in the matched filter process. Therefore, (3.32) becomes

$$\begin{aligned} s_2(t) &= [s_1(t)] \exp(-j\omega_0 t) \\ &\Rightarrow [s_1(t)] \exp(-j\omega_0 \hat{\beta} t) \\ &= [s_1(t)] \exp(-j\omega_0 t) \exp(-j2\pi \hat{\phi} t). \end{aligned} \quad (3.39)$$

This results in an array of demodulated signals, each demodulated with a different carrier  $\exp(-j\omega_0 \hat{\beta} t)$ . This means, that the demodulated signals before spectral separation (from (3.34)) become

$$s_3(t) = k_p \sum_{m=1}^N f_m(\beta[t - \tau]) + \theta - \omega_0 \tau + 2\pi \phi t - 2\pi \hat{\phi} t. \quad (3.40)$$

Therefore, the carrier time dilation is canceled out when  $\phi = \hat{\phi}$ , which occurs when the received carrier frequency is matched by the discriminator. This array of demodulated signals could then each be spectrally separated, and the resulting arrays of sub-band signals could then be matched filtered.

### 3.3.2 Demodulation in the Presence of Interference

The demodulation process becomes even more complex, when interference is also taken into consideration. The echo signal embedded in additive interference is represented by

$$\begin{aligned} r(t) &= s(t) + n(t) \\ &= \sqrt{e_o} |S_s| \cos[\omega_0 t + \theta + \psi(t)] + a_n(t) \cos[\omega_0 t + \psi_n(t)]. \end{aligned} \quad (3.41)$$

The interference term ( $n(t)$ ) can be either reverberation or noise, and the demodulation process is identical in the presence of either one.  $n(t)$  in this discussion is additive white Gaussian noise, where  $a_n(t)$  is the Rayleigh distributed noise envelope and  $\psi_n(t)$  is the uniformly distributed phase of the noise [41]. An effective way to illustrate the impact of noise on a sub-band modulating signal is to represent the received signal in vector notation. The vector of magnitude  $\sqrt{e_o} |S_s|$  rotates at the carrier frequency  $\omega_0$  in a noiseless environment, and that rotation is phase modulated by the message signals,



$\psi(t)$ .  $\theta$  is the phase shift imposed upon the echo signal by the scatterer (2.7), and it is set to zero here to simplify the vector addition. The addition of interference results in the vector addition between  $n(t)$  and the echo signal at the receiver. This yields a new vector amplitude and phase, as seen in figure 3.7.

The received signal(3.41) is rewritten with vector addition as

$$\begin{aligned}
 r(t) &= \sqrt{e_o} |S_s| \cos [\omega_0 t + \psi(t)] + a_n(t) \cos [\omega_0 t + \psi(t) + \psi_n(t) - \psi(t)] \\
 &= \sqrt{e_o} |S_s| \cos [\omega_0 t + \psi(t)] + a_n(t) \cos [\omega_0 t + \psi(t)] \cos [\psi_n(t) - \psi(t)] \\
 &\quad - a_n(t) \sin [\omega_0 t + \psi(t)] \sin [\psi_n(t) - \psi(t)] \\
 &= \left( \sqrt{e_o} |S_s| + a_n(t) \cos [\psi_n(t) - \psi(t)] \right) \cos [\omega_0 t + \psi(t)] \\
 &\quad - a_n(t) \sin [\psi_n(t) - \psi(t)] \sin [\omega_0 t + \psi(t)] \\
 &= R(t) \cos [\omega_0 t + \psi_R(t)]
 \end{aligned} \tag{3.42}$$

, where

$$R(t) = \sqrt{\left( \sqrt{e_o} |S_s| \right)^2 + 2 \sqrt{e_o} |S_s| a_n(t) \cos [\psi_n(t) - \psi(t)] + \left( a_n(t) \sin [\psi_n(t) - \psi(t)] \right)^2} \tag{3.43}$$

and

$$\psi_R(t) = \psi(t) + \tan^{-1} \left( \frac{a_n(t) \sin [\psi_n(t) - \psi(t)]}{\sqrt{e_o} |S_s| + a_n(t) \cos [\psi_n(t) - \psi(t)]} \right) \tag{3.44}$$

[2, 9, 27, 28, 41]. This notation illustrates the signal resulting from the addition of interference and the received echo, and this combined signal is the one, that gets demodulated.

The effectiveness of the sub-band demodulation process depends solely upon (3.44), since the discriminator disregards (3.43), as seen in section 3.3.1. If a high signal-to-interference ratio at the receiver ( $SIR_i$ ) is present ( $a_n(t) < \sqrt{e_o} |S_s|$ ), then the angular variations in the noise will result in minimal effects on the angle of the message signal, as seen in figure 3.7. Therefore, (3.44) can be rewritten as

$$\psi_R(t) = \psi(t) + \frac{a_n(t)}{\sqrt{e_o} |S_s|} \sin [\psi_n(t) - \psi(t)], \tag{3.45}$$

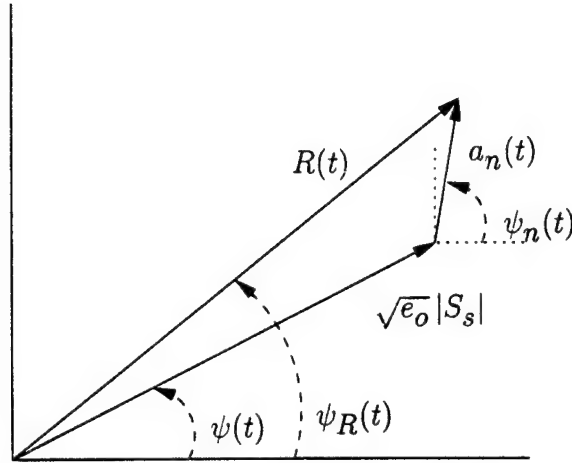


Fig. 3.7. Vector Addition of Echo Signal  $\left(s(t) = \sqrt{e_o} |S_s| \cos [\omega_0 t + \psi(t)]\right)$  and Noise  $\left(n(t) = a_n(t) \cos [\omega_0 t + \psi_n(t)]\right)$  at a Moment in Time (High  $SIR_i$ )

where  $\frac{a_n(t)}{\sqrt{e_o} |S_s|}$  is small compared to  $\psi(t)$ , and the phase of the received signal is dominated by the message signal [41].

However, the received signal dramatically changes as the signal-to-interference ratio becomes small. The noise signal becomes the dominant part of the received signal and the angular variations of the echo signal will have only a very small effect on its angle for a low signal-to-interference ratio at the receiver  $\left(a_n(t) > \sqrt{e_o} |S_s|\right)$ , as seen in figure 3.8 [9]. Therefore, (3.42) is rederived with the noise signal as the dominating signal, and (3.44) is rewritten as

$$\psi_R(t) = \psi_n(t) + \frac{\sqrt{e_o} |S_s|}{a_n(t)} \sin [\psi_n(t) - \psi(t)], \quad (3.46)$$

where  $\frac{\sqrt{e_o} |S_s|}{a_n(t)}$  is small compared to  $\psi_n(t)$  [41].

Although this seems like a drastic difference in demodulator performance, angle modulation (and sub-band modulation) offers significant demodulation improvement over amplitude modulation in a noisy environment. The magnitude of the received signal

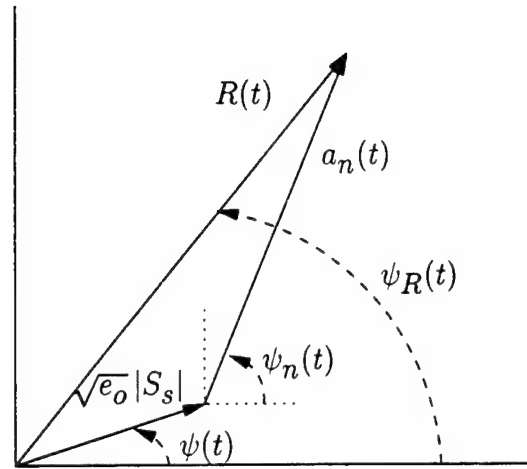


Fig. 3.8. Vector Addition of Echo Signal  $\left(s(t) = \sqrt{e_o} |S_s| \cos [\omega_0 t + \psi(t)]\right)$  and Noise  $\left(n(t) = a_n(t) \cos [\omega_0 t + \psi_n(t)]\right)$  at a Moment in Time (Low  $SIR_i$ )

varies linearly with the signal-to-interference ratio [9]. Figure 3.9 shows the linear increase in magnitude of the received signal as compared to the magnitude of only the echo signal. The amplitude difference increases in inverse proportion to  $SIR_i$ , which in turn adversely affects demodulation of an amplitude modulating echo signal. Although, this strongly effects the performance of AM, it is not detrimental to sub-band modulation, since the PM demodulation disregards the amplitude of the received signal. This is comparable to the reception of an AM radio signal, which does not fade out right away when the  $SIR_i$  gets small, but instead gets worse and worse as the  $SIR_i$  decreases. However, interference affects the phase of the received signal differently. Interference has very little effect on the phase of the received signal until the  $SIR_i$  gets small. When the  $SIR_i$  gets sufficiently small, the noise quickly dominates the phase component of the received signal, which is known as the threshold effect [29]. Figure 3.10 shows the drastic change in phase with decreasing  $SIR_i$  as compared to the phase of only the echo signal. This primarily affects angle modulation, because it depends so heavily upon the phase of the received signal for effective demodulation. This drastic change in phase with decreasing  $SIR_i$  is comparable to FM radio. FM radio has a much clearer reception than AM over a broader  $SIR_i$  range, but then quickly drops out, when the  $SIR_i$  has decreased below a certain point.

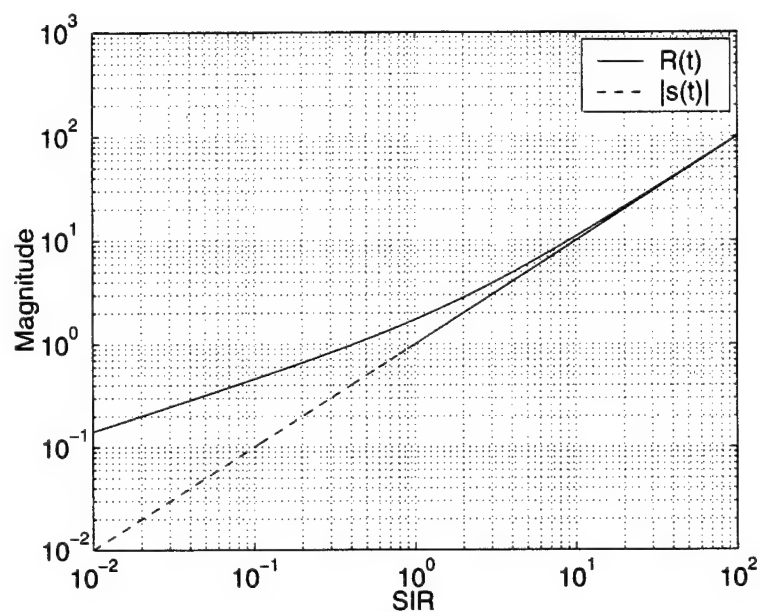


Fig. 3.9. Maximum Amplitude Difference between the Received Signal (Signal plus Noise,  $R(t)$ ) and the Echo Signal ( $|s(t)|$ ) with Respect to Received Signal-to-Interference Ratio (Constant Noise Level as Signal Level Increases)

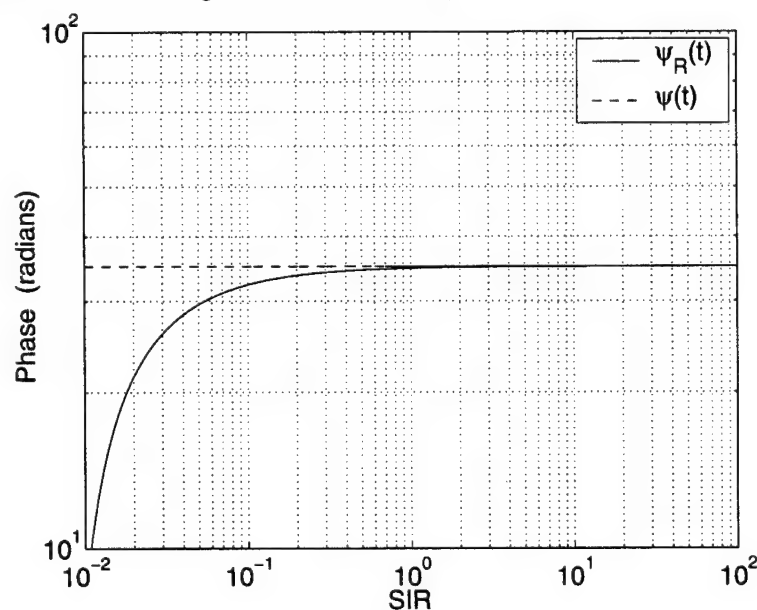


Fig. 3.10. Maximum Phase Difference between the Received Signal (Signal plus Noise,  $\psi_R(t)$ ) and the Echo Signal ( $\psi(t)$ ) with Respect to Received Signal-to-Interference Ratio (Constant Noise Level as Signal Level Increases)

## Chapter 4

### Experiment

The experiment portion of this thesis is divided into five sections to better present the implementation of sub-band modulation techniques in active sonar. First, the numerous factors contributing to waveform design are discussed. Second, the specifications of the waveforms used in this thesis are presented, along with the motivation behind the different combinations of sonar waveforms. Third, the implementation of sub-band modulation process in Matlab is summarized. Fourth, an overview of the simulations used in this thesis is given, paying particular attention to the setup, structure and goals of the simulation experiments. Finally, the conditions and goals behind the in-water experiment section of this thesis are discussed.

#### 4.1 Waveform Design Considerations

Waveform design is an important part of sub-band modulation. Many spectrum considerations need to be taken into account when designing a sub-band modulating waveform, because of the numerous limitations imposed by the transmitting transducer, the demodulation process and the effects of time compression. Therefore, the factors that go into waveform design are expanded upon here.

The transmission of a sub-band modulated waveform is achieved with a transmitting transducer (or array of transducers), and the signal is affected by the frequency response of this transmitter. Each sonar transmitter has a set operating bandwidth, and the spectrum of the sub-band modulating waveform needs to fall within this bandwidth to ensure proper transmission into the underwater environment. Carson's rule (3.23) should be implemented when designing the sonar waveform and selecting the deviation constant, so the spectrum of the sub-band modulating waveform will fall within the transmitter bandwidth.

The effects of time dilation also need to be taken into consideration. The transmitted signal is frequency shifted by the Doppler effect (2.13), and if this shift is large enough, the message signals can be shifted out of the frequency range of the receive transducers. When designing a sub-band modulating waveform, precautions need to be

taken in order to ensure that the signal will not be Doppler shifted out of the receive bandwidth  $B_t$ . The deviation constant  $k_p$  can be selected to meet the desired bandwidth criteria by making general assumptions about the maximum, closing line-of-sight velocity of potential scatterers ( $v_{lmax}$ ) and implementing Carson's rule (3.23),

$$k_p \leq \frac{B_t}{2\omega_{v_{lmax}}} - 1, \quad (4.1)$$

where  $B_t$  is the bandwidth of the transducer and

$$\omega_{v_{lmax}} = \omega_0 \left( 1 + \frac{2v_{lmax}}{c} \right). \quad (4.2)$$

Therefore, the bandwidth of the modulating waveform can be designed so it still falls within the receive bandwidth even in the case of maximum time dilation or compression. Typically, the receive transducer has a bandwidth wide enough to account for the maximum frequency shift, experienced by signals within the transmitter's bandwidth. However, the extra design criteria are taken in account as an additional precaution.

The transmitter response is not always flat over its entire bandwidth. Either only the flattest section of the frequency spectrum of the transducer is utilized, or the deviation constant and the frequencies of the sonar waveforms must be selected in such a way that the sub-band information does not fall within the dips of the transmitter's response. If portions of the modulating sonar signals fall in dips in the transmitter's frequency response, then the information at those frequencies is broadcast at a lower level than the rest of the signal, which may present problems for demodulation.

The selection of the specific sonar waveforms to be used in sub-band modulation is an involved process. Besides choosing a combination of waveforms that can estimate the desired sonar parameters (as discussed in sections 2.3 and 2.4), the waveforms are designed, so they can be spectrally separated after demodulation. When the sonar waveforms are combined linearly as the phase component of a carrier (3.16), they must be spaced far enough apart in frequency, that they can be separated using filtering techniques. The filters used to separate these signals also need to have wide enough passbands ( $B_{filter\ m}$ ) to allow for the potential Doppler shift of the sonar signals (2.13), where

$$B_{filter\ m} \geq 2\omega_m \left( \frac{2v_{lmax}}{c} \right). \quad (4.3)$$

Therefore, waveforms adjacent in frequency should be spectrally spaced according to

$$\begin{aligned}
 \omega_{m+1} &\geq \omega_m + \frac{B_{filter\ m}}{2} + \frac{B_{filter\ m+1}}{2} \\
 \omega_{m+1} \left[ 1 - \frac{2v_{lmax}}{c} \right] &\geq \omega_m \left[ 1 + \frac{2v_{lmax}}{c} \right] \\
 \omega_{m+1} &\geq \omega_m \frac{\left[ 1 + \frac{2v_{lmax}}{c} \right]}{\left[ 1 - \frac{2v_{lmax}}{c} \right]}.
 \end{aligned} \tag{4.4}$$

(3.20) shows, that the sub-bands of the modulation lie at the frequencies  $\sum_{\hat{m}_1=-\infty}^{\infty} \dots \sum_{\hat{m}_N=-\infty}^{\infty} (\omega_0 + \hat{m}_1\omega_1 + \dots + \hat{m}_N\omega_N)$  with magnitudes of  $\prod_{m=1}^N \left[ \sum_{\hat{m}=-\infty}^{\infty} J_{\hat{m}_m}(k_p) \right]$ .

The center frequencies of the sonar waveforms ( $\omega_m$ ) need to be chosen, so there are no significant sidebands at frequencies within the bandwidths of the filters used for post-demodulation signal separation. Prominent sidebands may appear as additional peaks in the matched filter response and should be avoided to ensure effective demodulation.

Filtering is used in the demodulation process to remove unwanted signal components from the sonar signals (sections 3.3.1 and 3.3.2), as well as to spectrally separate the multiple sonar signals. The sonar signal with the lowest center frequency ( $\omega_1$ ) should be designed, so that it's frequency is far enough away from these components to allow for their removal. This filter is a very low frequency bandstop filter with a bandwidth of  $B_d$ . The culmination of the constraints on the sonar waveforms' spectra implemented in sub-band modulation is illustrated in figure 4.1.

## 4.2 Waveform Specifications

Several different combinations of modulating waveforms were implemented throughout the course of this research to verify the effectiveness of sub-band modulation. Specifically, one waveform was used throughout the majority of the research, and several other waveforms were used in parts of the research to verify that the sub-band modulation performance was independent of the types of sonar waveforms used.

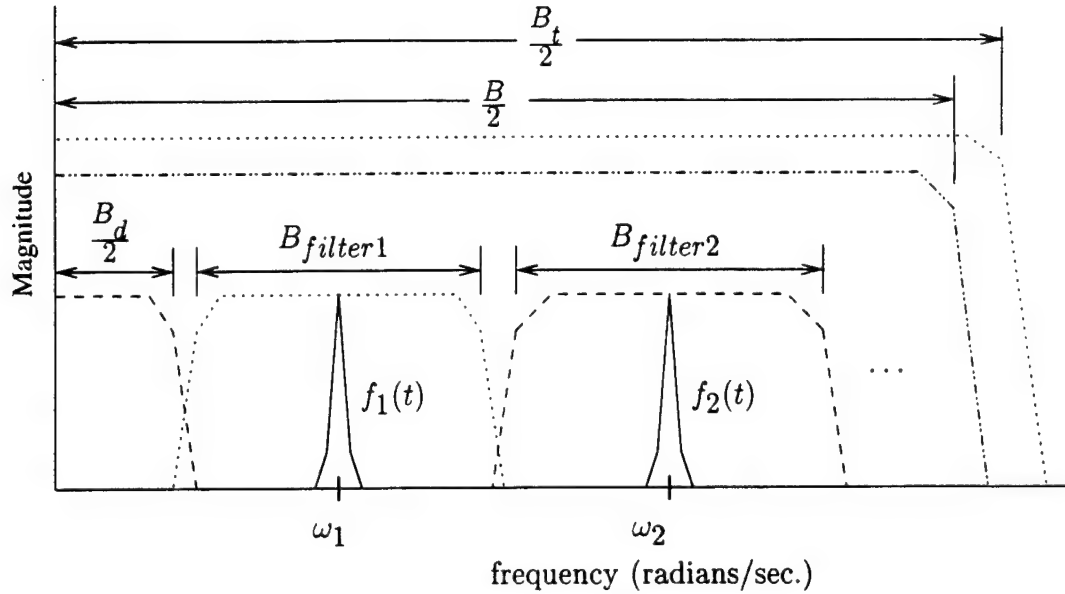


Fig. 4.1. Spectral Constraints of Waveform Design:  $f_m(t)$  Waveform "m" with  $\omega_m$  Center Frequency,  $B_{filter\ m}$  Filter for Separating Waveform "m" from Other Modulating Waveforms,  $B$  Bandwidth of Modulation,  $B_t$  Bandwidth of Receiver and  $B_d$  Low Frequency Bandstop Filter

The primary waveform used in this research is a combination of a CW and a BPSK,

$$\begin{aligned}\psi_a(t) &= k_p \left( f_{BPSK}(t) + \sin(\omega_2 t) \right) \\ &= k_p \left( f_1(t) + f_2(t) \right),\end{aligned}\tag{4.5}$$

where the center frequency of the BPSK ( $f_1(t)$ ) is  $\omega_1$  with a mainlobe bandwidth of  $W_1$  (see figure 4.2a).  $\omega_1$  and  $\omega_2$  are the basebanded center frequencies. The main motivation behind this waveform combination is to simultaneously implement a waveform with high frequency and time resolution along with waveform with poor time resolution. This combination uses the CW to make a detection estimation and to make generalizations about scatterer parameters. Then, the desired high resolution scatterer parameters are extracted from the matched filter response of the BPSK using a more focused bank of



replicas. This waveform combination allows for a coarse approximation of the echo parameters made with a low resolution signal to ease the computational intensity associated with the high resolution signal, as discussed in section 2.4.

This waveform combination was also chosen to verify and investigate the bandwidth constraints of sub-band modulation. Since the BPSK has a reasonably large bandwidth, it's sub-band modulation with any other sonar waveform produces a wideband waveform. Therefore, the BPSK waveform is bandpass filtered to keep the modulating bandwidth within the transducer's bandwidth constraints. It is found, that 95.45% of the signal energy in this BPSK is contained within the mainlobe and the first two sidelobes of the sinc function. The overall bandwidth of the BPSK can be reasonably reduced without compromising the waveform energy by bandpass filtering out some sidelobes. This also allows for wider spectral separation between the two waveforms, in order to facilitate easier signal separation in the demodulation process.

Several other signal combinations are used in parts of this research, to verify that the sub-band modulation performance is independent of sonar signal type. One waveform combination is the CW and LFM

$$\begin{aligned}\psi_b(t) &= k_p \left( \sin(\omega_2 t) + \sin \left( \left[ \omega_1 - \frac{W_1}{2} \right] t + \left[ \frac{\pi W_1 t^2}{T} \right] \right) \right) \\ &= k_p (f_2(t) + f_3(t)),\end{aligned}\tag{4.6}$$

where  $(f_3(t))$  is a LFM centered at  $\omega_1$  with a bandwidth of  $W_1$ , as seen in figure 4.2b. The combination of a signal with good low Doppler performance with a signal with good high Doppler performance is implemented to verify, if sub-band modulating signals could yield good Doppler performance independent of scatterer velocity. Another waveform combination is four CWs of different frequencies,

$$\begin{aligned}\psi_c(t) &= k_p (\sin(\omega_2 t) + \sin(\omega_4 t) + \sin(\omega_5 t) + \sin(\omega_6 t)) \\ &= k_p (f_2(t) + f_4(t) + f_5(t) + f_6(t)),\end{aligned}\tag{4.7}$$

as seen in figure 4.2c. This waveform combination is used to investigate the effects of the number of sub-band waveforms on the modulation process. Finally, a combination of 2 sinewaves of duration  $T$  and two sinewaves of duration  $\frac{T}{2}$  is investigated. This

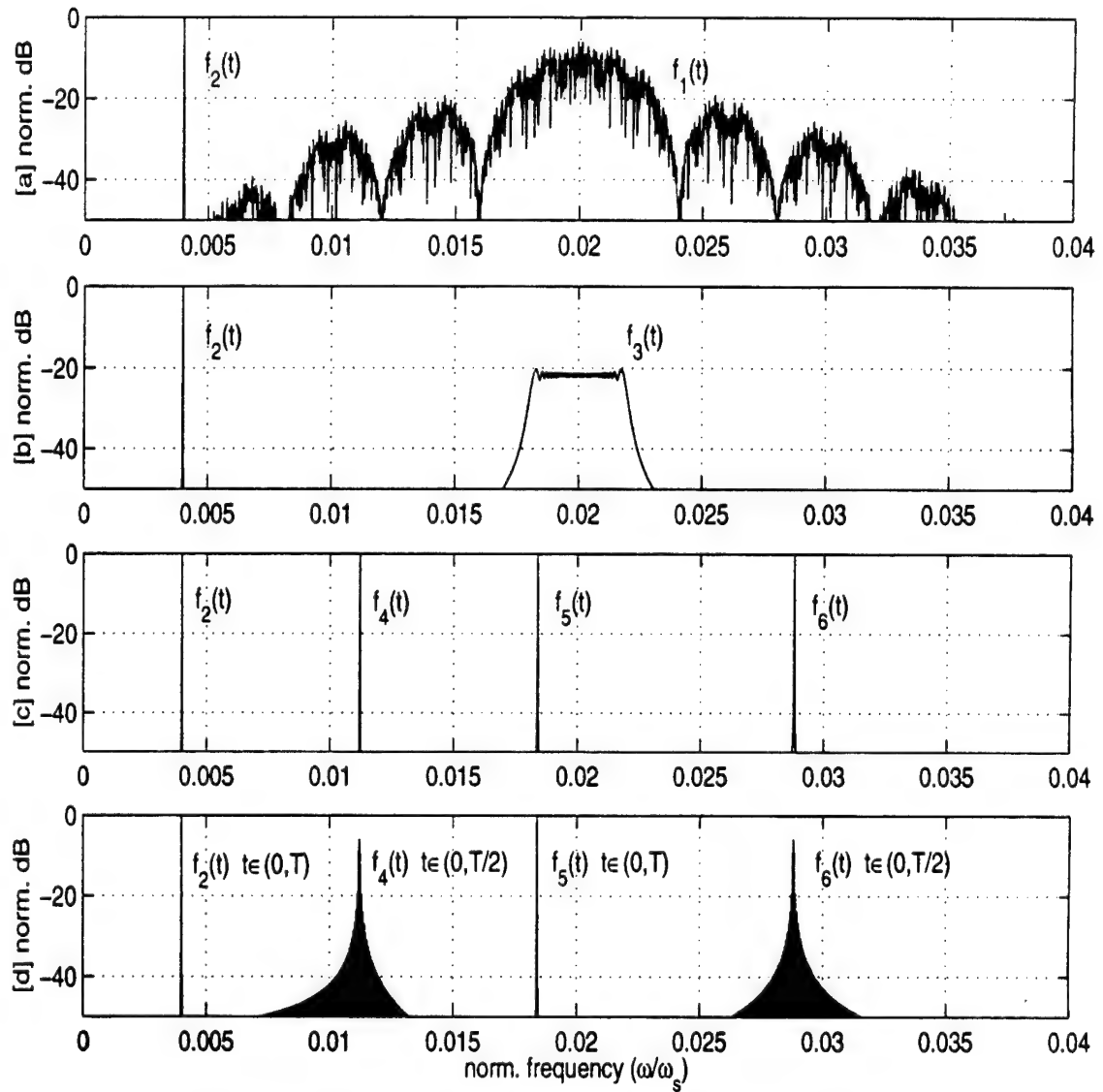


Fig. 4.2. Frequency Spectra of the Waveform Combinations Used in the Experiment (Normalized Frequency to  $\frac{\omega}{\omega_s}$ ); a. BPSK and CW ( $\psi_a(t)$ ), b. LFM and CW ( $\psi_b(t)$ ), c. 4 CWs ( $\psi_c(t)$ ), and d. 2 CWs of duration  $T$  and 2 CWs of duration  $\frac{T}{2}$  ( $\psi_d(t)$ )

combination

$$\psi_d(t) = \begin{cases} k_p (f_2(t) + f_4(t) + f_5(t) + f_6(t)) & : t \in (0, \frac{T}{2}) \\ k_p (f_2(t) + f_5(t)) & : t \in [\frac{T}{2}, T) \end{cases} \quad (4.8)$$

is seen in figure 4.2d. This waveform combination investigates the effects of using waveforms with different durations on sub-band modulation.

Realistically, all of the waveforms used in this thesis would have center frequencies of  $\omega_o + \omega_m$  instead of just  $\omega_m$ , if they were transmit without the use of sub-band modulation. The waveforms are basebanded, before they are sub-band modulated, so the waveforms in the first sub-band of the carrier would be at the same center frequency as those transmitted without sub-band modulation. This was done to minimize the bandwidth of the modulation and to ease processing complexity, by having the sub-band modulated and the equivalent unmodulated signals experience essentially the same Doppler shift.

Once the sonar waveforms are selected, the carrier frequency and deviation constant of the sub-band modulation are carefully considered. The most stringent design parameter in this research is the bandwidth of the transmitting transducer implemented in section 4.5. Since  $\psi_a(t)$  is to be the only waveform combination implemented in all parts of the experimental stage of this research, it's design is highly influenced by these bandwidth constraints. A large, relatively flat portion of the transducer's frequency response is utilized in this research, so the carrier frequency and modulation bandwidth are selected to fit within this frequency range. The carrier frequency  $\omega_0$  is selected to fall in the center of the desired transmit band, and Carson's rule determined the deviation constant, that will keep the maximum frequency shift due to the scatterer velocity within the transmission bandwidth (4.1). The value of the modulation index ( $k_p = 0.5$ ) is also selected so that the first set of sub-bands are much more prominent than most of the other sub-bands. Therefore, the sub-band modulating signals are essentially represented by the first set of sub-bands. Although, these first sub-bands have a low magnitude as compared to the carrier,  $k_p$  is kept small ( $k_p < \frac{\pi}{2}$ ), because a higher modulation index drastically increases the modulation bandwidth along with the sub-band magnitudes, as discussed in section 3.2.1. Since the bandwidth of the modulation is already wide, due to the inclusion of a BPSK, the modulation index is kept relatively small to avoid sub-band modulation outside of the transmission bandwidth. The frequency spectrum of this sub-band modulated signal can be seen in figure 4.3.

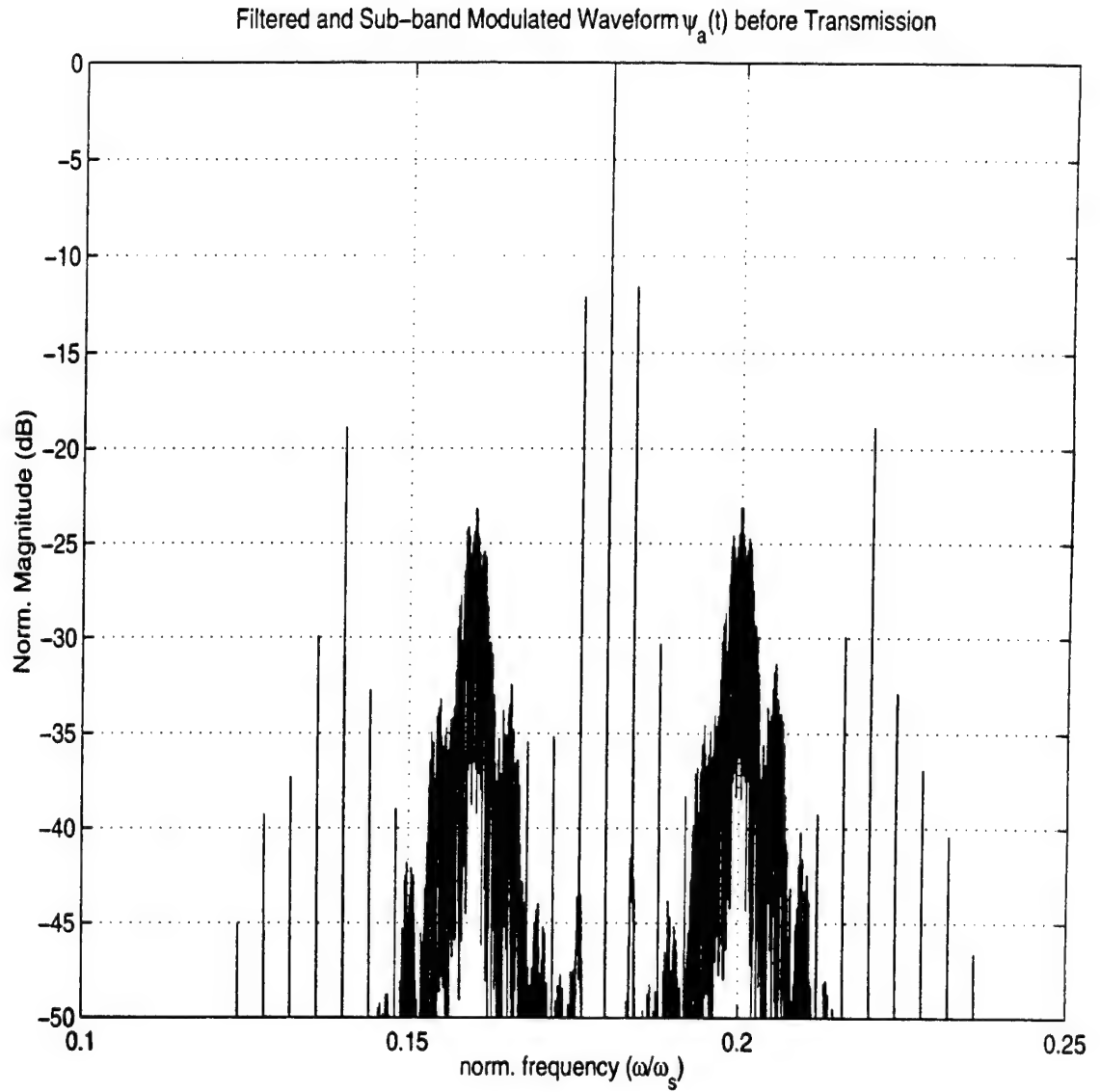


Fig. 4.3. Frequency Spectrum of the Sub-band Modulated BPSK and CW Waveforms in  $\psi_a(t)$  with Modulation Index  $k_p = 0.5$ ,  $\omega_0 = 0.18 \frac{\omega}{\omega_s}$  and  $B = 0.06 \frac{\omega}{\omega_s}$  Immediately before Transmission (Normalized Frequency to  $\frac{\omega}{\omega_s}$ )

Although  $k_p$  was chosen according to the design criteria in section 4.2 for use with signal combination  $\psi_a(t)$ , it was subsequently used for all four test signal combinations, because they had very similar bandwidths. This modulation index's effectiveness with all four test signal combinations was confirmed through a series of simulations, where different deviation constants were compared. One possibility for future work may be to investigate a sub-band modulating signal with a narrower modulation bandwidth, so a more extensive analysis of the modulation index may be made.

### 4.3 Matlab Implementation

This section of the thesis is devoted to the application of sub-band modulation theory as a series of signal processing programs. The waveform generation, sub-band modulation, demodulation, signal manipulation and echo processing in this research are all implemented in Matlab version 5.3 with Signal Processing Toolbox [14]. This section provides a general overview of the sub-band modulation processes in Matlab, which will then be applied in the simulation and in-water experiment sections of this thesis (sections 4.4 and 4.5).

Most of the waveforms in this research are generated using standard mathematical functions in Matlab. The one exception is the BPSK, which is generated with a function created by Anthony J. Cutezo [6]. These discrete waveforms are generated at a sampling rate of  $\omega_s$ , where  $\omega_s \gg \omega_0 \gg \omega_m$ .

Amplitude, phase/sub-band and frequency modulation are achieved using the "modulate()" command from the Signal Processing Toolbox. The source code for this function was compared to the modulation theory discussed in section 3.2 directly applied in Matlab, and was found to yield identical results. Since the "modulate()" function is less computationally intensive than the independently developed modulation functions, it is used through out this research. This applies to the "demod()" function for demodulation, as well. Matlab also has numerous filtering functions, that can be used to separate the demodulated echo signals spectrally or to represent the bandwidth of the transducer.

The frequency matching of the carrier for demodulation is implemented in Matlab with a fast Fourier transform (fft) of the scatterer return portion of the received time series. The narrowband frequency shift of the carrier signal can be approximated from the resulting frequency spectrum. The rough estimation of the carrier's narrowband frequency shift is a close enough approximation of the time dilation of the carrier, that it

can be used with the ideal discriminator. However, this method of frequency matching is only effective in high receive signal-to-interference situations, where the scatterer return is discernible from the rest of the received time series.

The processing of the individual sonar signals is also implemented in Matlab. After the data is read into Matlab, the time series data is displayed to verify that the echo signal is present in the data. Since the overall data set can be several seconds long at a high sampling frequency, the echo return is cropped from the received data for processing. Processing time and complexity are greatly alleviated by only processing the echo return portion of the received data. Then, the echo location in the received data is noted and applied to the matched filter responses to achieve the desired range-to-scatterer estimations. This method does not work as well in the case of low signal-to-interference ratio. When the signal-to-interference ratio is so low, that the scatterer return could not be discerned from the reverberation, alternative methods were used to locate it. A priori knowledge of the scatterer's location was utilized in the simulations, and observations recorded during data collection aided in locating scatterer returns in the in-water data. This did help in locating the scatterer returns in the time series with low signal-to-interference ratio levels. However, it is not a practical method to use in a "real" sonar detection scenario, because it relies on already knowing the scatterer's location, before it is estimated. Although, such information is not available in "real" detection scenarios, the purpose of this research is to verify that echo parameters can be estimated from sub-band modulating signals, which is still achieved using this process. Therefore, it is reasonable to apply in this research. Topics for future research may include more extensive processing techniques, that allow for processing the entire set of received data more effectively and efficiently.

#### **4.4 Simulations**

Two sets of simulations were completed as part of this research. One is a simple ocean setup to verify the entire sub-band modulation process, and the other is a simulation of the in-water experiment to better understand the field results. The former is discussed here, while the later will be presented in section 4.5 along with the actual in-water portion of this research for better comparison between the two.

The sonar simulations in this research were created using methods outlined in [8], which will be referred to as the synthetic data generation process (or SDG) in the remainder of this thesis. The SDG process simulates sound propagation, the ocean

environment, ocean surfaces, scatterers, scatterer echos, reverberation and background noise. The SDG process allows for easy implementation with Matlab, so the signals can be generated and modulated in Matlab, sent to the SDG process for signal propagation simulation, and then read back into Matlab for demodulation and processing.

The purpose of this portion of the research is to demonstrate that sub-band modulation is a viable option for active sonar. Therefore, a simple direct path ocean environment without boundary reflections is implemented. A single point scatterer at the same depth as the sonar platform is used in a uniformly deep ocean environment, which allows for a single speed of sound to be used instead of an entire sound velocity profile for the different strata in the ocean. The transmit and receive beams on the sonar transducer are omnidirectional, so the effects of beam directionality does not effect the data. The simulation is designed to be as simple as possible, so the effects of reverberation, target velocity, and target range on sub-band modulation can be investigated without the scattering effects of boundary interactions.

The main experiment consists of two hundred and forty simulations using the combination BPSK and CW signal  $(\psi_a(t))$ . Different scatterer velocities are implemented to test the effect of time dilation on demodulation and detection with a sub-band modulated signal. The varying scatterer velocity also permitted for the evaluation of the detection performance of the sub-band signals with and without frequency matching in the discriminator. A small number of these simulations were also used to test the performance of the coupled demodulation, hypothesis testing process. This experiment is further subdivided according to the signal-to-interference ratio at the receiver  $(SIR_i)$ , to investigate the effects of interference on the demodulation and detection of a sub-band modulated signal. These  $SIR_i$  values were achieved by varying the location and the scattering strength of the scatterer, and all of the simulations evaluated fall within a  $\pm 1.5$ dB range of the desired value. This range of  $SIR_i$  values is needed, because both the target and reverberation were randomized by the synthetic data generation process to provide a more realistic simulation. The signal-to-interference ratio at the receiver  $(SIR_i)$  is used instead of the signal-to-interference ratio at the matched filter output  $(SIR_o)$ , because it permits the direct comparison between the performance of a sub-band modulating signal and the performance of the same unmodulated signals in equivalent interference.

Two hundred and forty simulations using unmodulated BPSK and CW signals were also generated for comparison with the sub-band modulated signals. These simulations had the same parameters as the previous simulations, only the signals were not sub-band modulated. The sonar waveforms used (the BPSK  $f_{uh1}(t)$ ) and (the CW  $f_{uh2}(t)$ ) were the same as the sub-band modulating signals in the previous simulations  $f_1(t)$  and  $f_2(t)$ , except they are centered at  $\omega_o + \omega_1$  and  $\omega_o + \omega_2$  respectively instead of being basebanded. This is done, so the unmodulated signals measured at the receiver can be directly compared to the received sub-band modulated signals, which are frequency translated up to the carrier frequency once they are demodulated (as discussed in section 3.3.1). The results of this comparison are presented and analyzed in chapter 5.1.

The other experimental sets with the waveform combinations  $\psi_b(t)$ ,  $\psi_c(t)$  and  $\psi_d(t)$  were carried out in the same manner as  $\psi_a(t)$ , except fewer simulations were completed for each set. Each set only consisted of seventy-two simulations for the sub-band modulated signals and seventy-two additional simulations for the equivalent, unmodulated signals. These experimental sets did not need to be as extensive as the first one, since their main purpose was to investigate the influence of signal type and number of modulating signals on detection with sub-band modulated signals and verify the performance of the first experimental set.

## 4.5 In-Water Data

A small in-water experiment was also completed as part of this research. The sub-band modulating signal combination of  $\psi_a(t)$  was used on twenty-four separate instances to interrogate a scatterer with Doppler. The purpose of this portion of the research was to experimentally verify the detection performance observed in the simulations. Although not enough interrogations were completed to generate detection statistics, the data was used to validate the results gathered in section 4.4.

The ocean environment was similar to the simulation set up discussed in section 4.4, however the sound propagation was much more complex. Since the sound propagation could not be limited to the direct path between the sonar platform and the scatterer, surface and bottom bounces were also included in the received data. A varying sound velocity profile also affected the propagating sonar signals, as did the high volume attenuation in the medium. All of these factors contributed in creating a very strong reverberation level. Although the ocean environment was not too different from the one used in the simulations, the added complexity of the real ocean environment and higher



reverberation levels decreased the detection performance of the sub-band modulating signals.

Although the sonar platform and the scatterer were somewhat similar to the ones simulated in section 4.4, they also exhibited some key differences, which inevitably influenced the comparison between the simulated data and the in-water data. The transmitter/receiver on the sonar platform was a thirty-seven element array of transducers instead of a single omni-directional transducer, and the receive beam of the array was steered to track the scatterer position. This steering was done both physically during the data collection and with beamforming techniques during the processing, to ensure that the scatterer fell within the mainlobe of the receive beam. This provided the highest  $SIR_i$  and chance for detection. The weighting and filtering for the received array data was completed in Matlab. While the steering of the receive beam increased the probability of detection, the geometry of the experiment resulted in exceptionally small Doppler values. The sonar platform was stationary over all of the interrogations, while the scatterer always produced a small Doppler shift in the backscattered signal. A carrier without a frequency shift was used in the demodulation process, because the scatterer induced Doppler was close to zero for most of the interrogations, and because the  $SIR_i$  was so low, that the scatterer return could not be discerned from the rest of the time series for frequency matching. Attempts at frequency matching were made, but ultimately the first method ended up being more effective.

The distance between the scatterer and sonar platform was much larger in the in-water portion of the research than in the simulations, which resulted in smaller signal-to-interference ratio measurements at the receiver. The scatterer was also at a greater depth in the ocean than the sonar platform, so the temperature and salinity strata in the ocean had a greater effect on the propagating signal, which was not taken in account in the simulations. Several attempts were made to better model the in-water data in the synthetic data generation process by implementing more complex simulations. This did not significantly aid the analysis of the in-water data, or provide additional insight into the performance of the sub-band modulated signals in the in-water scenarios, so further simulations were suspended.

Despite the differences between the in-water experiment and the simulations, the results verified that sub-band modulation can be accomplished in realistic situations. The analysis of the in-water data serves as a confirmation of the results obtained from the simulations. The results of this comparison are presented and analyzed in chapter 5.2.

## Chapter 5

# Results and Analysis

## 5.1 Simulation Analysis

An analysis of the detection performance of sub-band modulation is made through the comparison of matched filter responses for different signal combinations and scenarios. First, a few individual matched filter responses for sub-band modulated and equivalent unmodulated signals are compared in order to analyze the sub-band modulation process's effect on matched filter peak shape, location and detection resolution. Next, the average matched filter peak responses versus signal-to-interference ratio at the receiver for sub-band modulated and unmodulated signals are investigated, and the effects of interference on scatterer detection for each process are compared.

The matched filter responses for several of the sub-band modulated signals were compared to the matched filter responses of the equivalent unmodulated signals to ensure, that the signals were not distorted by the sub-band modulation process. The goal of this analysis is to verify that the same delay and Doppler information can be gathered with the sub-band modulated signals, that is gathered with the equivalent unmodulated signals. Figure 5.1 compares the matched filter response of the sub-band modulated and demodulated BPSK and CW signals from simulation set  $\psi_a(t) (s_{dh\ 1}(t)[a] \text{ and } s_{dh\ 2}(t)[c])$  with the equivalent unmodulated signals  $(s_{uh\ 1}(t)[b] \text{ and } s_{uh\ 2}(t)[d])$  to a stationary scatterer at an  $SIR_i$  of 20dB. The carrier used with the discriminator matched the received carrier frequency in this case. Both the sub-band modulated BPSK and CW signals estimated identical scatterer delay and Doppler parameters to the equivalent unmodulated signals. Furthermore, the delay and Doppler parameters estimated with the matched filters accurately represented the scatterer parameters set up in this simulation. The overall phase-plane shapes of the matched filter response peaks are also almost identical, which indicates that the sub-band modulation did not significantly distort the sonar signals. The particular replica maps used in this portion of the thesis were chosen, because they provided a large enough delay-Doppler range to observe the matched filter response in a broader section of the phase-plane than just the area immediate to the peak response. Although this did slightly compromise the detection resolution, it was

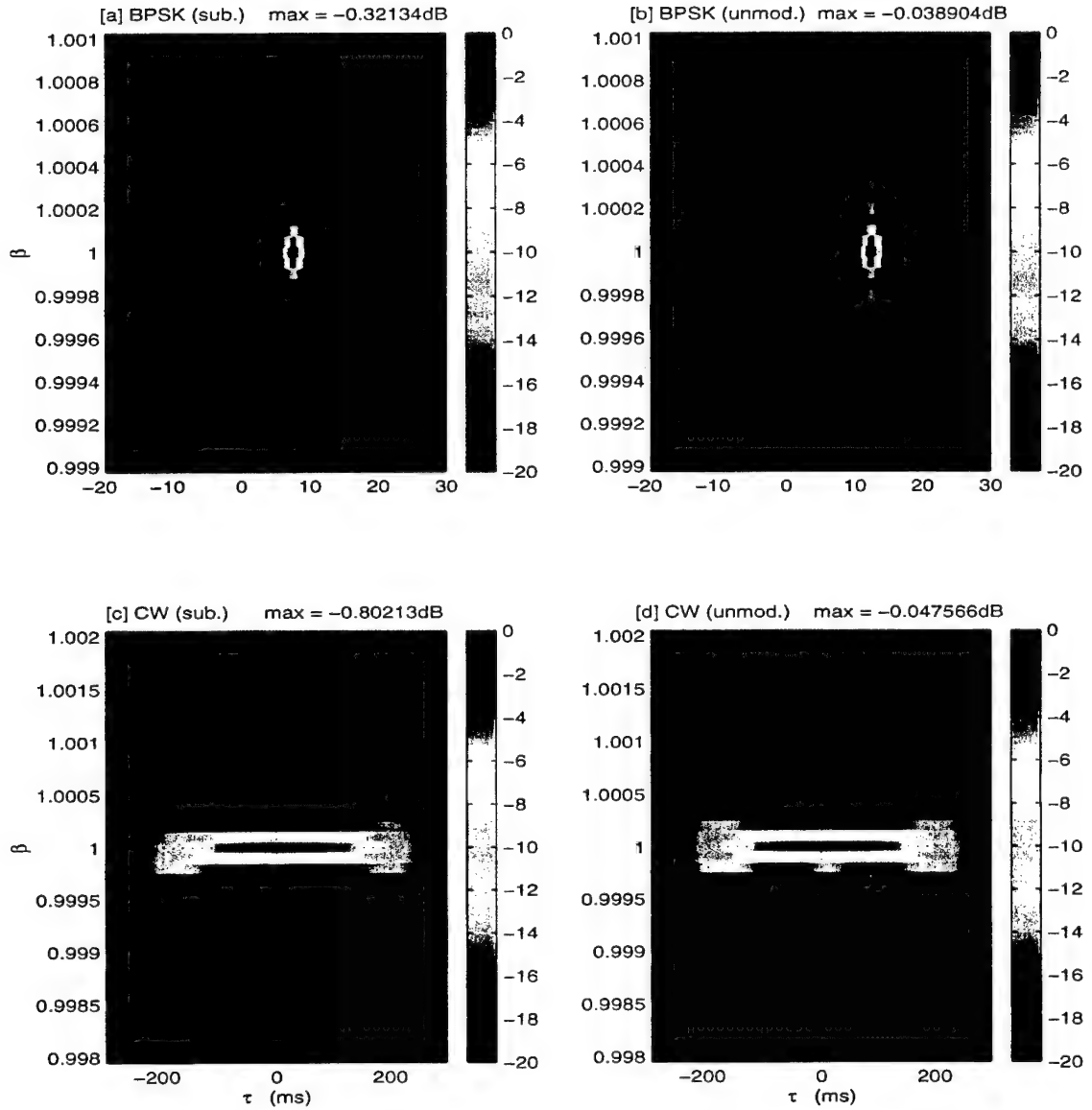


Fig. 5.1. Comparison between Matched Filter Responses of Sub-band Modulated and Unmodulated BPSK and CW Signals at 20dB  $SIR_i$  (stationary scatterer and matched carrier): [a]  $s_{dh1}(t)$  Sub-band Modulated BPSK in  $\psi_a(t)$ , [b]  $s_{uh1}(t)$  Equivalent Unmodulated BPSK, [c]  $s_{dh2}(t)$  Sub-band Modulated CW in  $\psi_a(t)$ , and [d]  $s_{uh2}(t)$  Equivalent Unmodulated CW

done to ensure that no abnormalities were generated in the matched filter response by the sub-band modulation process. The only difference in the matched filter responses of the sub-band modulated signals of simulation set  $\psi_a(t)$  and the responses of the corresponding unmodulated signals is a decrease in the peak response level of the sub-band modulated signals by approximately 1dB. This discrepancy represents a drop in correlation from  $\sim 1$  to  $\sim 0.9$  between the received signal and the replicas. This indicates, that the sonar signals are slightly distorted by the sub-band modulation process, but the amount of distortion is minimal. It is also important to take into account, that the signal energy was split between the sub-band modulating signals. While both the modulated and unmodulated signals had approximately the same  $SIR_i$  levels when received, the signal energy is split between the individual sub-band signal, once they are demodulated. Therefore, the signal-to-interference ratio is lowered for each of the demodulated signals. Furthermore, it will be shown later in this section, that detection performance decreases as the signal-to-interference ratio decreases. When this is taken into consideration, it is not unreasonable to expect a decrease in matched filter level of the sub-band modulated signals, as compared to the unmodulated responses at the same  $SIR_i$ .

The matched filter responses of these same signals are also compared for a closing scatterer at 3 (m/sec.) and an opening scatterer at -3 (m/sec.) (figures 5.2a-d and 5.3a-d respectively). The same carrier used above was implemented in these demodulation processes, which resulted in a carrier mismatch. Although both sets of figures indicate that sub-band modulated signals estimate the same delay and Doppler parameters of a scatterer as the equivalent unmodulated sonar signals, the differences between peak levels of the matched filter responses for the sub-band modulated signals and the equivalent unmodulated signals are much greater than the differences seen in figures 5.1a-d for the stationary scatterer. The matched filter peaks for the moving scatterers were approximately 6dB lower than the peaks for the stationary scatterer (or a drop in correlation to  $\sim 0.5$ ). This decrease in peak matched filter level is a result of the frequency mismatch between the carrier of the received echo signal from a moving scatterer and the carrier implemented in the demodulation process, which further distorts the received signals.

A series of simulations were completed to characterize the performance of sub-band modulation, when a mismatched carrier is implemented in the demodulation process due to a moving scatterer. A series of simulations were run using the experimental set up discussed in section 4.4. The scatterer velocity ranged from 9(m/sec.) to -9(m/sec.), and all of the data used was taken at 7dB  $SIR_i$  ( $\pm 1.5$ dB). All of the simulations were

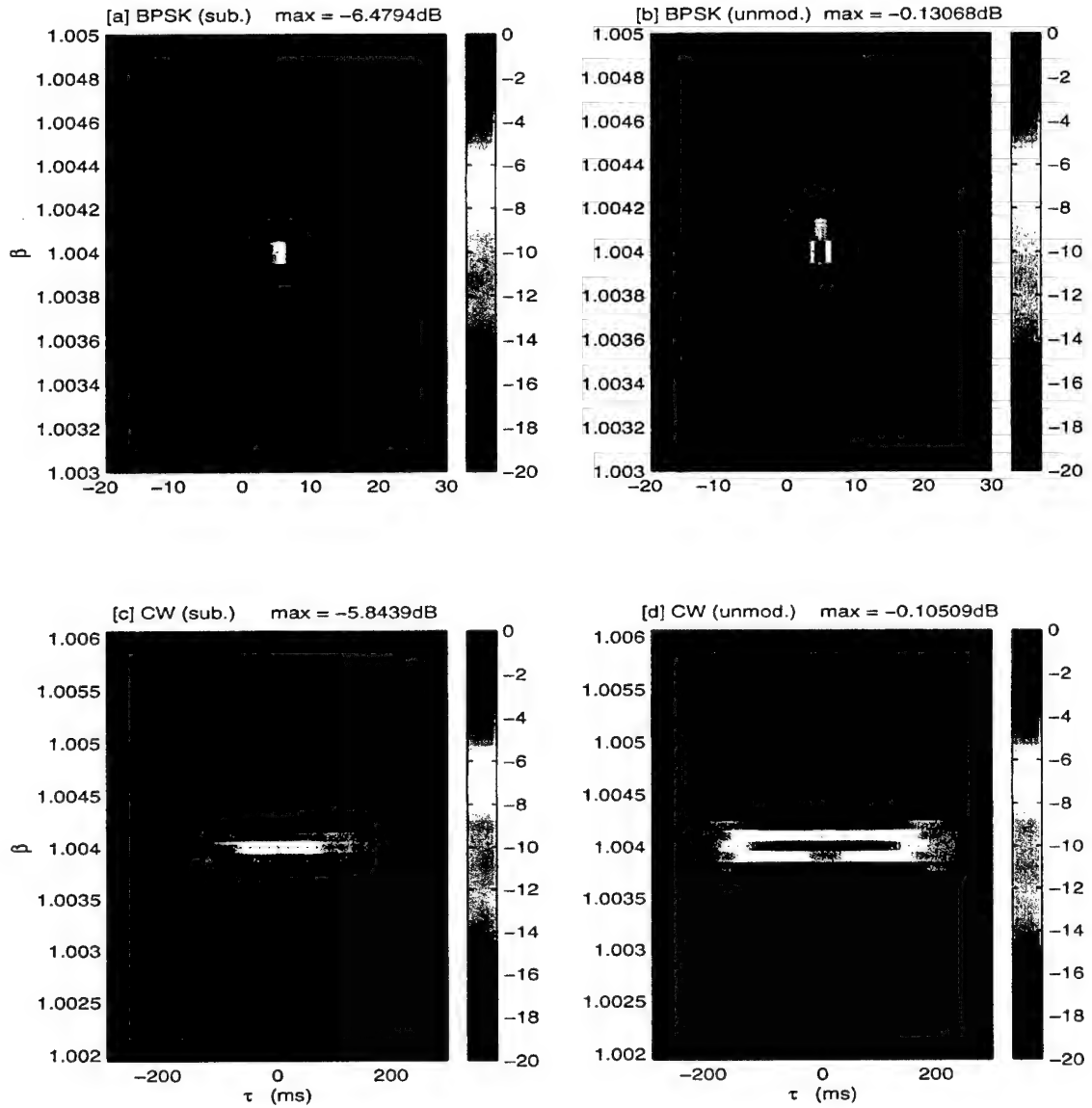


Fig. 5.2. Comparison between Matched Filter Responses of Sub-band Modulated and Unmodulated BPSK and CW Signals at 20dB  $SIR_i$  (closing scatterer at 3 (m/sec.) and mismatched carrier): [a]  $s_{dh1}(t)$  Sub-band Modulated BPSK in  $\psi_a(t)$ , [b]  $s_{uh1}(t)$  Equivalent Unmodulated BPSK, [c]  $s_{dh2}(t)$  Sub-band Modulated CW in  $\psi_a(t)$ , and [d]  $s_{uh2}(t)$  Equivalent Unmodulated CW

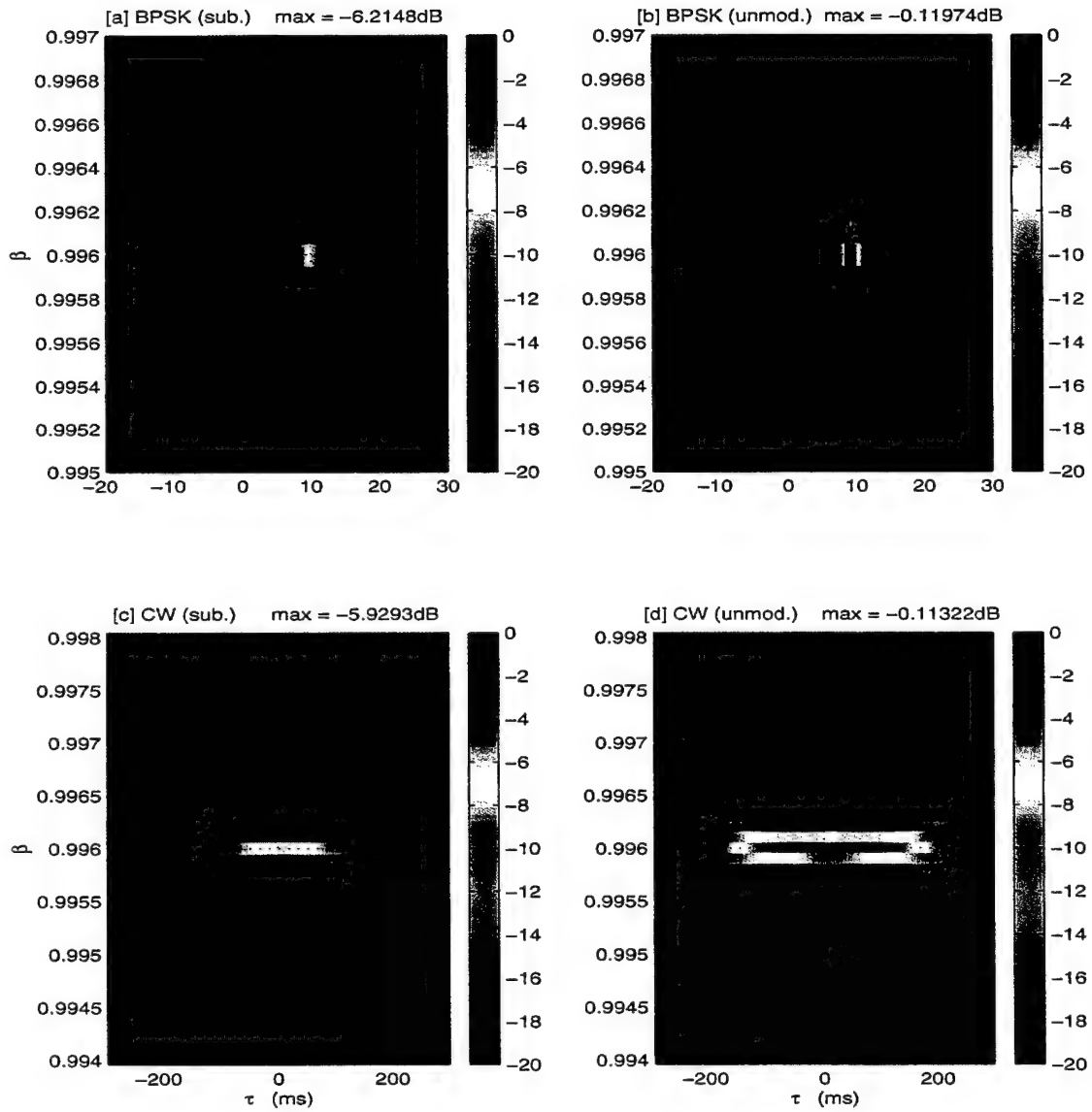


Fig. 5.3. Comparison between Matched Filter Responses of Sub-band Modulated and Unmodulated BPSK and CW Signals at 20dB  $SIR_i$  (opening scatterer at -3 (m/sec.) and mismatched carrier): [a]  $s_{dh1}(t)$  Sub-band Modulated BPSK in  $\psi_a(t)$ , [b]  $s_{uh1}(t)$  Equivalent Unmodulated BPSK, [c]  $s_{dh2}(t)$  Sub-band Modulated CW in  $\psi_a(t)$ , and [d]  $s_{uh2}(t)$  Equivalent Unmodulated CW

demodulated using the unshifted carrier frequency ( $\omega_0$ ), which produced matched filter responses for a wide range of mismatched carrier frequencies. Three simulations resulting in matched filter detections were computed at each of the different scatterer velocities, and each set of three peak matched filter levels were averaged. This was done to ensure that the typical peak level of the matched filter output and not an atypical response was analyzed. The averaged peak responses were then plotted versus the difference between the transmitted and received carrier frequencies. Figure 5.4 shows a 6dB difference between the peak matched filter response when the received and demodulated carrier frequencies are identical and when they are not. This equates to a drop in the correlation between the received signal and the replicas from  $\sim .9$  to  $\sim .5$ . The figure also shows that the performance of the sub-band signals demodulated with a mismatched carrier does not vary significantly as the frequency difference increases. Additional simulations were conducted over a range of small scatterer velocities near 0 (m/sec.) to establish a frequency mismatch for the demodulation process. It was found, that a range of frequencies 1.5Hz above and below the carrier (or  $\Delta\omega = \pm 0.2387$  radians) produced detection peaks equivalent to the frequency matched response. This also corresponded to the narrowband Doppler resolution of the signal (2.35). Therefore, carrier frequency mismatches falling within this tolerance can still be considered matched. Another series of simulations was demodulated with a carrier, that matched the received carrier frequency from a scatterer closing at 3(m/sec.). The results from these simulations were identical to those observed in figure 5.4. A prominent peak was observed at the matched frequency and the performance at the mismatched frequencies were approximately 6dB lower. Therefore, sub-band demodulation yields more desirable results when the received signal is demodulated with a matching carrier (within the tolerance), but it does yield detection results for mismatched carriers and that performance was relatively constant over the range of scatterer velocities investigated. These results are also displayed for the BPSK and CW in  $\psi_a(t)$  in figure 5.5, where the performance of the sub-band signals demodulated with a mismatched carrier, the sub-band signals demodulated with a matched carrier and the equivalent unmodulated signals are compared.

Similar detection performance was observed when comparing the signals of  $\psi_b(t)$ ,  $\psi_c(t)$  and  $\psi_d(t)$  with corresponding unmodulated signals. Examples of this performance for the LFM and CW signals of  $\psi_b(t)$  against a stationary scatterer are seen in figures 5.6a-d. All of the sub-band modulated signals investigated yielded delay and Doppler information consistent with the scatterer information estimated with the corresponding

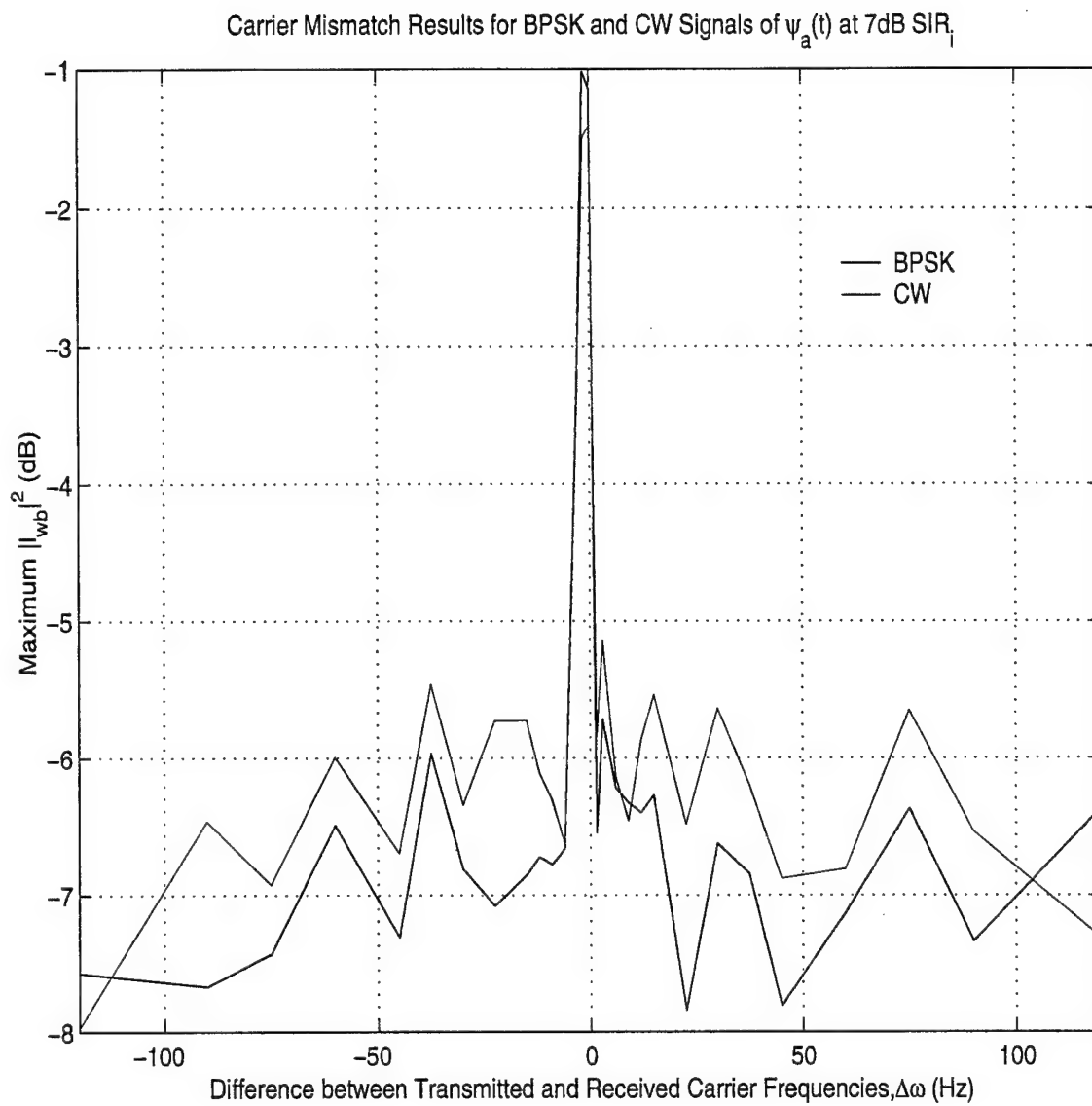


Fig. 5.4. Carrier Mismatch Results for BPSK and CW Signals: Magnitude of Matched Filter Peaks vs. Frequency Difference between the Received Carrier and the Carrier Implemented in the Demodulation Process



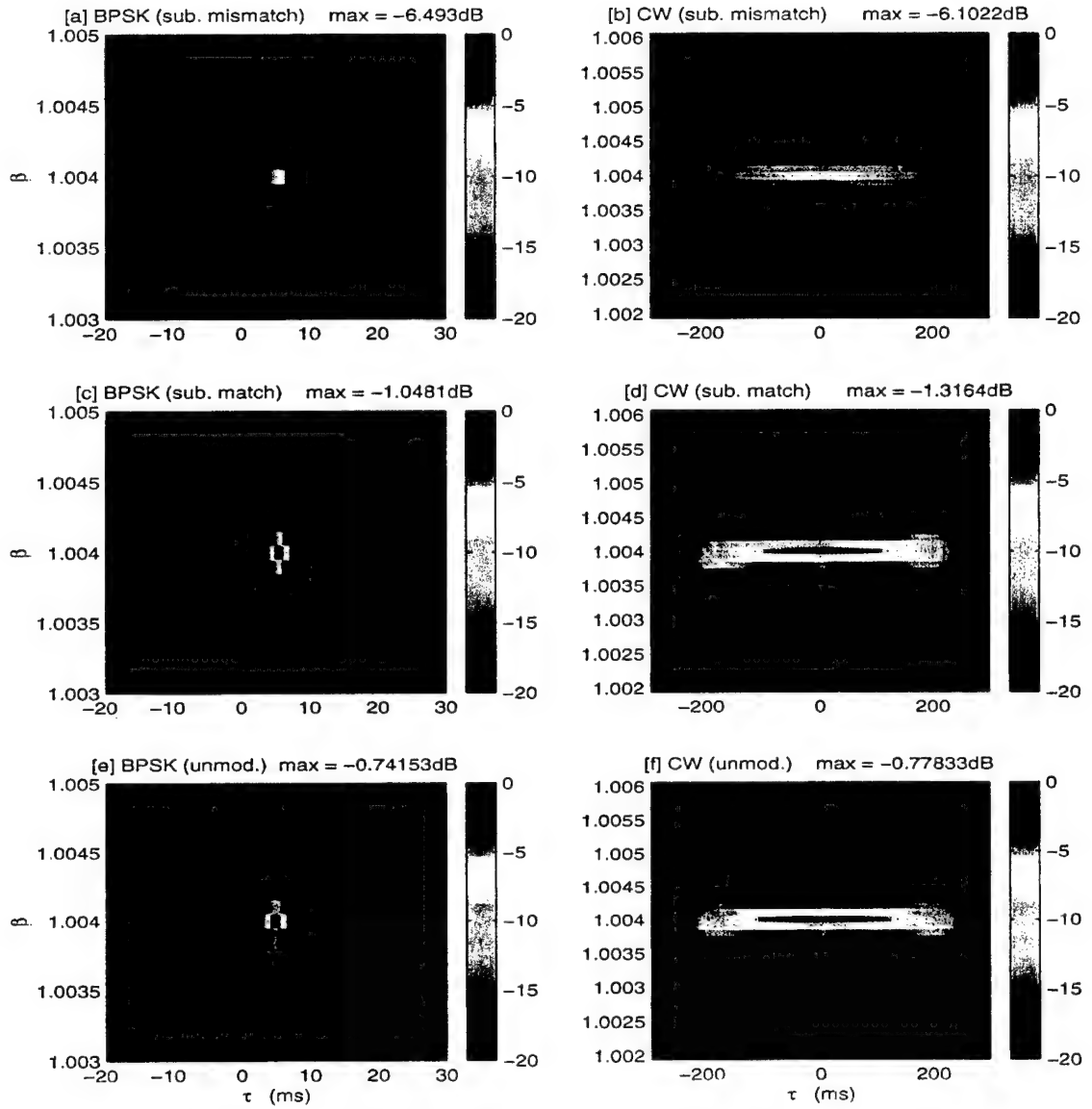


Fig. 5.5. Comparison between Matched Filter Responses of BPSK and CW Signals at 7dB  $SIR_i$ : Sub-band Modulated with Matched Carrier, Sub-band Modulated with Mismatched Carrier and Unmodulated (closing scatterer at 3(m/sec.) ): [a]  $s_{dh1}(t)$  Sub-band Modulated BPSK with Mismatched Carrier (Large Mismatch) , [b]  $s_{dh2}(t)$  Sub-band Modulated CW with Mismatched Carrier, [c] Sub-band Modulated BPSK with Matched Carrier (within Tolerance) , [d] Sub-band Modulated CW with Matched Carrier, [e]  $s_{uh1}(t)$  Equivalent Unmodulated BPSK, and [f]  $s_{uh2}(t)$  Equivalent Unmodulated CW

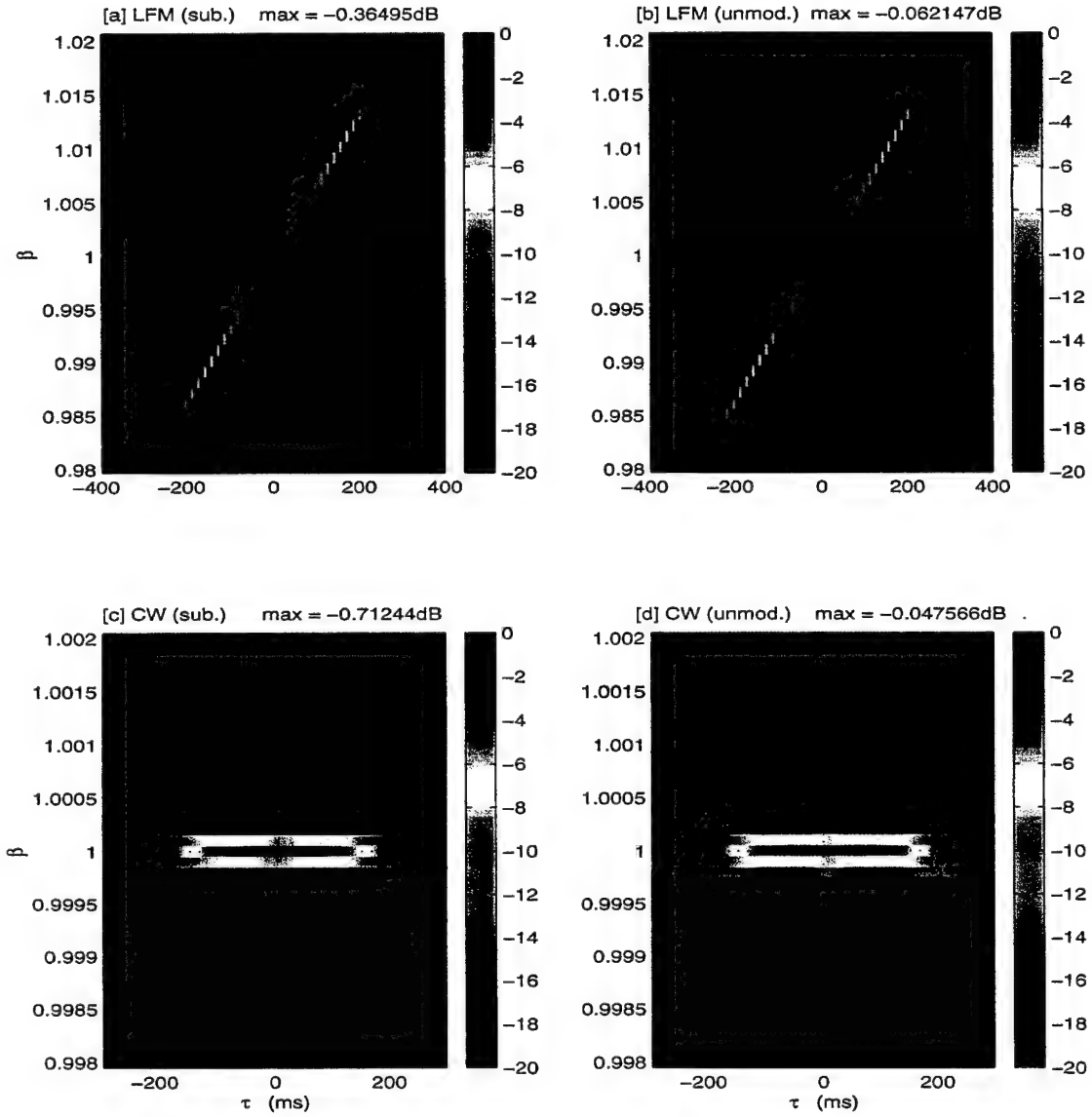


Fig. 5.6. Comparison between Matched Filter Responses of Sub-band Modulated and Unmodulated LFM and CW Signals at  $20\text{dB } SIR_i$  (stationary scatterer and matched carrier): [a]  $s_{dh\ 3}(t)$  Sub-band Modulated LFM in  $\psi_b(t)$ , [b]  $s_{uh\ 3}(t)$  Equivalent Unmodulated LFM, [c]  $s_{dh\ 2}(t)$  Sub-band Modulated CW in  $\psi_b(t)$ , and [d]  $s_{uh\ 2}(t)$  Equivalent Unmodulated CW

unmodulated signals. They also exhibited the same decreased matched filter performance as the signals of  $\psi_a(t)$ , when demodulated with a mismatched carrier. The only significant difference observed was a slight decrease in the peak matched filter levels for the CW signals in simulation sets  $\psi_c(t)$  and  $\psi_d(t)$  by  $\sim 1\text{dB}$  in both the matched and mismatched carriers cases. A decrease was to be expected, since the signal energy is split between four sonar signals in these sets, instead of only two as in sets  $\psi_a(t)$  and  $\psi_b(t)$ . Therefore, it can be concluded, that the peak matched filter response for each signal decreases according to the number of sub-band signals modulating a given carrier, but their responses are otherwise undistorted. However, all of the signals used in each of the simulations sets behaved similarly for the most part, which illustrates that the sub-band modulation detection performance is independent of signal type, but is dependent on number of modulating signals to a certain degree.

Although demodulating received sub-band signals with matching carriers yields stronger matched filter responses than those of signals demodulated with mismatched carriers (figure 5.5), matching the received carrier frequency with an ideal discriminator presents other problems. There is no a priori knowledge of the carrier frequency, so it needs to be measured in order to be matched. Frequency matching (or frequency tracking) of the received signal requires an estimation of the Doppler-shifted carrier frequency, which can be very time consuming and computationally intensive. This is especially difficult, when the  $SIR_i$  is low. The effects of matched versus mismatched carrier demodulation on detection performance coupled with frequency matching difficulties prompted an investigation into the implementation of the demodulation process as part of the hypothesis testing. The received signal was demodulated with an array of time dilated carriers, as discussed in section 3.3.1, and the resulting array of demodulated signals were spectrally separated. The arrays of signals were matched filtered, and an improvement in detection performance was observed (figure 5.7). Only a small number of simulations were completed using this method of demodulation and hypothesis testing, but they did yield positive results. Since the coupled demodulation, hypothesis testing process implements frequency matching, it is not surprising, that resulting matched filter responses had maximum values around the same level as the matched carrier responses seen earlier in this analysis. The detection performance observed in these experiment demonstrate that a further investigation into the implementation of demodulation as part of hypothesis testing would be a good topic for future research. This performance also indicates, that it may be worthwhile to investigate demodulators with frequency tracking, such as the phase locked loop discussed in section 3.3.1.

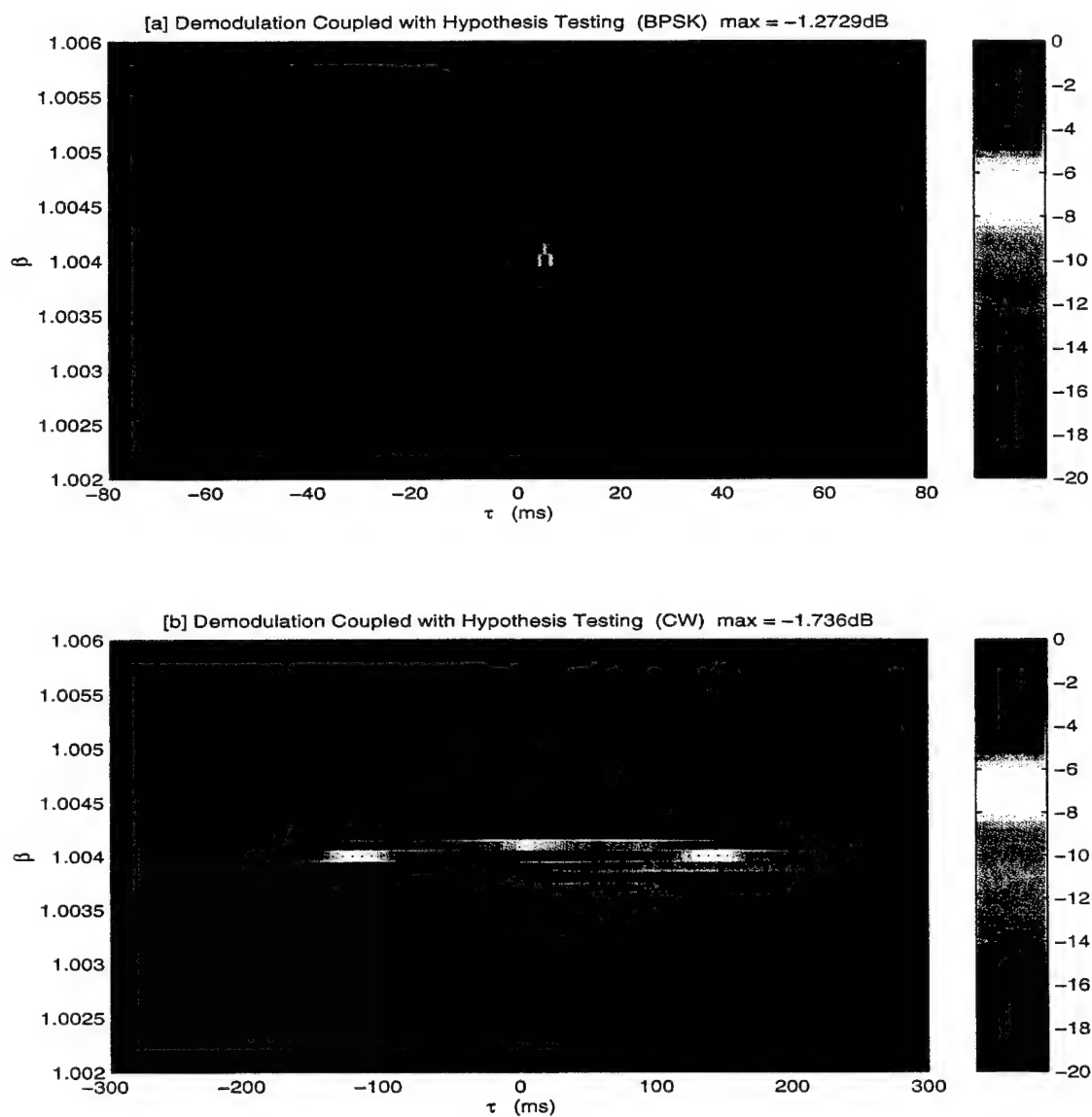


Fig. 5.7. Matched Filter Responses of Sub-band Modulated BPSK and CW signal Combination  $(\psi_a(t))$  at 7dB  $SIR_i$ , when Demodulation is Coupled with Hypothesis Testing: [a]  $s_{dh1}(t)$  Sub-band Modulated BPSK and [b]  $s_{dh2}(t)$  Sub-band Modulated CW

The effects of noise and interference on the detection performance of the sub-band modulating signals were investigated through the analysis of the resulting matched filter responses at different  $SIR_i$  levels. A series of simulations were conducted over a range of  $SIR_i$  values from 20dB to -13dB with the BPSK and CW signals in  $\psi_a(t)$ . Ten detections were made at each  $SIR_i$ , and their peak matched filter response levels were then averaged. These average peak levels for the matched filters were then plotted with respect to  $SIR_i$ . This was done with a stationary scatterer, and then repeated with a scatterer closing at 3(m/sec.) using the same carrier for demodulation to observe the effects of a mismatched carrier on the noise performance of the sub-band signals (figure 5.8). Since the scatterer parameters are controlled in these simulations, it was straight forward to verify the accuracy of the parameter estimations made with the matched filters. This was done, so only accurate detections were used as the ten peak matched filter responses averaged at each  $SIR_i$  investigated. Therefore, the effects of interference on the performance of the sub-band modulating signals could be assessed independently, instead of coupled with the probability of detection. A proper investigation of the probability of detection for the ideal discriminator would be more meaningful, when compared with the probability of detection of several other demodulators. This comparison is another topic left for future research.

Figure 5.8 shows a decrease in the peak matched filter responses as the signal-to-interference ratio at the receiver decreases. Since the curves for the BPSK and CW signals were essentially the same for each case, they were combined to provide a more general description of the noise performance of sub-band modulation independent of signal type. The curves for the sub-band modulated (both the matched and mismatched carrier cases) and equivalent unmodulated signals followed roughly the same shape, only at different levels. The relative levels of the three curves in figure 5.8 corresponded to the peak matched filter levels observed earlier in this analysis. The average response of the sub-band signals demodulated with a matched carrier is about 1dB lower than the unmodulated response for  $SIR_i$  values above 0dB (or a drop in correlation of  $\sim 0.1$ ). Accordingly, the average response of the sub-band signals demodulated with a mismatched carrier (outside of the tolerance) is about 6dB lower than the response of the matched carrier case (or 7dB below the unmodulated response) for  $SIR_i$  values above 0dB. This corresponds to a drop in correlation of  $\sim 0.4$  below the matched carrier case and  $\sim 0.5$  below the unmodulated case. All three cases were relatively indifferent to interference above 0dB  $SIR_i$ , but the peak matched filter responses began to steadily decrease as the  $SIR_i$  decreased further. This closely follows the demodulation theory

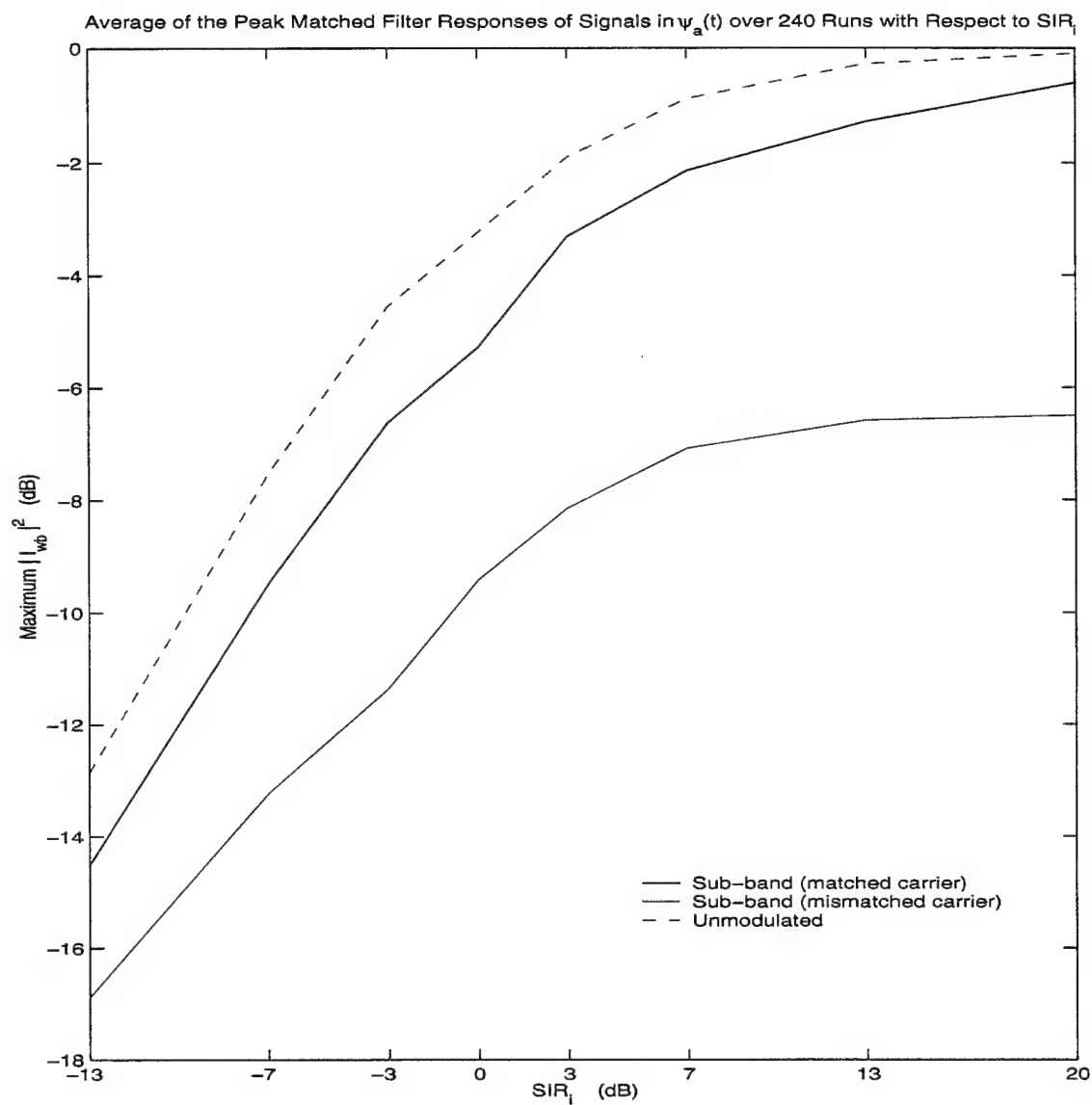


Fig. 5.8. Average of the Peak Matched Filter Responses of Signals in  $\psi_a(t)$  over 240 Simulations with Respect to  $SIR_i$  for Three Cases: Sub-band Signal Demodulated with a Matched Carrier (within the Tolerance), Sub-band Signal Demodulated with a Mismatched Carrier (Large Mismatch) and the Equivalent Unmodulated Signal

presented in section 3.3.2. Similar results were obtained when other simulation sets and scatterer velocities were used. Therefore, the results displayed in figure 5.8 are a reasonable representation of the overall noise performance of sub-band modulation.

## 5.2 In-Water Data Analysis

The matched filter responses of the in-water data were analyzed to verify the detection performance of sub-band modulation in a real world scenario. However, this was more difficult than anticipated. The reverberation levels for each interrogation were so high, that the scatterer returns were not discernible in most of the time-series. This resulted in very low  $SIR_i$  levels at the receiver. The strongest  $SIR_i$  level detected was approximately 0dB, and the average  $SIR_i$  values were below -5dB for the majority of the interrogations.

Each of the twenty-four scatterer returns were demodulated and matched filtered against the corresponding replica maps. The peaks in matched filter responses were at a relatively low level, since the  $SIR_i$  was so low for each of the interrogations. The peaks of the matched filter responses for the BPSK signals were noticeably lower than those of the CW signals, even though the matched filter peaks for the sub-band modulated CW and BPSK signals were roughly the same level observed in the simulations. Furthermore, the level of the BPSKs' responses were low enough, that significant peaks in the matched filter responses were only detected in nine interrogations out of twenty-four (and only four of those detections were prominent and easily discernible in the phase plane), whereas significant matched filter peaks were detected in sixteen interrogations for the CW signals. Seven of these CW detections were made without corresponding BPSK detections, while the other nine were from the same interrogations as the BPSK detections (otherwise known as joint detections). No BPSK detections were made without corresponding CW detections. This difference in detection performance with the BPSK signals is the result of it's phase sensitivity combined with the low  $SIR_i$  levels in these interrogations. Despite this difference, characteristics of the sub-band modulating signals' performance can still be analyzed from the few matched filter detections.

Sixteen detections were made in twenty-four interrogations with the sub-band modulated CW signal. The delay and Doppler values estimated from these matched filter responses corresponded with the scatterer parameters observed during the data collection for the majority of these interrogations. Nine of these interrogations were also joint detections with both the CW and BPSK signals, and the Doppler estimations

from both of the sub-band signals were equivalent. The delay estimations were also approximately equivalent, except that the BPSK's delay estimate was at a much higher resolution, which was expected (section 2.2). Figure 5.9 shows example matched filter responses for one of these interrogations, that resulted in a joint detection. Only eight interrogations out of twenty-four did not result in scatterer detections with either the sub-band modulated CW signals or both the sub-band modulated CW and the BPSK signals. The matched filter response for these interrogations were predominantly obscured by reverberation.

Despite the low number of joint detections, the in-water sub-band modulated signals performed reasonably similar to those in simulations with low  $SIR_i$ 's, that were also demodulated with mismatched carriers. This was especially reassuring, since the  $SIR_i$  was too low to effectively frequency match the received signals in the in-water case. Both the in-water data and the simulations verified, that multiple sonar signals sub-band modulating a carrier could be used to simultaneously estimate a scatterer's parameters. They also showed, that sub-band modulated signals could still be used to detect a scatterer even at low  $SIR_i$  values and without precisely matching the received carrier frequency. Although there were only a limited number of in-water interrogations available for analysis in this thesis, they yielded favorable results, even though they were at very low  $SIR_i$  values against a scatterer with very small l.o.s. velocities. Therefore, the further investigation of sub-band modulation through more extensive in-water testing against a variety of scatterers with different Dopplers over a large range of  $SIR_i$  values might be a worthwhile topic for future research.



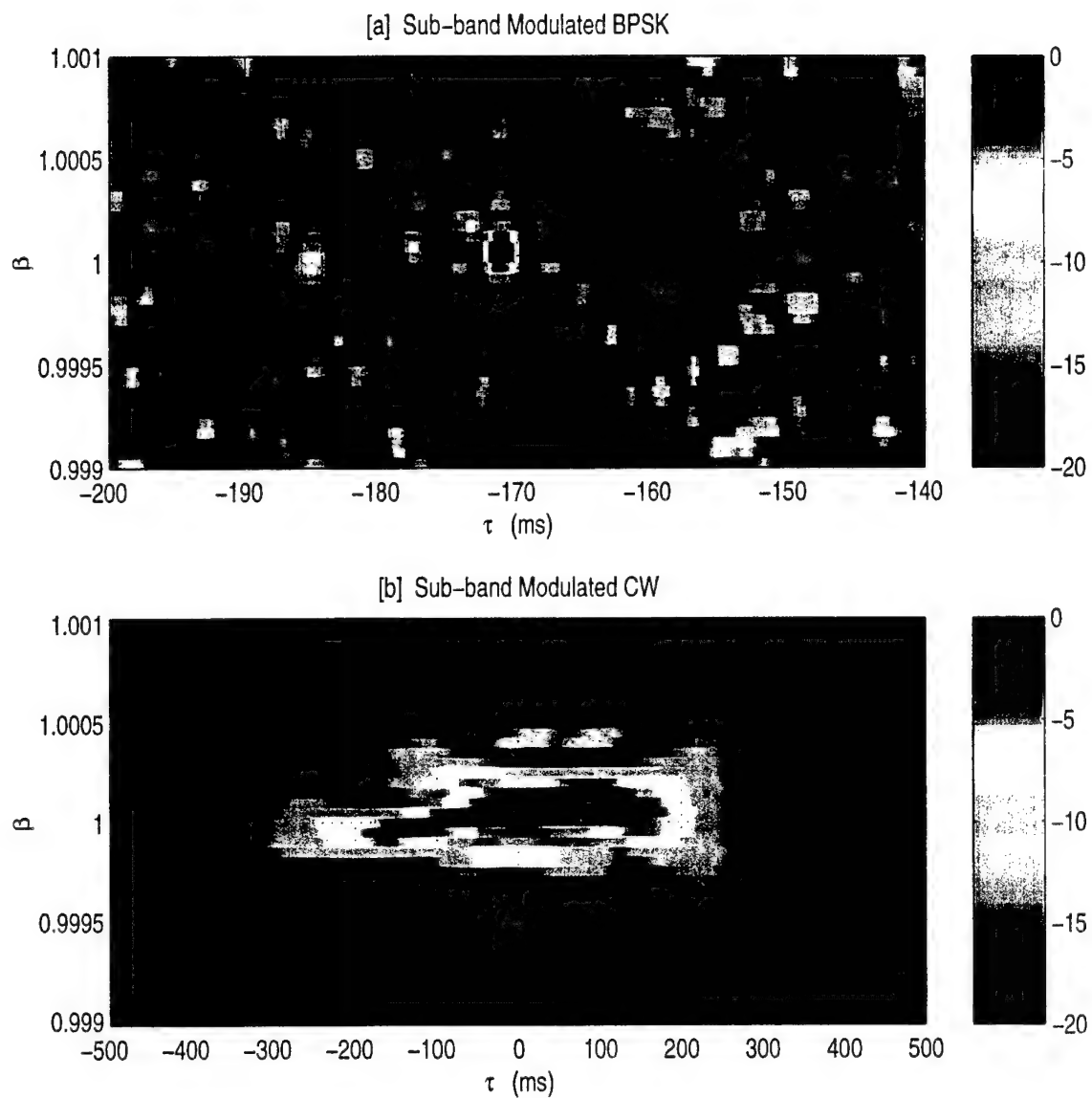


Fig. 5.9. Matched Filter Responses of Sub-band Modulated BPSK and CW Signal Combination ( $\psi_a(t)$ ) (In-Water): [a]  $s_{dh1}(t)$  Sub-band Modulated BPSK and [b]  $s_{dh2}(t)$  Sub-band Modulated CW

## Chapter 6

### Summary and Conclusions

This thesis presented a method of simultaneously transmitting multiple sonar signals, while maximizing transmission time and avoiding losses in total transmit energy caused by amplitude modulation in a peak power limited system. This process is known as sub-band modulation, and it is the linear combination of multiple sonar signals as the modulating phase component of a carrier signal. An analysis of the advantages and disadvantages of different sonar waveforms in different situations illustrated the benefits of transmitting multiple sonar signals. The specific benefits of different sonar signal combinations were also discussed. An extensive background of sonar theory and echo processing explained the advantages of simultaneously transmitting multiple sonar signals to characterize a given underwater event and the need to limit transmission time in active sonar. This background also gave insight into the methods used to estimate delay and Doppler parameters of a scatterer from echo signals backscattered off of it. Then, different types of modulation were investigated and compared to show the disadvantages of amplitude modulation in a peak power limited system and to further justify the use of sub-band modulation.

Next, the theory behind sub-band modulation was presented. The factors governing the modulation were discussed, and several examples were examined, that illustrated effects of these factors on transmit energy, modulation bandwidth and sideband locations of the modulating sub-bands. This was followed by an analysis of the demodulation process used to extract the individual sonar signals from the backscattered echo signals. Special attention was spent on the demodulation difficulties due to the scatterer parameter effects on the echo signal. Most of these difficulties stemmed from a frequency mismatch between the carrier of the received echo signal and the carrier implemented in the demodulation process. Methods of resolving these problems through frequency matching and coupling the demodulation process with hypothesis testing were then discussed and analyzed. These methods were found to successfully counteract the carrier mismatch. This discussion was followed by an analysis of the effects of interference on the demodulation of a sub-band modulating signal. In this section, it was found, that

the performance of the sub-band demodulation remains relatively unaffected by interference, when the signal-to-interference ratio is high. When the  $SIR_i$  drops low enough, the demodulator performance rapidly degrades.

The practicality of sub-band modulation was discussed in the experiment section of this thesis. First, waveform design considerations were discussed, and methods of selecting the modulation index and the frequency spacing of sub-band waveforms, while taking into consideration transducer bandwidth and potential scatterer Doppler, were presented. Second, the different sub-band signal combinations implemented in the experimental portion of this thesis were presented, and the motivation behind these signal combinations were discussed. An analysis of the modulation index used in this research followed this discussion. Third, the Matlab implementation of the sub-band modulation and demodulation processes were summarized, along with the echo processing. Finally, an overview of the different simulated and in-water experiments completed in this thesis and their goals were discussed. These experiments investigated the overall detection performance of sub-band modulating signals and were conducted to examine the effects of modulating signal type, signal-to-interference ratio and demodulation conditions on detection.

Finally, the results of the simulated and in-water experiments were discussed and analyzed. For the most part, the detection performance of the sub-band modulating signals was investigated in the simulations, while the in-water experiment was used to confirm this performance. The simulations indicated, that the signal type or combination does not adversely affect the detection performance of the sub-band modulating signals, while the number of sub-band modulating signals did influence detection. Scatterer range and velocity estimations made from the matched filter responses of the sub-band modulating signals matched the scatterer parameters in the simulations, and the shapes of the matched filter responses were not noticeably different from the responses of equivalent unmodulated sonar signals. However, the peak magnitudes of the matched filter responses of the sub-band modulating signals were slightly lower than the responses of the corresponding unmodulated signals, because of a small drop in correlation between the demodulated echo signal and the bank of replicas caused by the sub-band modulation process. It was also determined, that the detection performance of the sub-band signals were negatively affected by carrier mismatch. The demodulation process used in this thesis works best, when the demodulator can match the carrier frequency of the received signal. This performance was confirmed by the results from the simulations involving the coupled demodulation, hypothesis testing process. The performance of the sub-band

modulating signals demodulated with a matched carrier, the sub-band signals demodulated with a mismatched carrier and the equivalent unmodulated signals were evaluated and compared over a range of signal-to-interference ratios at the receiver. Although there was a difference between the matched filter peak magnitudes in the three cases, all of the cases showed similar decreases in performance as the signal-to-interference ratio decreased. A small set of in-water data with a sub-band modulated signal was also analyzed to verify the performance seen in the simulations. The results of this analysis were similar to the performance of the simulated data in similar circumstances, which consisted of small signal-to-interference ratios and mismatched carriers.

Possible future research topics in sub-band modulation could include a further investigation of different modulation indices and the resulting modulation bandwidths. Another possibility for future research would be to investigate different frequency tracking demodulators, such as the phase locked loop, and compare them with the ideal discriminator. Further evaluation of the coupled demodulation, hypothesis testing process is also warranted. Finally, more experiments (both simulated and in-water) should be conducted using more complex sceneries and a variety of different scatterers resulting in a wide range of Doppler values to more thoroughly examine the detection performance of sub-band modulating signals.

## References

- [1] Richard Alan Altes. *Methods of Wideband Signal Design for Radar and Sonar Systems*. PhD thesis, University of Rochester, Rochester, NY, 1970.
- [2] Harold S. Black. *Modulation Theory*. D. Van Nostrand Company, Inc., Princeton, New Jersey, 1953.
- [3] William S. Burdic. *Underwater Acoustic System Analysis*. Prentice-Hall, Inc., Englewood Cliffs, New Jersey, 1984.
- [4] T. Collins and P. Atkins. Doppler-sensitive active sonar pulse design for reverberation processing. *IEE Proceedings. Radar, Sonar and Navigation*, 145(6):347-353, December 1998.
- [5] Charles E. Cook and Marvin Bernfeld. *Radar Signals: An Introduction to Theory and Application*. Academic Press, New York, 1967.
- [6] A. J. Cutezo. Correspondence with A. J. Cutezo, 2000.
- [7] Yves Doisy, Laurent Deruaz, S. Peter Beerens, and Robert Been. Target Doppler estimation using wideband frequency modulated signals. *IEEE Transactions on Signal Processing*, 48(5):1213-1224, May 2000.
- [8] R. P. Goddard. The sonar simulation toolset. *Proc. Oceans '89, The Global Ocean (Volume 4)*, IEEE Publication Number 89CH2780-5, pages 1217-1222, 1989.
- [9] Stanford Goldman. *Frequency Analysis, Modulation and Noise*. McGraw-Hill Book Company, Inc., New York, 1948.
- [10] Michael J. Gustafson. Uncertainty product scattering function estimation. Master's thesis, Pennsylvania State University, University Park, PA, December 1993.
- [11] Carl W. Helstrom. *Elements of Signal Detection and Estimation*. Prentice-Hall, Inc., Englewood Cliffs, New Jersey, 1995.
- [12] Carl W. Helstrom. *Statistical Theory of Signal Detection*. Pergamon Press, London, 1998.

- [13] August Hund. *Frequency Modulation*. McGraw-Hill, Inc., New York, first edition, 1942.
- [14] Mathworks Inc. *Signal Processing Toolbox: User's Guide*. Mathworks Inc., Natick, MA, 1996.
- [15] William C. Knight, Roger G. Pridham, and Steven M. Kay. Digital signal processing for sonar. *Proceedings of the IEEE*, 59(11):1451–1507, November 1981.
- [16] F. Jessie MacWilliams and Niel J. A. Sloane. Pseudo-random sequences and arrays. *Proceedings of the IEEE*, 64(12):1715–1729, December 1976.
- [17] David Middleton. *An Introduction to Statistical Communication Theory*. The Institute of Electrical and Electronics Engineers, Inc., New York, third edition, 1996.
- [18] Richard O. Nielsen. *Sonar Signal Processing*. Artech House, Boston, 1991.
- [19] Philip F. Panter. *Modulation, Noise, and Spectral Analysis: Applied to Information Transmission*. McGraw-Hill, Inc., New York, 1965.
- [20] Athanasios Papoulis. *Probability, Random Variables, and Stochastic Processes*. McGraw-Hill, Boston, third edition, 1991.
- [21] D. W. Ricker. Constrained bandwidth waveforms with minimal dilation sensitivity. *IEEE Transactions on Aerospace and Electronic Systems*, 29(3):666–676, July 1993.
- [22] D. W. Ricker and A. J. Cutezo. Correspondence with D. W. Ricker and A. J. Cutezo, 1999.
- [23] D. W. Ricker and A. J. Cutezo. Estimation of coherent detection performance for spread scattering in reverberation-noise mixtures. *Journal of the Acoustical Society of America*, 107(4):1978–1986, April 2000.
- [24] D. W. Ricker and A. J. Cutezo. Detection of incoherent recombination with partial information. *IEEE Transactions on Aerospace and Electronic Systems*, 37(1):242–253, January 2001.
- [25] Dennis W. Ricker. The Doppler sensitivity of large TW phase modulated waveforms. *IEEE Transactions on Signal Processing*, 40(10):2406–2413, October 1992.

- [26] Dennis W. Ricker and Michael J. Gustafson. A low sidelobe technique for the direct measurement of scattering functions. *IEEE Journal of Oceanic Engineering*, 21(1):14-23, January 1996.
- [27] J. H. Roberts. *Angle Modulation: The Theory of System Assessment*. Peter Peregrinus LTD., London, 1977.
- [28] W. P. Robins. *Phase Noise in Signal Sources*. Peter Peregrinus LTD., London, second edition, 1984.
- [29] Mischa Schwartz. *Information, Transmission, Modulation and Noise*. McGraw-Hill, Inc., New York, third edition, 1980.
- [30] L. H. Sibul and D. W. Ricker. Correspondence between L. H. Sibul and D. W. Ricker, 1998.
- [31] Seymour Stein. Algorithms for ambiguity function processing. *IEEE Transactions on Acoustics, Speech, and Signal Processing*, ASSP-29(3):588-599, June 1981.
- [32] J. L. Stewart and W. C. Westerfield. A theory of active sonar design. *Proceedings from the IRE*, pages 872-881, May 1959.
- [33] Harry L. Van Trees. *Detection, Estimation, and Modulation Theory: Part 1 Detection, Estimation, and Linear Modulation Theory*. John Wiley and Sons, Inc., New York, 1968.
- [34] Harry L. Van Trees. *Detection, Estimation, and Modulation Theory: Part 2 Non-linear Modulation Theory*. John Wiley and Sons, Inc., New York, 1971.
- [35] Harry L. Van Trees. *Detection, Estimation, and Modulation Theory: Part 3 Radar-Sonar Signal Processing and Gaussian Signals in Noise*. John Wiley and Sons, Inc., New York, 1971.
- [36] Robert J. Urick. *Principles of Underwater Sound*. Peninsula Publishing, Los Altos, California, third edition, 1983.
- [37] Donald R. Wehner. *High-Resolution Radar*. Artech House, Boston, 1995.
- [38] Lora G. Weiss. *Wideband Inverse Scattering and Wideband Deconvolution of Acoustic Signals Using Wavelet Transforms*. PhD thesis, Pennsylvania State University, University Park, PA, May 1993.

- [39] Lora G. Weiss. Wavelets and wideband correlation processing. *IEEE Signal Processing Magazine*, 11(1):13–32, January 1994.
- [40] Anthony D. Whalen. *Detection of Signals in Noise*. Academic Press, San Diego, 1971.
- [41] R. E. Ziemer and W. H. Tranter. *Principles of Communications: Systems, Modulation, and Noise*. John Wiley and Sons, Inc., New York, fourth edition, 1995.